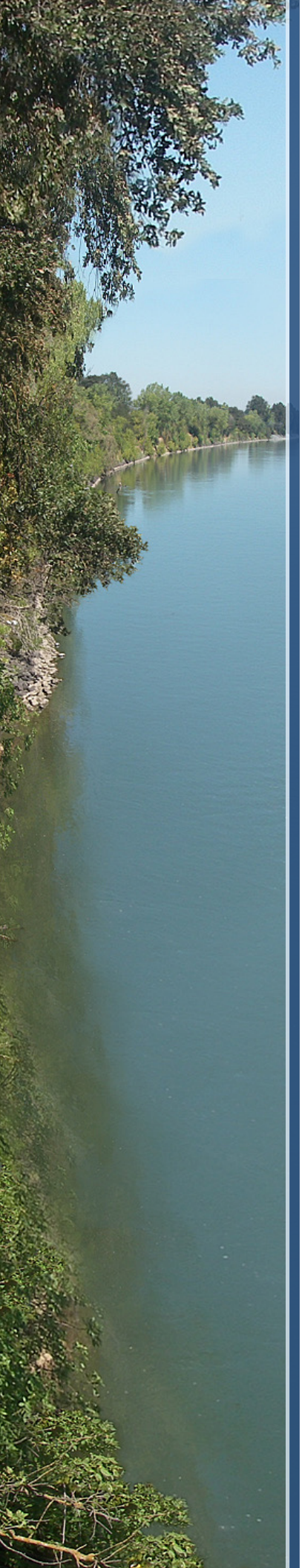

California Levee Vegetation Research Program

Influence of Tree Roots and Mammal Burrowing Activity on Levee Performance:
Volume 5. – Modeling Tree Roots and Mammal Burrowing Effects on Seepage and Stability of Levees

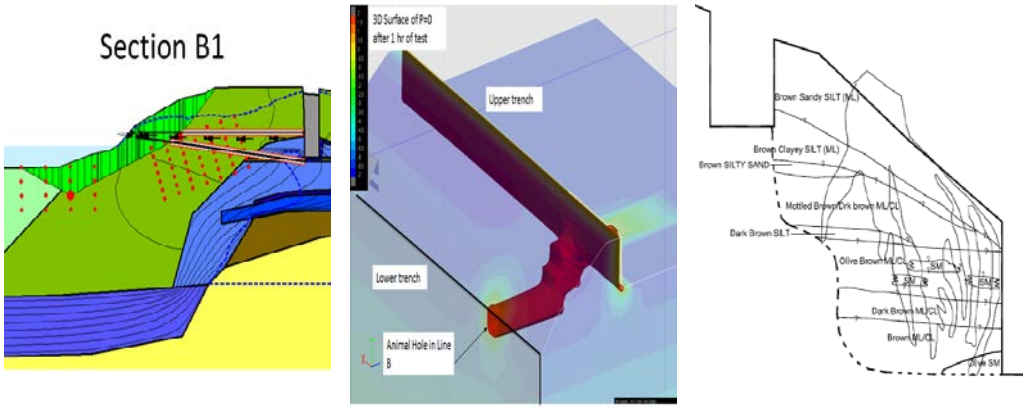

Diego Cobos Roa, Michelle Shriro, Nicholas Sitar and Jonathan D. Bray
Department of Civil and Environmental Engineering
University of California
Berkeley, CA 94720

Grant funding provided by:
The California Department of Water Resources (Contract No. 4600008761)
and the Sacramento Area Flood Control Agency (Contract No. 984)

October 2014

Geotechnical Engineering
UC Berkeley
Report UCB GT 13-03 vol. 5

Sponsoring/Advisory Agencies of the California Levee Vegetation Research Program

California Levee Vegetation Research Program

Influence of Tree Roots and Mammal Burrowing Activity on Levee Performance:
Volume 5. – Modeling Tree Roots and Mammal Burrowing Effects on Seepage and Stability of Levees

Diego Cobos Roa, Michelle Shriro, Nicholas Sitar and Jonathan D. Bray
Department of Civil and Environmental Engineering
University of California
Berkeley, CA 94720

Grant funding provided by:
The California Department of Water Resources (Contract No. 4600008761)
and the Sacramento Area Flood Control Agency (Contract No. 984)

October 2014

Geotechnical Engineering
UC Berkeley
Report UCB GT 13-03 vol. 5

CONTENTS

1 ABSTRACT 7

2 INTRODUCTION 8

2.1 SEEPAGE MODELING WITH SEEP/W 8

2.2 SLOPE STABILITY MODELING WITH SLOPE/W 8

3 PARALLEL TRENCH WETTING FRONT TEST: CAL EXPO 8

3.1 INTRODUCTION 8

3.2 SUMMARY OF TEST DATA 10

3.3 SEEPAGE MODELING 15

3.3.1 Soil Properties 15

3.3.2 3D Flow Model 19

3.3.3 Initial Conditions 20

3.3.4 Boundary Conditions 20

3.3.5 Results 21

3.4 SLOPE STABILITY ANALYSES 25

3.4.1 Approach 25

3.4.2 Results 27

4 CROWN TRENCH SEEPAGE TEST: TWITCHELL ISLAND 28

4.1 INTRODUCTION 28

4.2 INTERPRETED SECTIONS AND MESH DESIGN 30

4.3 SEEPAGE MODELING 34

4.3.1 Hydraulic Properties and Calibration 34

4.3.2 Seepage Modeling at Section A 43

4.3.3 Seepage Modeling at Section B 51

4.3.4 Seepage Analyses at Section C 59

4.4 SLOPE STABILITY MODELING 63

4.4.1 Modeling Root Reinforcement and Tree Loading *63*

4.4.2 Shear Strength Assumptions *66*

4.4.3 Pore Water Pressure Conditions *67*

4.4.4 Slope Stability Analyses Results *68*

4.5 DISCUSSION 74

4.5.1 Seepage Modeling *74*

4.5.2 Stability Analyses *75*

5 MODELING ANIMAL BURROWS AND OTHER DISCONTINUITIES 76

5.1 IDEALIZED SIMULATIONS 76

5.2 PIPING POTENTIAL OF COMPLETELY PENETRATING BURROWS 88

5.3 CLAYEY SITE LEVEE SIMULATION 90

6 CONCLUSIONS 92

7 REFERENCES 94

LIST OF FIGURES

Figure 3-1. Generalized cross section of wetting front test (Shriro et al., 2011). 9
Figure 3-2. Plan view of wetting front test (Cobos et al., 2012) [1 ft: 0.31 m]. 10
Figure 3-3. Instrument layout of wetting front test. T: tensiometer, P: piezometer, EX: hand augered boring [1 ft: 0.3 m]. 10
Figure 3-4. Dry run data for control trench. 11
Figure 3-5. Dry run data for stump trench. 12
Figure 3-6. Test data for control section (Line C). 13
Figure 3-7. Test data for section away from stump (Line B). 13
Figure 3-8. Test data for stump section (Line A). 13
Figure 3-9. Saturation times of Line B. 14
Figure 3-10. Saturation times for Line C. 14
Figure 3-11. Saturation times for Line A. 15
Figure 3-12. Gradation analyses for Cal Expo site. 18
Figure 3-13. Initial moisture contents. 19
Figure 3-14. Soil Water Characteristic curves. 19
Figure 3-15. Simplified analysis section. 20
Figure 3-16. Model results for instrument Line A (stump). Solid lines: instrument data, Dots: model data. 21
Figure 3-17. Model results for instrument Line B (gopher burrow). Solid lines: instrument data, Dots: model data. 22

Figure 3-18. Saturation front after 1 hour of test simulation. 23
Figure 3-19. Saturation front after 10 hours of test simulation. 23
Figure 3-20. Saturation front after 50 hours of test simulation. 24
Figure 3-21. Simulation results changing conductivity of roots. 24
Figure 3-22. Excerpt from the American River Watershed Project. Our study site is at Station 9+100 on the plan. Source: USACE, 1999. 26
Figure 3-23. Conceptual levee section representative of the test site. 26
Figure 3-24. A comparison of simulations with and without a stump yields factors of similar factors of safety for similar slide circles. 27
Figure 3-25. Total hydraulic head is held at 50 feet on the waterside. Three models are compared showing factor of safety with a low permeability stump and root system, no root system, or a fully decomposed root system acting as a series of voids. 28
Figure 4-1. Site and instrument layout plan. 29
Figure 4-2. Four waterside and two landside failure scenarios are delineated for analysis. 31
Figure 4-3. Section A interpreted section with model mesh. 32
Figure 4-4. Section B interpreted section with model mesh. 33
Figure 4-5. Section C interpreted section with model mesh. 34
Figure 4-6. Instrument line C showing instrument location and boundary conditions. 36
Figure 4-7. Instrument line C tensiometer data. 37
Figure 4-8. Instrument line C devices TC2-36 and TC4-24 38
Figure 4-9. Instrument line C devices TC4-60 and TC4-36 38
Figure 4-10. Instrument line B section and boundary conditions 39
Figure 4-11. Instrument line B devices TB2-36 and TB4-36 39
Figure 4-12. Instrument line B devices TB4-60 and TB5-36 40
Figure 4-13. Instrument line A section and boundary conditions 41
Figure 4-14. Instrument line A devices TA2-36 and TA4-24 41
Figure 4-15. Instrument line A devices TA4-36 and TA4-60 42
Figure 4-16. Instrument line A devices TA5-24 and TA5-36 42
Figure 4-17. Section A layers and boundary conditions. 43
Figure 4-19. Section A transient analysis scenarios. 44
Figure 4-20. Section A transient analysis results, open burrow on landside. Simulation time 0 hours. Total head contours, 2 ft interval and flux sections ($ft^3/s/ft$) included in plot 44
Figure 4-21. Section A transient analysis results, open burrow on landside. Simulation time 1 hour. Total head contours, 2 ft interval and flux sections ($ft^3/s/ft$) included in plot 45
Figure 4-22. Section A transient analysis results, open burrow on landside. Simulation time 10 hours. Total head contours, 2 ft interval and flux sections ($ft^3/s/ft$) included in plot 45
Figure 4-23. Section A transient analysis results, open burrow on landside. Simulation time 24 hours. Total head contours, 2 ft interval and flux sections ($ft^3/s/ft$) included in plot 45
Figure 4-24. Section A transient analysis results, open burrow on landside. Simulation time 48 hours. Total head contours, 2 ft interval and flux sections ($ft^3/s/ft$) included in plot 46
Figure 4-25. Section A transient analysis results, open burrow on landside. Simulation time 100 hours. Total head contours, 2 ft interval and flux sections ($ft^3/s/ft$) included in plot 46
Figure 4-26. Section A transient analysis results, open burrow on landside. Simulation time 200 hours. Total head contours, 2 ft interval and flux sections ($ft^3/s/ft$) included in plot 46

Figure 4-27. Section A transient analysis results, open burrow on landside. Simulation time 300 hours. Total head contours, 2 ft interval and flux sections ($ft^3/s/ft$) included in plot 47
Figure 4-28. Section A waterside inundation steady state models. 48
Figure 4-29. Section A landside inundation steady state models. 49
Figure 4-30. Section A centerline trench inundation steady state models. 50
Figure 4-31. Section B layers and boundary conditions. 51
Figure 4-33. Section B transient analysis scenarios. 52
Figure 4-34. Section B transient analysis results, comparison between open and plugged burrows. Simulation time 0 hours. Total head contours at 2 ft intervals shown..... 52
Figure 4-35. Section B transient analysis results, comparison between open and plugged burrows. Simulation time 1 hour. Total head contours at 2 ft intervals shown 53
Figure 4-36. Section B transient analysis results, comparison between open and plugged burrows. Simulation time 10 hours. Total head contours at 2 ft intervals shown..... 53
Figure 4-37. Section B transient analysis results, comparison between open and plugged burrows. Simulation time 24 hours. Total head contours at 2 ft intervals shown..... 54
Figure 4-38. Section B transient analysis results, comparison between open and plugged burrows. Simulation time 48 hours. Total head contours at 2 ft intervals shown..... 54
Figure 4-39. Section B transient analysis results, comparison between open and plugged burrows. Simulation time 100 hours. Total head contours at 2 ft intervals shown..... 55
Figure 4-40. Section B transient analysis results, comparison between open and plugged burrows. Simulation time 200 hours. Total head contours at 2 ft intervals shown..... 55
Figure 4-41. Section B transient analysis results, comparison between open and plugged burrows. Simulation time 300 hours. Total head contours at 2 ft intervals shown..... 56
Figure 4-42. Section B waterside inundation steady state models. 57
Figure 4-43. Section B landside inundation steady state models..... 58
Figure 4-44. Section B centerline trench inundation steady state models. 59
Figure 4-45. Section C layers and boundary conditions. 60
Figure 4-46. Section C transient analysis results. Simulation time 0 hours. Total head contours at 2 ft intervals shown..... 60
Figure 4-47. Section C transient analysis results. Simulation time 1 hour. Total head contours at 2 ft intervals shown..... 60
Figure 4-48. Section C transient analysis results. Simulation time 10 hours. Total head contours at 2 ft intervals shown 61
Figure 4-49. Section C transient analysis results. Simulation time 24 hours. Total head contours at 2 ft intervals shown 61
Figure 4-50. Section C transient analysis results. Simulation time 48 hours. Total head contours at 2 ft intervals shown 61
Figure 4-51. Section C transient analysis results. Simulation time 100 hours. Total head contours at 2 ft intervals shown 61
Figure 4-52. Section C transient analysis results. Simulation time 200 hours. Total head contours at 2 ft intervals shown 62
Figure 4-53. Section C transient analysis results. Simulation time 300 hours. Total head contours at 2 ft intervals shown 62
Figure 4-54. Section C waterside inundation steady state model..... 62

Figure 4-55. Section C landside inundation steady state model. 63
Figure 4-56. Section C centerline trench inundation steady state model. 63
Figure 4-57. Example of root reinforcing and distributed horizontal forces at the landside oak. 65
Figure 4-58. Example of root reinforcing and distributed horizontal forces at the waterside oak. 66
Figure 4-59. Landside failure scenarios modeled. Scenario A (orange) is in the vicinity of the landside oak tree while Scenario C (gray) is at the control section. 69
Figure 4-60. Failure scenario Waterside BC3 71
Figure 4-61. Failure scenario Landside A. 72
Figure 4-62. Waterside failure scenario B1. 73
Figure 4-63. Waterside failure scenario B2. 73
Figure 5-1. Idealized model section. 77
Figure 5-2. Results of idealized model. 78
Figure 5-3. Idealized model for flow into a single cavity. 78
Figure 5-4. Material properties for single-cavity idealized model. 79
Figure 5-5. Results of the single-cavity idealized model using sand. 80
Figure 5-6. Results of the single-cavity idealized model using fine-grained soil. 80
Figure 5-7. Multiple cavity idealized simulation. 81
Figure 5-8. Multiple cavity simulation results. 81
Figure 5-9. No cavity simulation results. 82
Figure 5-10. Simplified representation of animal burrow networks. 83
Figure 5-11. Steady state simulation of Sandy Levee Site burrows. Total head contour interval 0.25 m. 83
Figure 5-12. Input section for completely penetrating burrows. 84
Figure 5-13. Results from transient analysis after one day of simulation with burrow C. Contour interval: 0.25 m. 84
Figure 5-14. Evolution of pore pressures on a vertical section across the levee crown for burrow C 85
Figure 5-14. Results from transient analysis after one day of simulation. No holes present. Total head contour interval: 0.25 m. 85
Figure 5-16. Evolution of pore pressures on a vertical section across the levee crown for the case of no hole 86
Figure 5-17. Results from transient analysis after one day of simulation with burrow at A. Total head contour interval: 0.25 m. 86
Figure 5-18. Evolution of pore pressures on a vertical section across the levee crown at burrow A 87
Figure 5-19. Results from transient analysis after one day of simulation at Hole B. Total head contour interval: 0.25 m. 87
Figure 5-20. Evolution of pore pressures on a vertical section across the levee crown for the burrow at B 88
Figure 5-17. Piping potential evaluation using the Ohja (2003) formula. 89
Figure 5-18. Piping potential evaluation using the Sellmeijer (1988) formula. 89
Figure 5-19 High water on Clayey Levee Site in 1998. Images courtesy Al Romero, DWR 90
Figure 5-20. Clayey levee site 3D model 91

Figure 5-21. Critical flow velocities for different particle sizes compared to range of velocities along burrow 92

LIST OF TABLES

Table 3-1. Soil properties used for groundwater flow models. 18
Table 4-1. Soil properties used for flow models. 36
Table 4-2. Horizontal and vertical root forces for landside oak tree. 64
Table 4-3. Horizontal and vertical root forces waterside oak tree. 64
Table 4-4: Shear strengths used in modeling effort 67
Table 4-5. Results of mass averaged factor of safety for landside failure scenarios 70
Table 4-6: Results of mass averaged factor of safety against instability for waterside failure scenarios 74

1 ABSTRACT

Decomposing roots and ~~animal~~ burrows are capable of creating discontinuities within a levee embankment, which can lead to poor performance when subject to a hydraulic load, particularly piping and fast saturation of the levee prism. These can eventually lead to instability or deformation of the embankment. However, the mere presence of biotic activity, especially tree roots, is not necessarily sufficient to result in poor performance or failure, as described in Volume 1 of this report. An important condition for burrows or voids left by decomposing roots to present a threat to levee performance occurs when the voids are continuous and are directly connected to the source of hydraulic loading on the waterside. In such setting high potential head and associated high flow velocities can trigger piping or internal erosion.

The influence of woody vegetation on seepage through levees was evaluated by performing a series of transient seepage analyses using data obtained from the field seepage tests performed as a part of the California Levee Vegetation Research Program (CLVRP) on two different levee segments by Shriro et al. (2014 a, b) and Cobos et al (2014a, b). A separate series of analyses was carried out to assess the influence of burrows on seepage through levees using the data obtained from the field mapping of burrows also performed as a part of this effort, as described in Volume 4. The numerical simulations of the wetting front test at the Cal Expo levee were performed assigning a lower hydraulic conductivity value to a simplified root system geometry and were capable ~~to show~~ the effect of delayed saturation of the wetting front around the decomposed root system. Other simulations indicate that the position and continuity of a hole or gap within the levee dominate the potential for piping: a continuous hole located near the toe of the levee will have higher hydraulic heads and consequently higher piping potential compared to a continuous hole located in the upper meter of embankment. Similarly, discontinuous holes will not be a significant source of flow for piping or internal erosion because the flow into the cavity is controlled by the flow through the soil around it~~,~~ thus for an unsaturated levee the amount of water that will flow into a discontinuous cavity will be very small.

Based on calibrated numerical simulations at Cal Expo and Twitchell Island, trees were found not to play a significant role in seepage-induced rotational or block failure of the levee slopes. However, where trees exhibit significant lean (center of mass extends beyond the fulcrum of the root plate) or face strong wind loading, horizontal roots extending into the levee may place additional loads on the levee embankment. Loading was found to vary with degree of tree lean as well as slope angle. Horizontally oriented tree root loading increased faster than vertical loading in response to increasing slope angle, while vertical root forces increased more rapidly with increasing tree lean. Loading of this type can be incorporated into two~~-~~dimensional slope stability analyses, using mass-averaging to capture the three-dimensional impact of the tree. At the Twitchell Island test site, tree overturning was evaluated at the waterside oak tree. Root forces were represented as a single horizontal force and a single vertical force. The method was implemented and successfully captured the observed landside and waterside tree responses during the Crown Trench Seepage Test.

2 INTRODUCTION

2.1 SEEPAGE MODELING WITH SEEP/W

SEEP/W, the seepage module of the Geostudio software package, is a finite element software product for analyzing groundwater seepage and excess pore-water pressure dissipation in porous media. The two and three dimensional versions of this software were implemented to simulate field test seepage conditions and hypothetical flood scenarios. The software is capable of analyzing saturated and unsaturated steady-state and transient flow problems. Transient and steady state seepage conditions at the Cal Expo and Twitchell Island test sites were simulated to gain insight. The models were used to simulate pore pressure conditions for use in slope stability models.

2.2 SLOPE STABILITY MODELING WITH SLOPE/W

Slope stability modeling was performed using the General Limit Equilibrium Method (GLE). The method is based on two factor of safety equations balancing moments and forces over a range of potential slide masses. For each potential slide mass, the software divides the mass into a series of slices, taking a ratio of: 1) resisting moments divided by driving moments, and 2) resisting forces divided by driving forces. To solve this otherwise statically indeterminate system, an assumption is commonly made with regard to the angle of the normal force between slices. Side force assumptions are based on Morgenstern and Price (1965).

With the limit equilibrium method, the shear strength of site soils is estimated at the base and sides of each slice. For this study, the Mohr Coulomb method was implemented to arrive at a linear failure envelope defined by:

$$\tau = c + \sigma_n \tan\phi$$

Here τ is shear strength, σ_n is normal stress, ~~and~~ c is the intercept of the failure envelope axis of shear stress, and ϕ is the slope of the failure envelope. For drained conditions, effective stress parameters~~,~~ ϕ' and c' are specified for each material type.

3 PARALLEL TRENCH WETTING FRONT TEST: CAL EXPO

3.1 INTRODUCTION

This section summarizes the results of the field test performed on a levee near Sacramento, California, during September and October of 2010 (Shriro et. al, 2014a). The test section consisted of a silty levee, approximately 4.5 m high (16 ft) with landside and waterside slopes of 2:1 (horizontal to vertical). Groundwater level was located several meters below the area subject to the test; therefore, the test focused on the evolution of negative pore pressure values as a wetting front was generated by the test.

The principal objective of the field test was to study the influence of woody vegetation on the seepage patterns through the unsaturated portion of an embankment. Figure 3-1 is a simplified cross section showing the main elements of the test. Parallel trenches were excavated above (near the landside levee crown) and below (near landside levee toe) ~~of~~ a decomposing stump of a eucalyptus tree that was cut down around 1993. An additional set of trenches ~~was~~ excavated away from the stump to provide control conditions (Figure 3-2). The wetting front test consisted o~~n~~ filling the upper trenches with water, establishing a pressure head condition of 60 to 90 cm (2 to 2.5 ft) and monitoring the progression of the wetting front from the upper to the lower trenches through the use of the instrumentation arrays consisting of tensiometers and piezometers.

Three instrumentation lines (Lines A, B and C on Figure 3-2) were laid out with nests of tensiometers installed in depths ranging from 45 cm to 150 cm and vibrating wire piezometers from 150 to 210 cm, with the objective of covering the shallower soil layers where most of the root mass was located. Figure 3-3 shows a detailed instrumentation layout, with the location and name of each instrument installed at this site. The nomenclature used to name the instrument is as follows: the first letter indicates the type of instrument (T: tensiometer, P: piezometer), the following number indicates the row the instrument was located at (1 through 4 – ~~line~~ 1 was located near the upper trenches, and ~~line~~ 4 just above the lower trenches), the following letter indicates the instrument line (A through C), and the last number indicates the depth of the instrument in inches. Instrument Line A was located through the decomposing stump, Instrument Line B was located approximately 2.5 m left ~~(east~~) of Line A, and Instrument Line C was located through the control trenches.

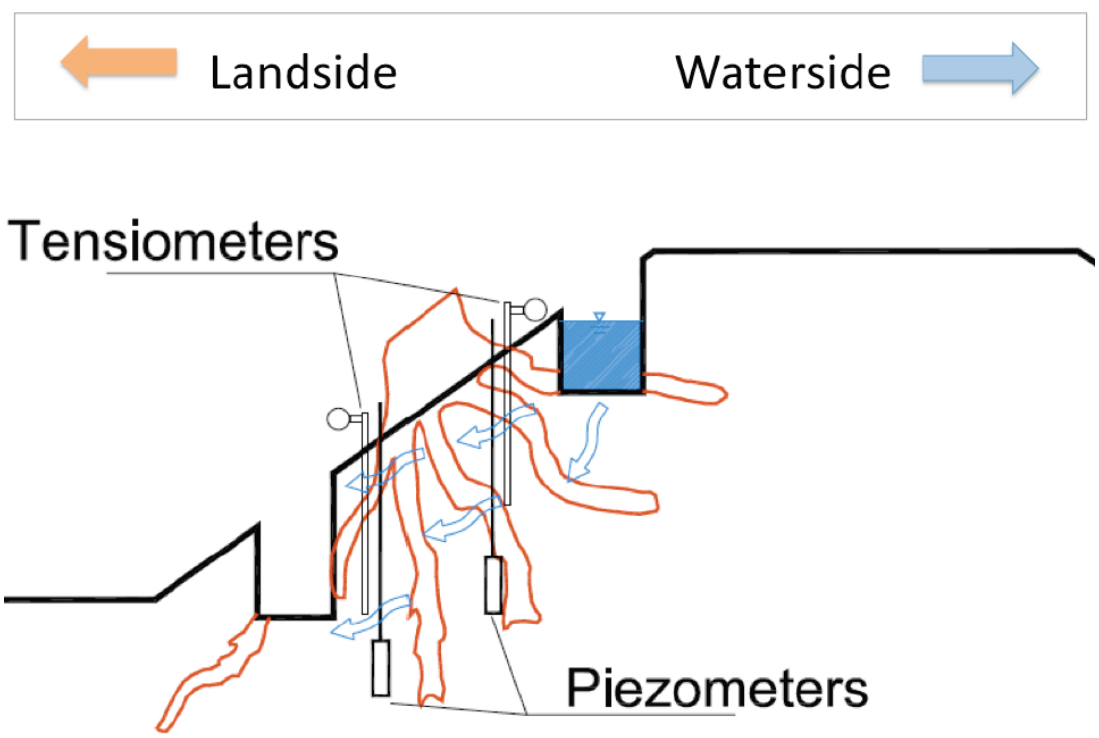

Figure 3-1. Generalized cross section of wetting front test (Shriro et al., 2011).

A pocket gopher burrow was encountered approximately 2.5 meters (8 ft) ~~east~~ (left) of instrument Line A~~, which~~ was later found to connect upper and lower stump trenches; surficial evidence of burrowing activity was also observed along the test area, as shown by the red circles on Figure 3-3. The existence of these holes proved to be a dominant factor on the wetting front test, as will be described in subsequent sections.

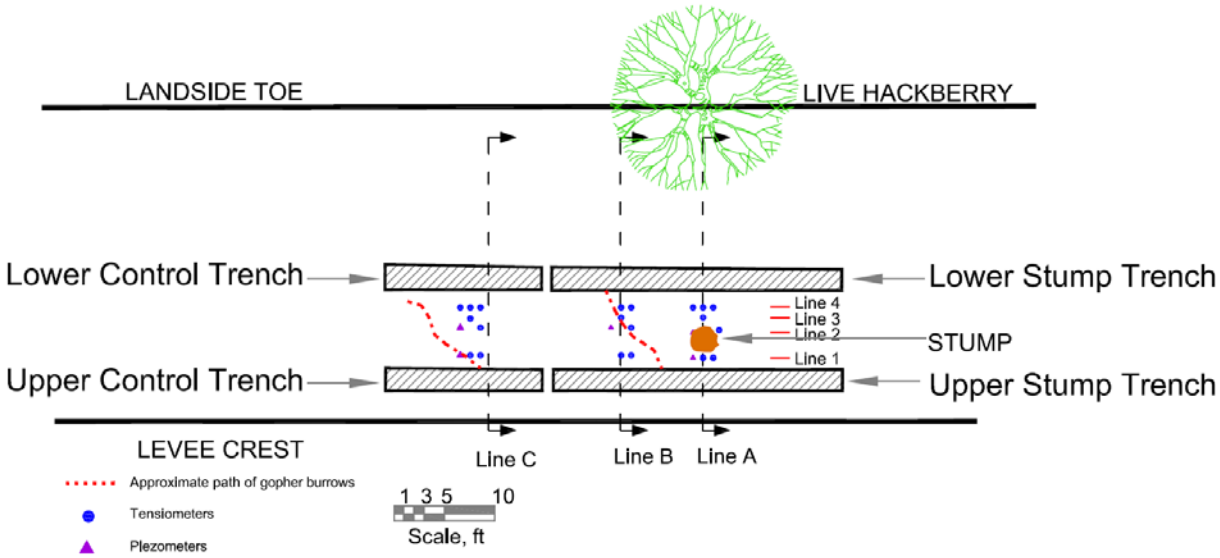

Figure 3-2. Plan view of wetting front test (Cobos et al., 2012) [1 ft: 0.31 m].

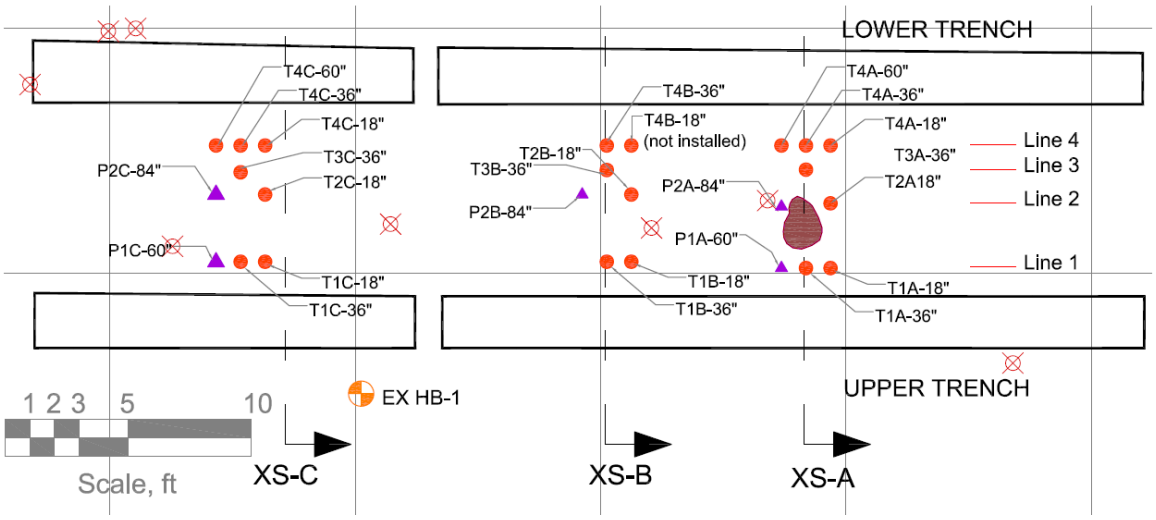

Figure 3-3. Instrument layout of wetting front test. T: tensiometer, P: piezometer, EX: hand augered boring [1 ft: 0.3 m].

3.2 SUMMARY OF TEST DATA

Suction values were recorded on each tensiometer using Campbell Scientific® CR3000 Microloggers, which allowed automatic data collection during the entire test using a

collection interval of 30 seconds. Piezometers were monitored using a Geokon® portable readout device therefore the amount of data collected for each piezometer was significantly less than the tensiometers.

Prior to commencing the wetting front test, a 'dry run' was performed to assure all devices, power sources and loggers were functioning correctly. Figure 3-4 and Figure 3-5 show the tensiometer data for the dry run test. Suction values ranged between 30 and 70 kPa during the 40 hours of dry run, and temperatures ranged from 60 to 100 degrees Fahrenheit. Sudden drops on recorded data represent times when the tensiometer tube was opened and refilled with water therefore losing the vacuum inside the tube and gauges. During this dry run refilling was performed several times given the high suction and temperatures that contributed to the quick emptying of the tensiometers.

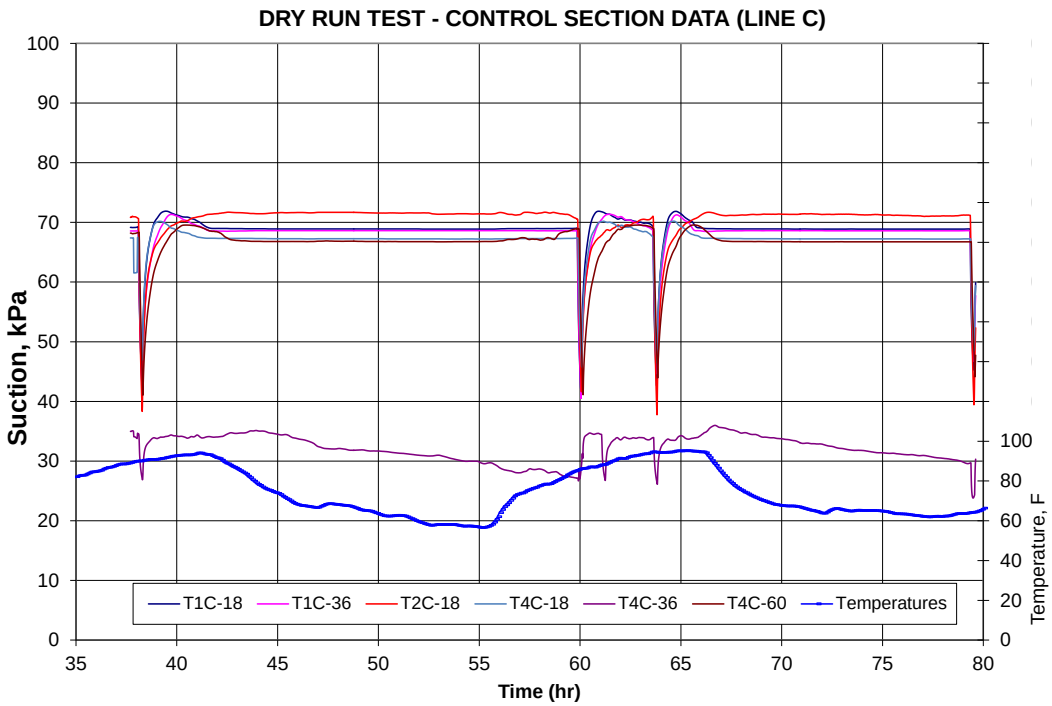

Figure 3-4. Dry run data for control trench.

The wetting front test started on September 7, 2010 at 10:57 am, some minutes after times were reset to zero and tensiometers were refilled and given enough time to re-equilibrate before turning on the 60 cm (2 ft) of pressure head on the upper trenches. Dataloggers were set to record every 30 seconds for the duration of the test, generating approximately ~~500 thousand~~ data points. Data reduction included smoothing each tensiometer series to remove high frequency noise.

Data recorded along each instrument line is shown on the following figures. Each time series contains a relatively flat segment near the start of the test, corresponding to the time prior to the arrival of the wetting front to the ceramic tip. The drop on tension values indicates that the wetting front reached the instrument and therefore suction values rapidly decrease to almost zero.

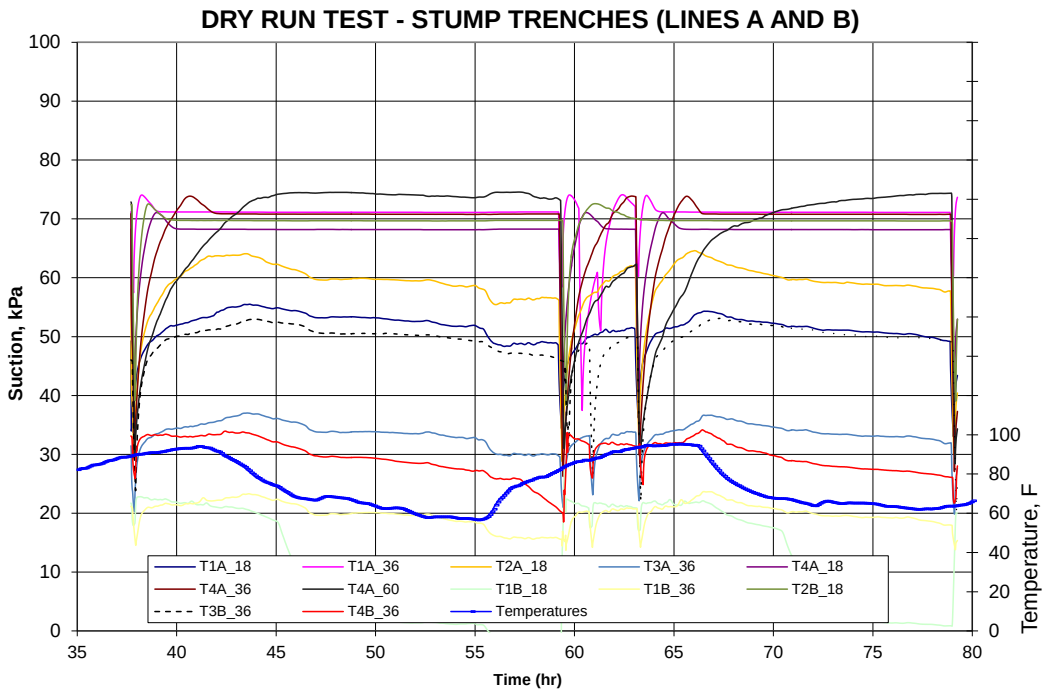

Figure 3-5. Dry run data for stump trench.

After saturation was achieved in all instruments, the upper trenches were allowed to empty and therefore the soil mass between the two trenches started to slowly drain. This is evidenced by the slight increase in suction after time = 120 hours. Figure 3-6 through Figure 3-8 show the entire suction time histories for Lines C, B and A, respectively.

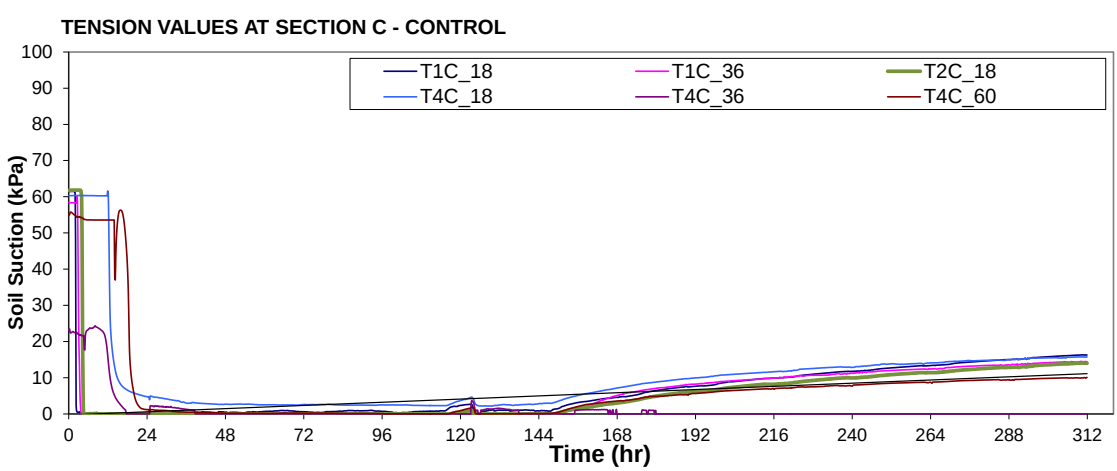

Figure 3-6. Test data for control section (Line C).

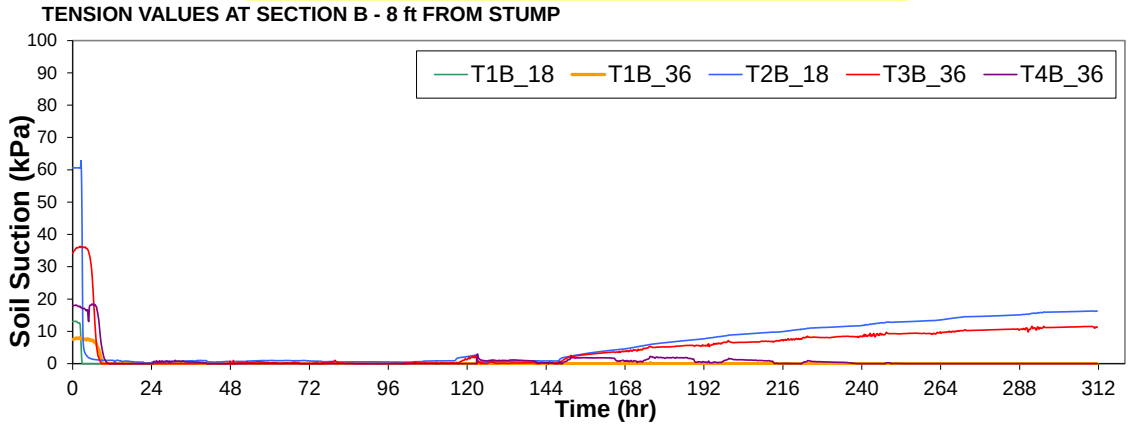

Figure 3-7. Test data for section away from stump (Line B).

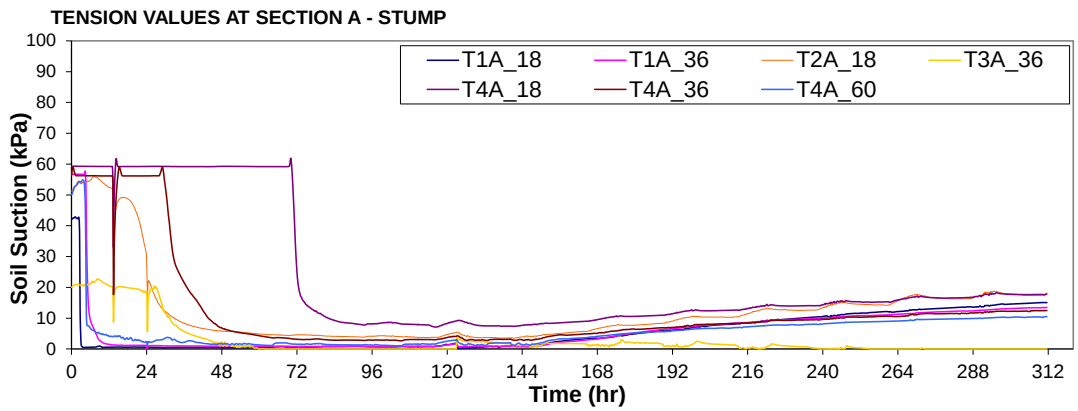

Figure 3-8. Test data for stump section (Line A).

INSTRUMENT LINE B SATURATION

The measured progression of the wetting front was ~~drastically~~ different between the three instrument lines; the following paragraphs describe the evolution of suction values for each section, starting with the fastest to saturate. Instruments on Line B (Figure 3-9) saturated in less than twelve hours, mainly because of the presence of a mammal burrow extending from the upper to the lower trench. This burrow was directly connected to the source of water and was able to transmit the full hydraulic head applied on the upper trench throughout the levee material, causing some surface seeps and small collapses on the lower trench wall within 30 minutes of the start of test. The saturation path on this instrument line extended from upper to lower trench and radially out from the continuous burrow. The first instrument to saturate was T1B-18, located 30 cm downslope from the upper trench wall, and 45 cm (18 inches) below slope surface. Suction values on this instrument went to zero approximately two and a half hours after the start of the test. The next instrument to saturate was T2B-18, located approximately 1.2 m (4 ft) downslope from the upper trench wall and 45 cm deep. This instrument saturated in three hours as flow from the pressurized burrow saturated this area.

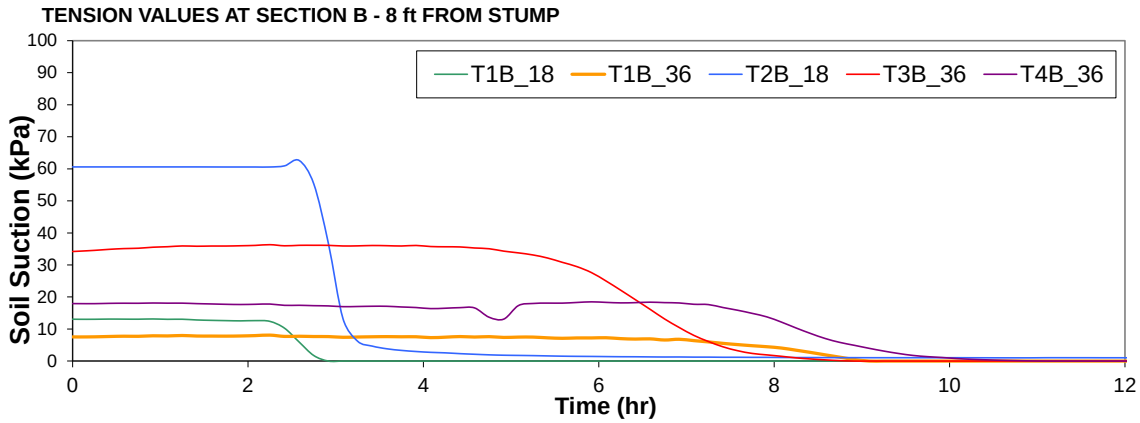

Figure 3-9. Saturation times of Line B.

The remaining three instruments saturated between six and ten hours from the start of the test driven by the fact that essentially the same head being applied on the upper trench was present inside the levee at all times during the test, allowing for a faster saturation of the mass of soil between the two trenches.

INSTRUMENT LINE C SATURATION

Instrument Line C (Figure 3-10), located through the control section showed a similar behavior to line B, as a small burrow was encountered extending from the upper trench approximately halfway between the upper and lower trenches. A small seep was encountered on the lower trench wall a few hours after the test started (Shriro et al, 2011), but did not expel as much water as the burrow on Line B. Saturation times for instruments on this line ranged between two and 22 hours, with the instruments in the vicinity of the small burrow saturating in less than four hours, and the remaining devices achieving saturation between 12 and 22 hours.

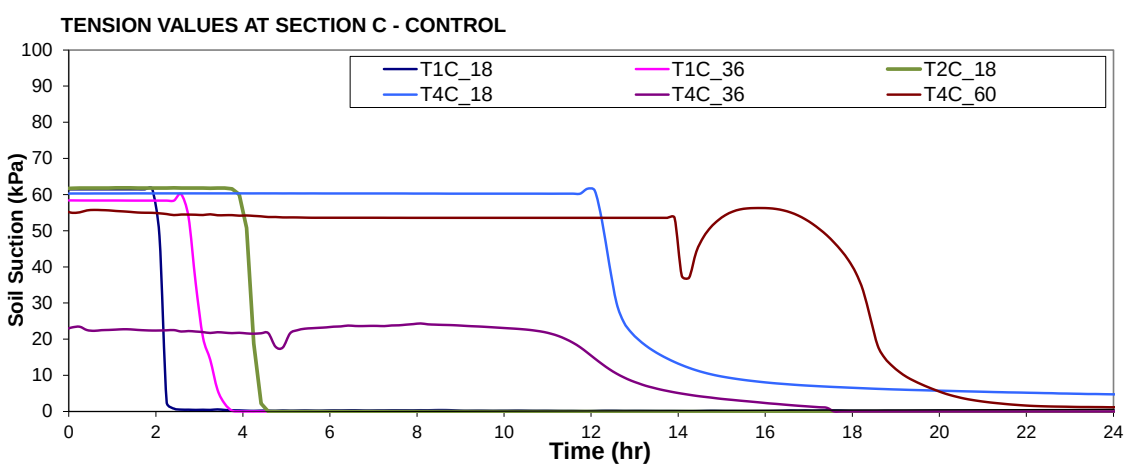

Figure 3-10. Saturation times for Line C.

INSTRUMENT LINE A SATURATION

Instruments along Line A (Figure 3-11) exhibited significantly ~~larger~~ times to reach saturation when compared to the other two instrument sections on the field test. Devices near~~by~~ the upper trench (T1A-18 and T1A-36, located 18 and 36 inches deep and approximately 30 cm from the upper trench wall) saturated between two and six hours from the start of the test, while most of the remaining instruments saturated between 30 and 70 hours later. Instrument T4A-60, located 60 inches deep and less than half a meter from the lower trench wall also exhibited a rapid saturation, approximately five and a half hours after the start of the test; this can be explained because of capillary saturation from the bottom of the lower trench, which was partially filled by the discharge flowing out of the mammal burrow near instrument Line B, located about 2.5 m east of the stump (on the same trench). The height of ~~the~~ water ponding ~~on~~ this trench was controlled using a pump, but a small column of water was present as the pump was unable to completely drain the trench. Consequently, instrument T4A-60, which was almost at the same depth as the bottom of the lower stump trench was saturated from the bottom of the experiment section via capillary rise.

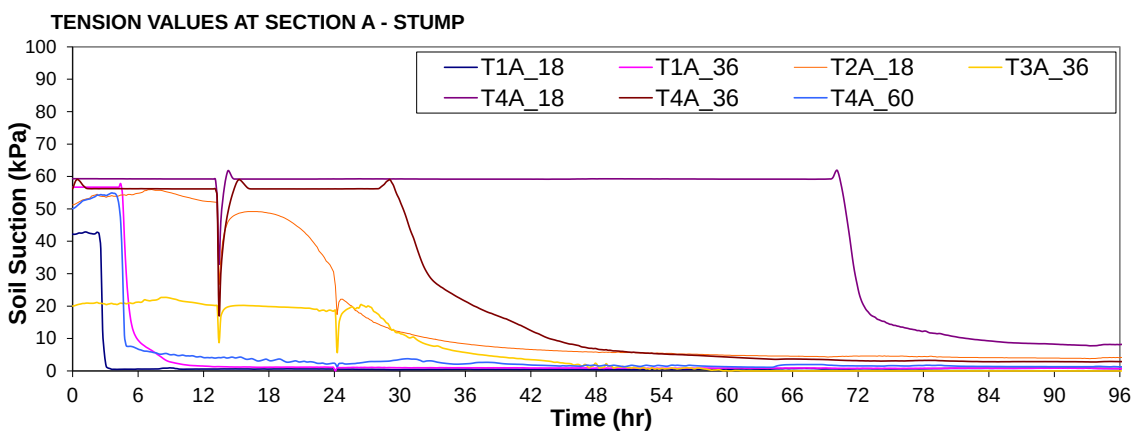

Figure 3-11. Saturation times for Line A.

The instruments around and downslope from the stump ~~consisted~~ of lines 2, 3 and 4 (T2A-18, T3A-36, T4A-18 and T4A-36) appeared to reach saturation more than one day later, suggesting that the progression of the wetting front was delayed by the presence of the decomposing stump. Even though some short and isolated gaps between the soil and the decomposed roots were encountered during excavation activities (see Volume 2), no tensiometer or piezometer recorded increased pore pressures near these features.

3.3 SEEPAGE MODELING

3.3.1 Soil Properties

Soil properties for the different layers were estimated using a combination of index tests (grain size, Atterberg limits, moisture contents) and suction testing (Tempe Cell tests) to determine the saturated and unsaturated properties of the profile on the test site.

Index tests were employed to determine soil texture and main type (Figure 3-12), and moisture contents were estimated before the test with the goal of having values of initial moisture contents correlatable with the unsaturated properties of the soil (Figure 3-13).

Suction tests using a Tempe cell ~~form~~ Soilmoisture Equipment Corp™ were performed to estimate the Soil Water Characteristic Curve (SWCC) of each layer (Figure 3-14), and in conjunction with typical correlations (Chapuis, 2004), saturated hydraulic conductivities were estimated for each layer. Unsaturated values of hydraulic conductivity and volumetric water content were estimated using the procedure described as follows:

Values of volumetric water content, or the volume of water contained in the pores of the soil were obtained at saturation conditions from laboratory tests. For the estimation of the decrease of these values under unsaturated conditions, the Van Genuchten (1980) relationship was used to estimate the soil water characteristic curves of each material (Equation 1).

Equation 1

$$\Theta = \Theta r + \frac{\Theta s - \Theta r}{\left[1 + \left(\frac{\Psi}{a}\right)^{n}\right]^{m}}$$

Where:

Θs, Θr = saturated and residual volumetric water contents, respectively

a, n, m = fitting parameters

n = 1/(1-m)

Ψ = suction [M/L^2]

Hydraulic conductivities were estimated for the different materials in the profile using available literature for the conductivity values in the positive pore pressure realm, and the Van Genuchten (1980) relationship (Equation 2) to estimate conductivity decrease under unsaturated conditions.

Equation 2

$$K = Ks\frac{[1 - (a\Psi^{n-1})(1 + (a\Psi^{n})^{-m})]^{2}}{[((1 + a\Psi)^{n})^{m/2}]}$$

Where:

Ks, K = saturated hydraulic conductivity and conductivity for a given value of suction [L/T]

a, n, m = fitting parameters

n = 1/(1-m)

Ψ = suction [M/L^2]

With the saturated hydraulic conductivities known, the Van Genuchten (1980) (Equation 3 and Equation 4) uses the volumetric water content (or soil water characteristic curve) function to estimate the parameters a, n and m, as follows:

Equation 3

$$Sp = \frac{1}{(\Theta s - \Theta r)} \left| \frac{d\Theta p}{d(log\Psi p)} \right|$$

Where:

Θs, Θr = saturated and residual volumetric water contents, respectively

Θp = volumetric water content at the halfway point of the volumetric water content function

Ψp = matric suction at Θp [M/L^2]

Equation 4

$$m = 1 - \exp(-0.8\, Sp)\ [for\ 0 < Sp < 1]$$

$$m = 1 - \frac{0.5755}{Sp} + \frac{0.1}{Sp^2} + \frac{0.025}{Sp^3}\ [for\ Sp > 1]$$

$$a = \frac{1}{\Psi}\left(2^{\frac{1}{m}} - 1\right)^{(1-m)}$$

Layer compressibility is a corollary of layer storativity and transmissivity properties. Internally, the code employed for the modeling calculates transmissivity as the product of hydraulic conductivity and layer thickness. Another parameter used in the transient calculations is the coefficient of compressibility of the aquifer layer (Mv), which can be estimated from consolidation tests for fine grained soils, or correlated from storage coefficients estimated in pump tests. This value was left unchanged from the program default of 1x10^{-5} 1/kPa for all layers in the profile.

Table 3-1 summarizes the properties determined by the different tests and correlations. Gradation analyses performed in fifteen samples from the Cal Expo site are presented in Figure 3-12. Fines content in the soil ranged from 60 to 90% for thirteen of the samples, while two samples exhibited a percentage of fines between 35 and 43. The former represent sandy silt (ML) materials while the latter were classified as silty sand (SM) samples. Suction tests performed to eleven of these samples show a similar pattern, with most of the samples clustered in a saturated volumetric water content between 40 and 50% and a water content ranging between 25 and 35% after applying a suction of 100 kPa, indicating the type of behavior expected from a sandy silt sample. The remaining samples exhibited a more sandy-like characteristic curve, with saturated content between 20 and 25% and 10% when 100 kPa of suction were applied to the sample. The dotted lines

accompanying the two clusters of test results were created using the Van Genuchten (1980) relationship, employing the following parameters:

Table 3-1. Soil properties used for groundwater flow models.

Material	Ksat (cm/s)	θ[1] sat	θ res	a (kPa)	n[2]	m[2]	Ky/Kz
Silt	$1x10^{-5}$	0.45	0.06	6.0	1.25	0.2	0.25
Sand	$1x10^{-5}$	0.20	0.08	0.3	3.0	0.67	0.25

[1]Volumetric water content, [2]coefficients used in the Van Genuchten (1980) equation for characteristic curves.

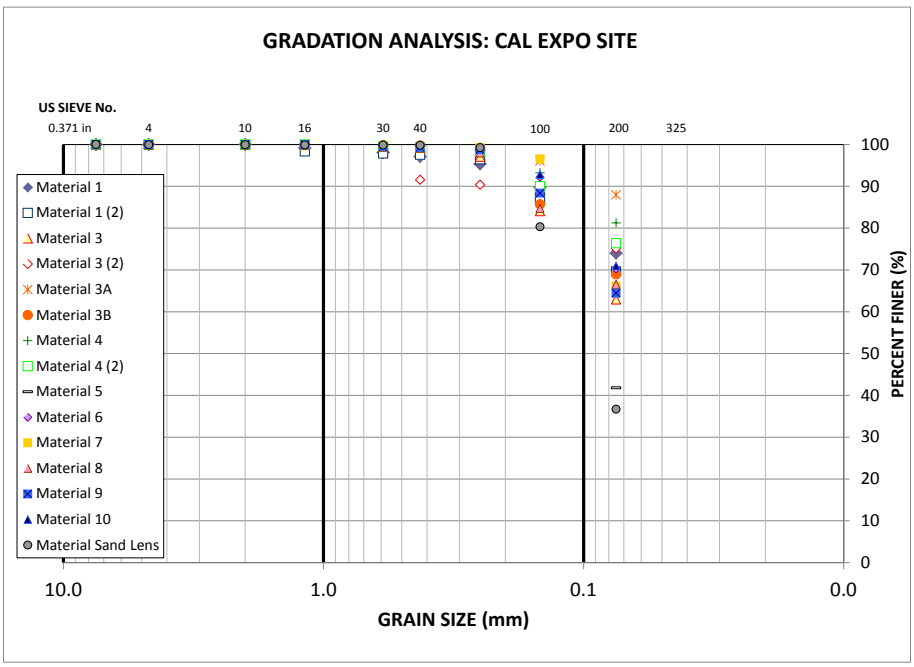

Figure 3-12. Gradation analyses for Cal Expo site.

The volumetric moisture content values shown on Figure 3-13 were used as a guide for truncating the SWCCs used in the finite element flow models described in subsequent sections. These, in conjunction with the recorded suction values during the dry run test were instrumental in defining initial conditions for the different soil layers and avoiding the calculation of very low values of hydraulic conductivity during model solution.

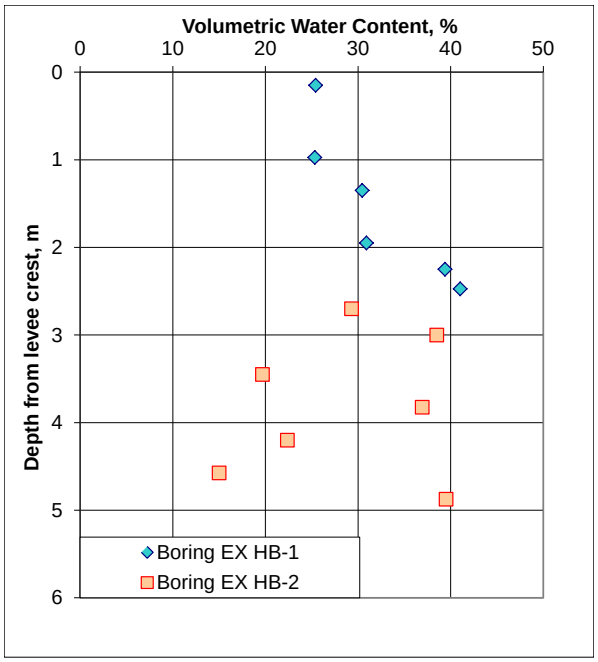

Figure 3-13. Initial moisture contents.

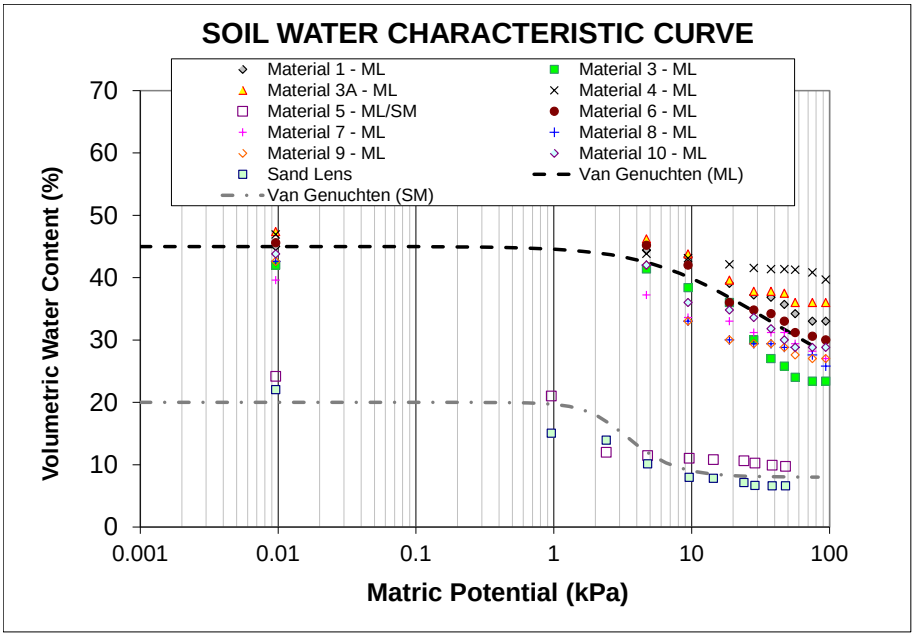

Figure 3-14. Soil Water Characteristic curves.

3.3.2 3D Flow Model

Seep3D, the three dimensional seepage package from GEOSTUDIO®, was used to develop a 3D finite element model that incorporated the root system and soil layers. The complexity of the problem and software limitations did not allow modeling the 3D geometry in its full detail, nor the presence of the finite and discontinuous spaces encountered between some roots and the surrounding soil. Consequently, the decomposing root system was modeled

as a homogeneous region with a value of hydraulic conductivity lower than the surrounding soil for the purposes of back-calculating the results of this field test. The simplified section is shown on Figure 3-15.

The domain was divided in cubic regions of 0.2 m side length in the vicinity of the root system, and roots were simulated by assigning a lower hydraulic conductivity to the regions along the roots. Finite element size was 0.1 m in and around the decomposing root system. Away from the root system, cluster size increased to 0.5 m with finite element size of 0.25 m. The Gopher burrow encountered along instrument Line B was modeled as an open space with a potential seepage (drainage) face boundary condition within the mesh.

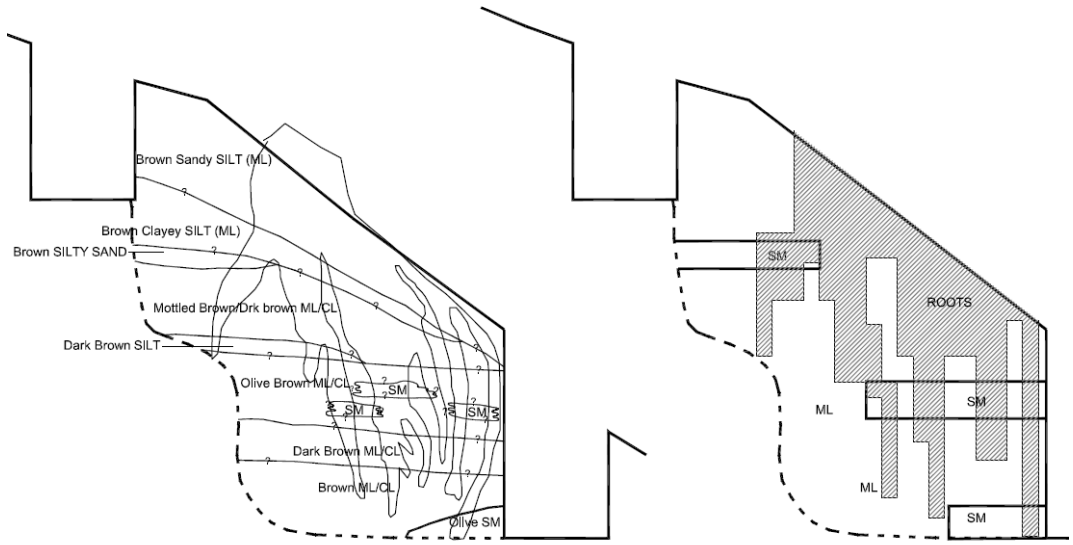

Figure 3-15. Simplified analysis section.

3.3.3 Initial Conditions

Initial conditions were defined using the values of initial moisture content and suction values measured during the dry run performed prior to the wetting front test. An initial finite element model was run by changing the position of the initial water table until suction values similar those measured by the tensiometers were computed by the software. Additionally, soil water characteristic curves were truncated at the maximum value of measured suction to avoid computation of very high tension values by the software that could translate into uncharacteristically low values of volumetric water content and therefore very low values of unsaturated hydraulic conductivity.

3.3.4 Boundary Conditions

Boundary conditions for the transient model were set to a constant pressure head for the duration of the wetting front test equal to 60 cm (2 ft) along the upper trenches and along the mammal burrow on instrument Line B; assuming that the burrow was not plugged and,

therefore, no head loss occurred along its length. A seepage face (review nodes) boundary condition was assigned to the lower trench walls and levee slope to allow for flux seeping out of the surface without ponding on the surface. Finally, since visqueen sheets were placed along the bottom and back walls of the upper trenches to minimize flow towards the waterside (opposite) slope of the levee, a no-flow boundary condition was applied along these edges.

3.3.5 Results

Model results are compared with tensiometer data ~~in~~ for instrument Line A (stump, Figure 3-16) and for instrument Line B (gopher burrow, Figure 3-17). Continuous lines represent instrument data and dots represent model results. The resulting suction values from the 3D model compare relatively well with the measured values during the field test, especially for the instrument line along the animal burrow, given the short time that took to achieve saturation. Along the instrument line across the stump the model values do not achieve a good match; however, the general trend of slower progression of the wetting front was captured by including a simplified representation of the root system using lower hydraulic conductivity clusters in the mesh.

The progression of the wetting front is represented by plotting a surface of zero pressure head (P=0) at different times during the simulation of the field test. Figure 3-18, Figure 3-19 and Figure 3-20 show these surfaces at time of 1, 10 and 50 hours from the start of test, with the saturation front shown as a red surface on the stump trench. The effect of the gopher burrow (lower right corner of figures) is evident after just one hour of test simulation. The saturation front is not only extending from the upper trench towards the lower trench, but radially out from the burrow, which is acting like an open pipe with the same pressure head applied on the nodes along the upper trench.

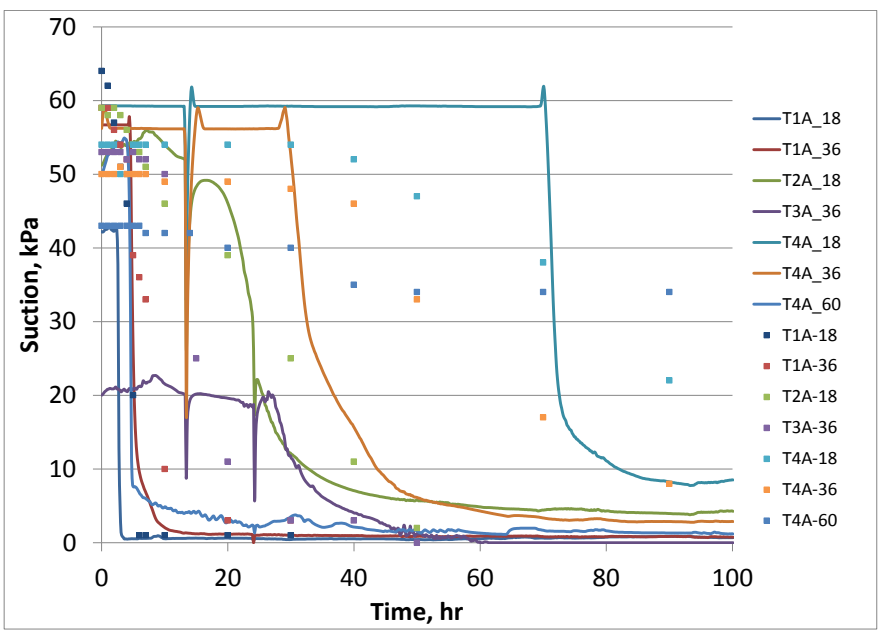

Figure 3-16. Model results for instrument Line A (stump). Solid lines: instrument data, Dots: model data.

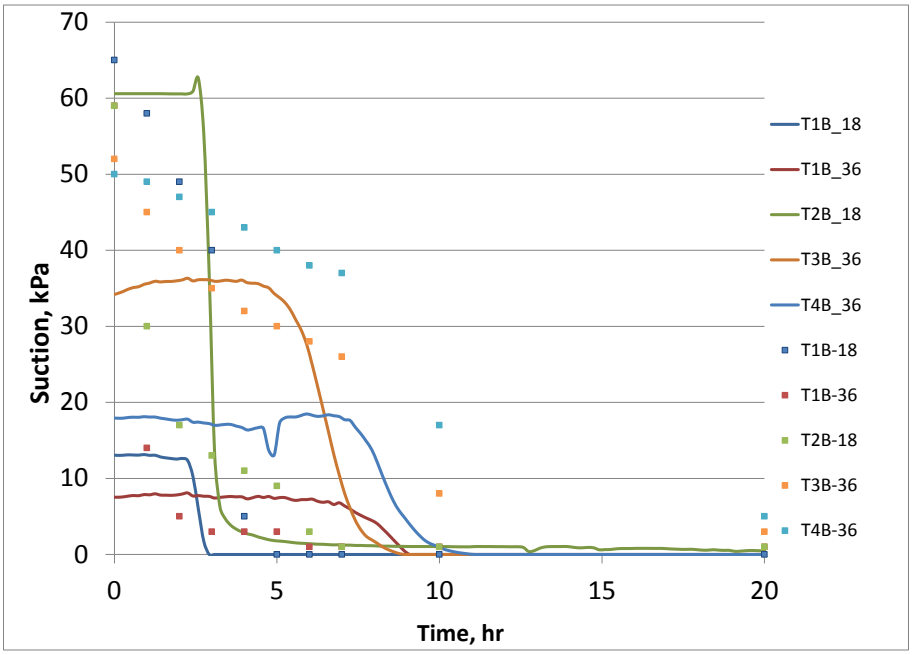

Figure 3-17. Model results for instrument Line B (gopher burrow). Solid lines: instrument data, Dots: model data.

The simulations show that after one hour of test (Figure 3-18) the saturation front has advanced only a few inches from the upper trench, consistent with values from tensiometers T1A-18, T1A-36 and T2A-18, which showed constant tension values for the first three hours of test. Figure 3-19 shows the simulated position of the wetting front after five hours, where the front has advanced approximately 50 centimeters downslope in the vicinity of the burrow and only a few centimeters along the rest of the trench. This is consistent with observed suction values along Line A (stump), which remained relatively constant between 20 and 60 kPa, depending on the instrument. The instruments along Line B (burrow) have started to saturate, particularly the instruments near the upper trench and the line situated 30 cm downslope.

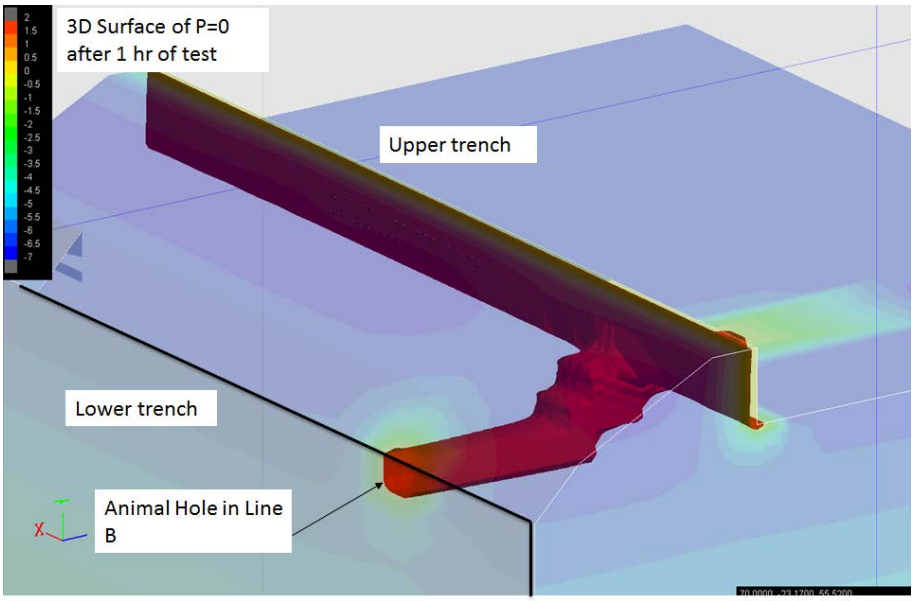

Figure 3-18. Saturation front after 1 hour of test simulation.

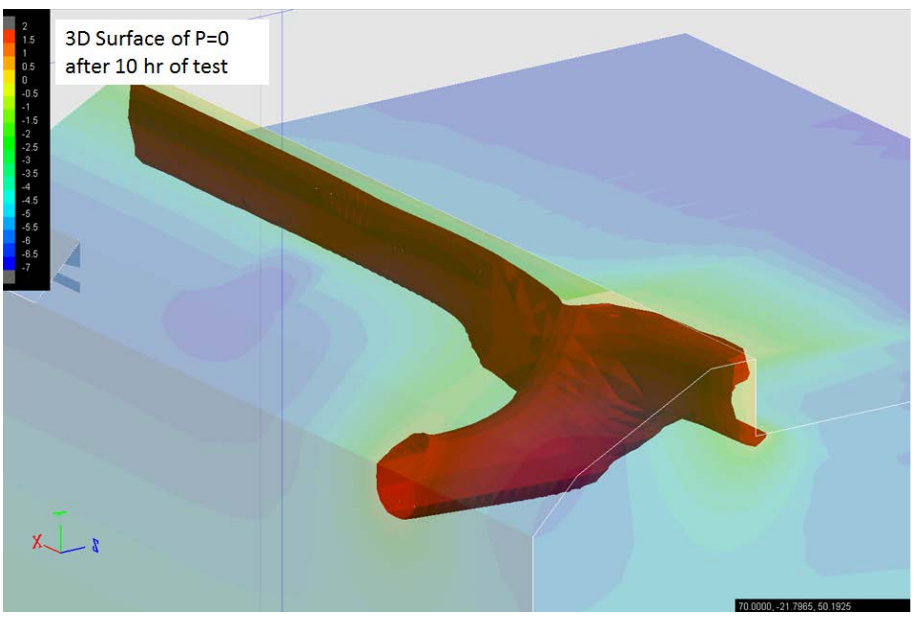

Figure 3-19. Saturation front after 10 hours of test simulation.

The position of the wetting front after 50 hours of test simulation is shown on Figure 3-20. By this time the upper wall on the lower trench is saturated in the vicinity of the gopher burrow, and the wetting front is being delayed by the presence of the lower hydraulic conductivity clusters composing the tree root system. This is shown by the pronounced curvature on the P=0 surface on Figure 3-20 indicated by the arrow.

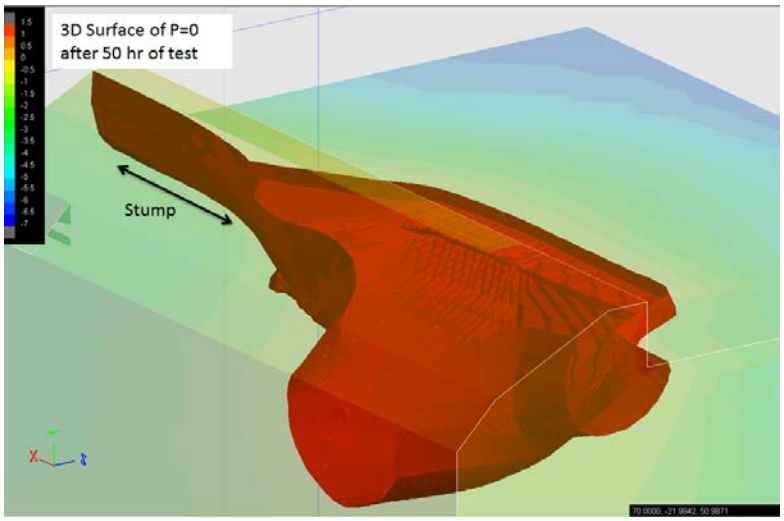

Figure 3-20. Saturation front after 50 hours of test simulation.

Additional simulations were performed by changing the properties of the clusters assigned to the decomposing root system and the soil mass around it. The first of such models assigned a high value of hydraulic conductivity to said regions (1x10-3 cm/s). The results (Figure 6-31) indicate that despite the roots being composed of a higher conductivity material, the influence on the saturation of the soil mass is negligible compared to that of a completely penetrating burrow. The fact that the high conductivity clusters are arranged in an irregular manner and are not directly connected to the hydraulic head being applied to the levee does not allow the establishment of a relatively fast flow along these elements because the flux of water into these holes is dependent on the flux of water out of the unsaturated fine-grained soil around the discontinuity. The P=0 surface shown on Figure 6-31 is very similar to the previously shown plots, with the difference that the marked curvature near the stump area is no longer present.

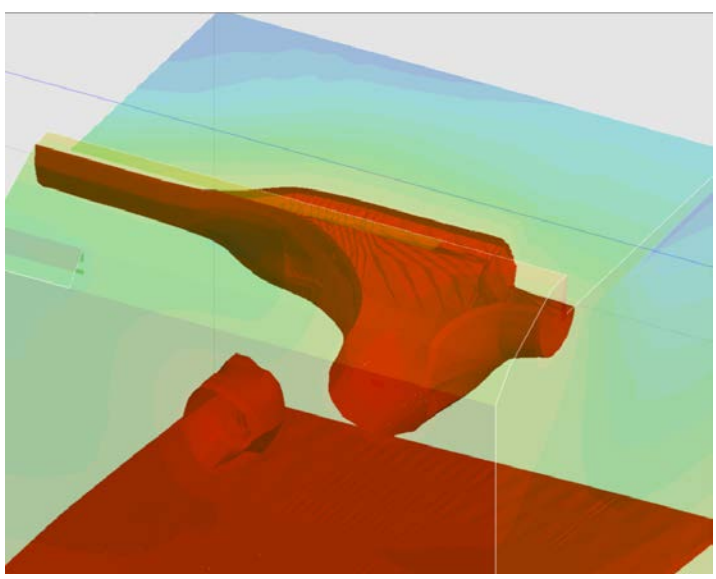
Figure 3-21. Simulation results changing conductivity of roots.

3.4 SLOPE STABILITY ANALYSES

3.4.1 Approach

Two and three dimensional transient and steady state seepage modeling of the localized zone of study during the Parallel Trench Wetting Front Test at Cal Expo are described above and in Cobos-Roa (2014). Available soil boings, cone penetration tests and nearby interpreted sections were reviewed in Volume 2 of this series (Shriro et al., 2014a). Nearby interpreted sections were prepared by URS (2009). These sections were modified slightly based on available soil information near the site and used for models (Figure 3-22). The slurry wall that exists at the site was omitted from the seepage and slope stability analysis to view the impact of the decomposing root system for a levee without a slurry wall.

The site was evaluated under steady state seepage conditions under simulated flood conditions. Steady state seepage conditions with water surface elevations of 40 feet and 50 feet were simulated for input into stability models. The model geometry is presented as Figure 3-23. The root system was modeled either as a zone with lower hydraulic conductivity than surrounding soils or as a zone with voids. The models were performed in two dimensions, though the problem is three dimensional. Where three-dimensional effects are important, mass averaging of slide sections across the potential slide area, as presented in subsequent sections, or the use of three-dimensional models could be implemented to improve the analysis.

Drained friction angles for similar soil deposits at nearby locations modeled by URS (2009) were adopted to model stability at the site. Selected parameters ~~and~~ are summarized on Figure 3-23. Design parameters forced a failure plane to avoid intersecting the stump through use of a high friction angle. The loose nature of decomposing roots, partially in-filled with loose soils, was estimated based on an assumption that the decomposed roots may be about two-thirds filled with loose frictional soils and organic matter. A typical effective stress friction angle for a very loose sand is $\phi' < 30°$. An effective stress friction angle of 20 degrees was selected to represent the very loose infill soil and void space.

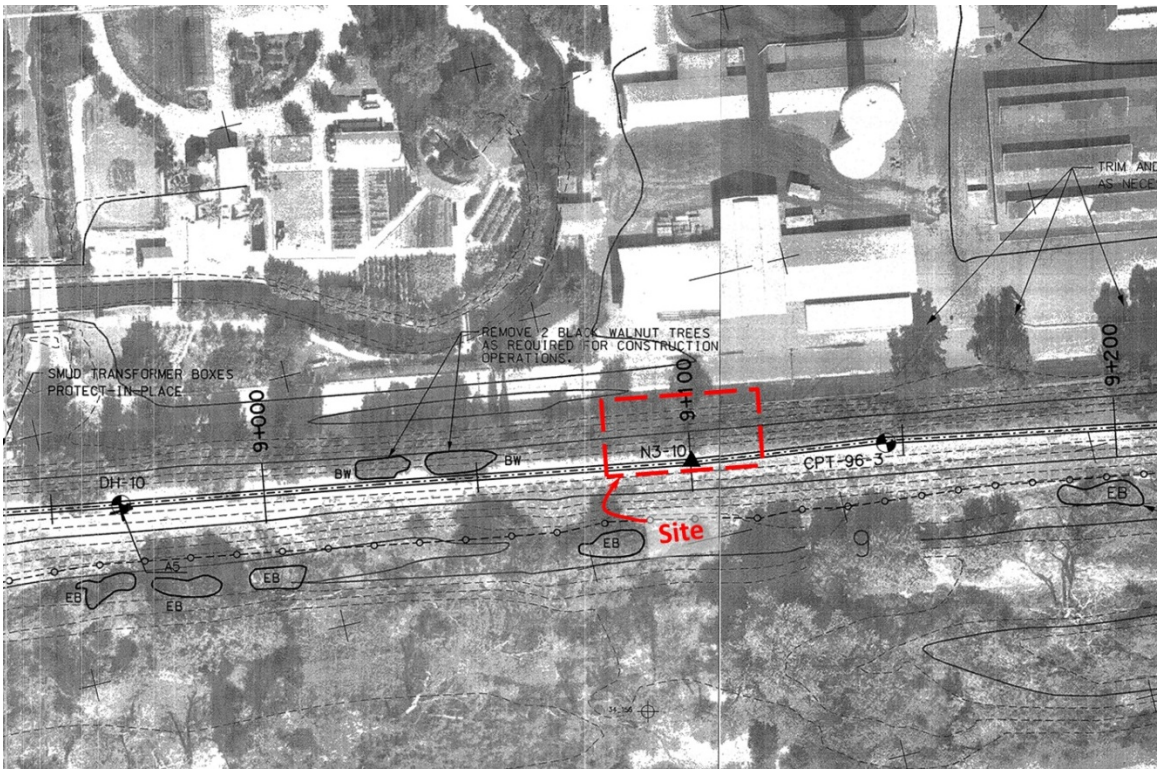

Figure 3-22. Excerpt from the American River Watershed Project. ~~Our~~ study site is at Station 9+100 on the plan. Source: USACE, 1999.

	Unit Weight (pcf)	Drained Parameters c'	Drained Parameters ϕ'
Silt (ML)	120	0	33
Silty Gravel (GM)	135	0	45
Silty Lean Clay (CL)	110	0	33
Silty Sand (SM)	130	0	40
Stump	60	0	60
Decayed Roots	85	0	20

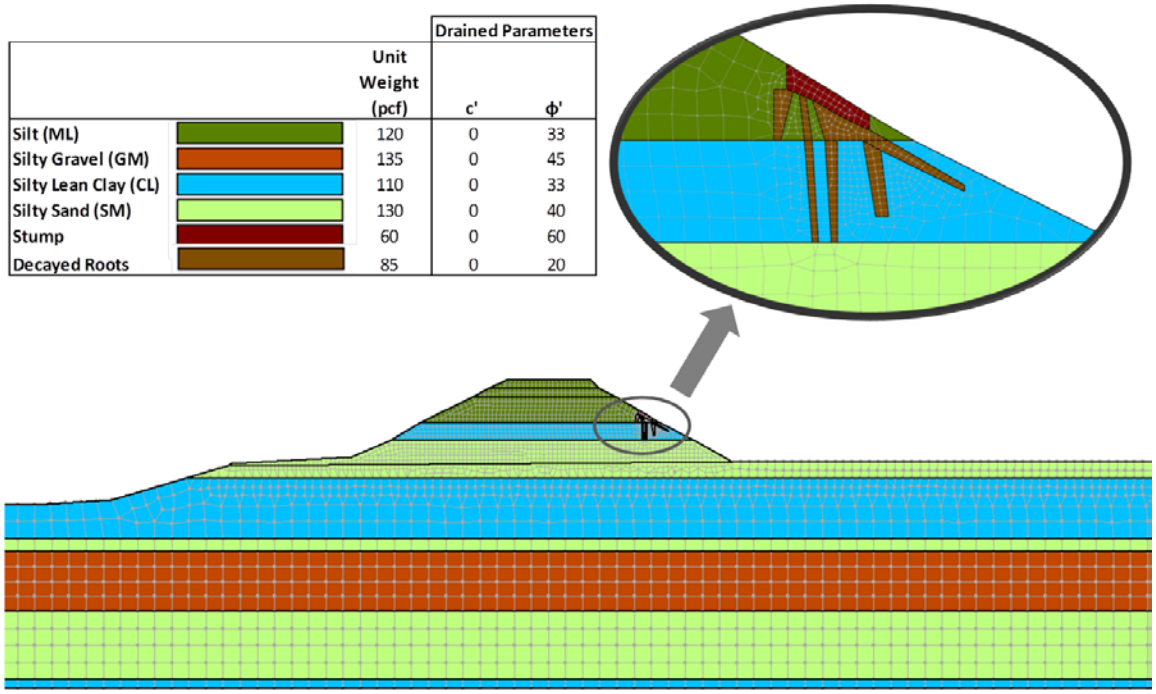

Figure 3-23. Conceptual levee section representative of the test site.

3.4.2 Results

The effect of a decomposing root system was explored based on the conditions noted above. Figure 3-24 presents factors of safety at a cross section extending through the root system of the decomposing stump as well as a similar section without a stump. Steady state seepage conditions were generated based on a waterside flood condition at a constant total head of 40 feet (12 ft below the levee crown) and these conditions were ~~input~~ into the slope stability model. The water surface within the levee embankment has not risen to the level of the root system and therefore pore water pressure differences between the two ~~models~~ are minimal within the slide circle. Both show factors of safety of 1.34 for similar slide circles.

In Figure 3-25, the levee section is modeled with a root system acting as a barrier~~,~~ acting as a drain or absent. These models consider a steady state water level at Elevation 50 ft (2 ft below the levee crown). Results show factors of safety are lowest (FS = 1.16) when the root system acts to block flow. Pressures build behind the blockage, reducing frictional strength due to decreased effective stress. In the case where the stump acts as a drain, the water surface is drawn down, reducing pore water pressures, increasing frictional shear strength, and increasing the factor of safety (FS = 1.33) against slope instability. When no stump is present, the factor of safety against instability was calculated to be 1.26. Other mechanisms of failure, such as the change in exit gradients due to the stump, were not evaluated as part of this effort. When the root system acts as a series of voids open to the downstream slope, high seepage exit gradients may present a more important failure mechanism than slope stability ~~(i.e. piping)~~.

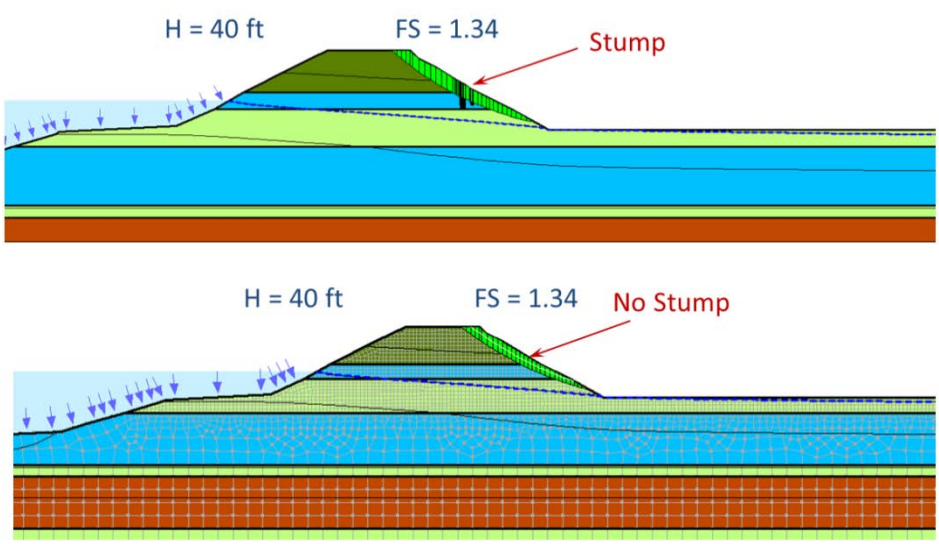

Figure 3-24. A comparison of simulations with and without a stump yields ~~factors of~~ similar factors of safety for similar slide circles.

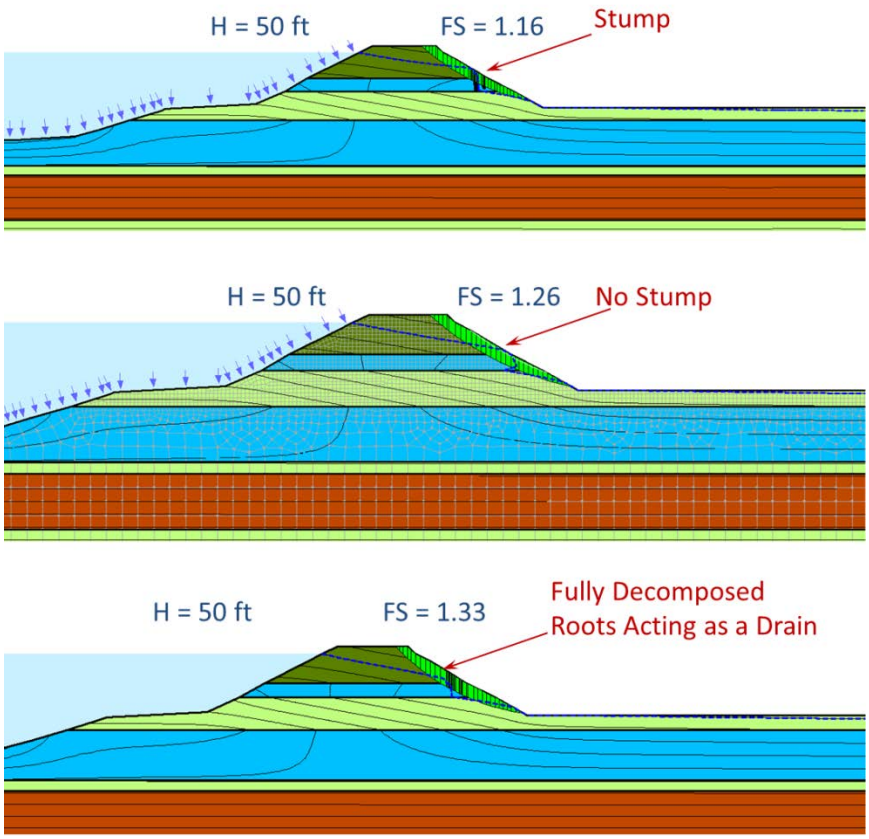

Figure 3-25. Total hydraulic head is held at 50 feet on the waterside. Three models are compared showing factor of safety with a low permeability stump and root system, no root system, or a fully decomposed root system acting as a series of voids.

4 CROWN TRENCH SEEPAGE TEST: TWITCHELL ISLAND

4.1 INTRODUCTION

A detailed description and analysis of the Crown Trench Seepage Test at Twitchell Island in Rio Vista, California is provided in the third volume of this series and will not be reiterated in detail herein. The test involved construction of two centerline trenches (a control and a tree trench) extending 8 feet in depth through a ~~bypassed~~ levee along the Sevenmile Slough on the north side of Twitchell Island. The trench was filled with gravel and water was pumped in and held at a constant head during the initial 4 day primary flow phase of the test. After the primary flow test, the tree trench was turned off and the control trench maintained with a constant head of water as instruments in this line had failed to saturate.

Three primary and two supplemental instrumented cross sections were identified to ~~establish~~ wetting front and flow patterns through the study area. The study area included a landside tree at primary instrument Line A and supplemental Line D, a waterside tree at primary instrument Line B and supplemental Line E, and a control section at Line C as shown on Figure 4-1.

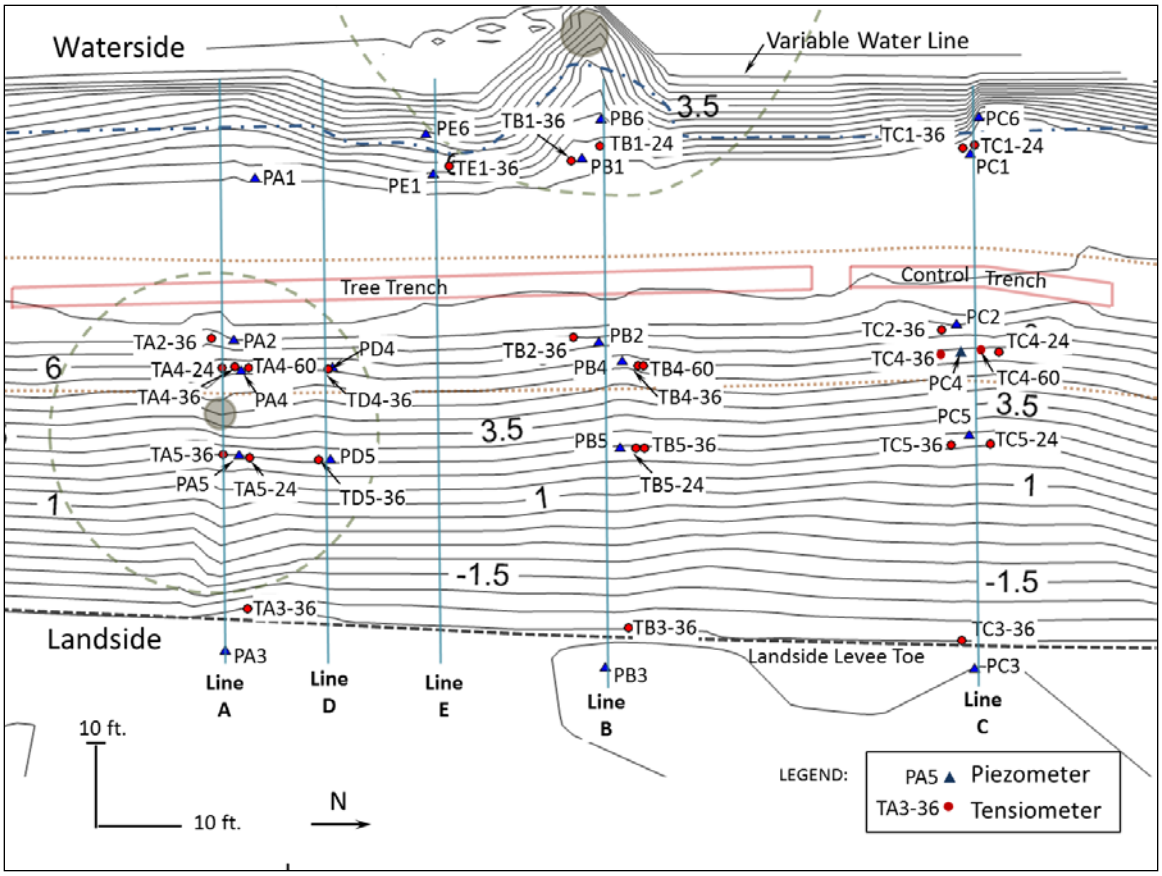

Figure 4-1. Site and instrument layout plan.

Landside flow patterns were found to be heavily influenced by (1) macroporosity associated with burrowing activities, and (2) site stratigraphy and heterogeneity. Burrowing activity was identified in the vicinity of the landside oak tree (instrument Line A) as well as an area north of the control instrument Line C. Seepage modeling will explore this possibility. The progression of the wetting front at instrument Line C appeared to be redirected midslope such that many instruments did not saturate. Contouring in the low permeability layer may have redirected water.

Deformations were observed on the waterside crown road and slope during the flow phase. Cracks are summarized as follows:

- Cracking between control and tree trench: Crack began opening a little over 2 hours into the flow test, before trenches were full. The crack peaked in size 13 hours into the test and began to shrink after 15 hours.

- Older and fresh cracking observed at the top of the waterside slope: A fresh crack was buried under a ~~waddle~~ and leaves near instrument line B and was discovered about 52 hours into the flow test. The time that the crack opened ~~in~~ not known but movement~~s~~ continued throughout the flow test. Older cracking was observed at the top of slope to the south.

- Pavement cracking (Stations TT 55 to 90): Minor cracking was observed near southern end of tree trench~~. The cracking was observed~~ 25.5 hours into the flow test.

- Cracking in the area of the tree rootball after failure of the tree (Stations TT 16-28): Cracking was observed ~~approximately 39 hours into the flow test,~~ coincident with the discovery of the tree failure.

An understanding of the role that the tree may have played in the waterside deformations of the levee is explored through seepage and seepage-induced slope instability simulations. A progressive failure scenario will be considered where the influence of the tree is evaluated under the following scenarios:

1) A large failure plane extending back to the control and tree trenches using transient pore pressures early in the flow test when movements were first observed

2) A smaller failure envelope extending from the crack at the top of the waterside slope

3) A failure scenario including only the root ball

4) A failure scenario of the embankment movement without the presence of a tree or reinforcing elements

4.2 INTERPRETED SECTIONS AND MESH DESIGN

Cracks indicative of levee deformation were observed at numerous locations along the levee crown and waterside slope during the Crown Trench Seepage Test at Twitchell Island in Rio Vista, California. Based on the patterns of cracking, four possible waterside slide and two landside failure scenarios were identified for analysis (Shriro, 2014). Figure 4-2 illustrates the failure scenarios selected for modeling.

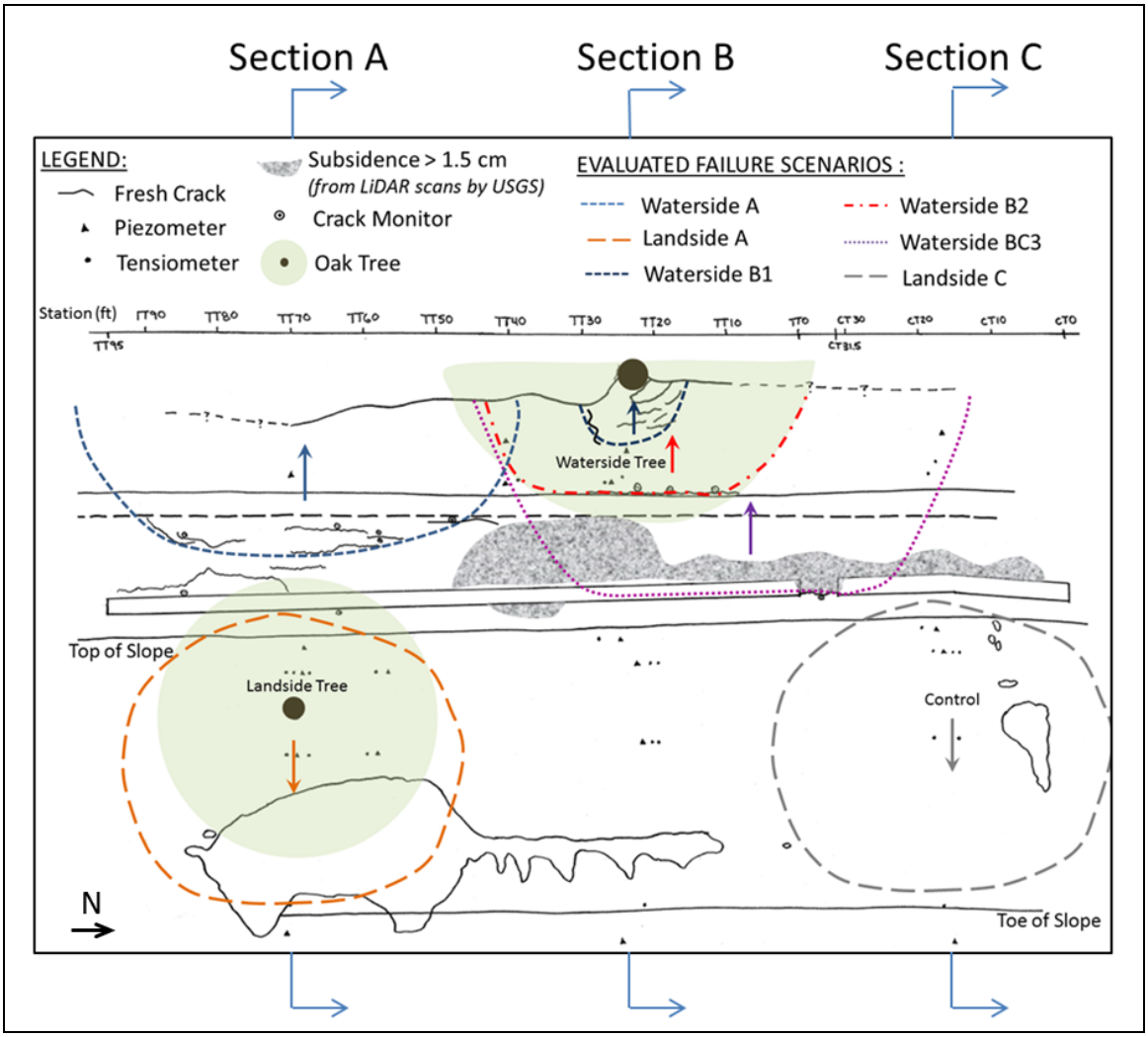

Figure 4-2. Four waterside and two landside failure scenarios are delineated for analysis.

Slope/W, the slope stability module of the Geostudio software package, is capable of analyzing two-dimensional cross sections for slope stability with limit equilibrium analysis. Isolated levee trees and their root systems are three dimensional problems. Mass averaging of 2D FS values of multiple 2D sections provides a reasonable approximation of the 3D FS (e.g., Seed et al., 1990). A simplified method is explored through mass averaged factors of safety over the slide mass as follows:

$$FS_{3D} = \frac{\sum_{i=1}^{i=n}(FS_{2D})_i(m)_i}{\sum_{i=1}^{i=n}(m)_i}$$

Three basic cross sections based on the interpreted geometry of the Twitchell Island test site, as discussed in Chapter 3, are presented as Figure 4-3, Figure 4-4, and Figure 4-5. These three basic sections are used in all models, varying the loading and reinforcement conditions the scenarios, as appropriate.

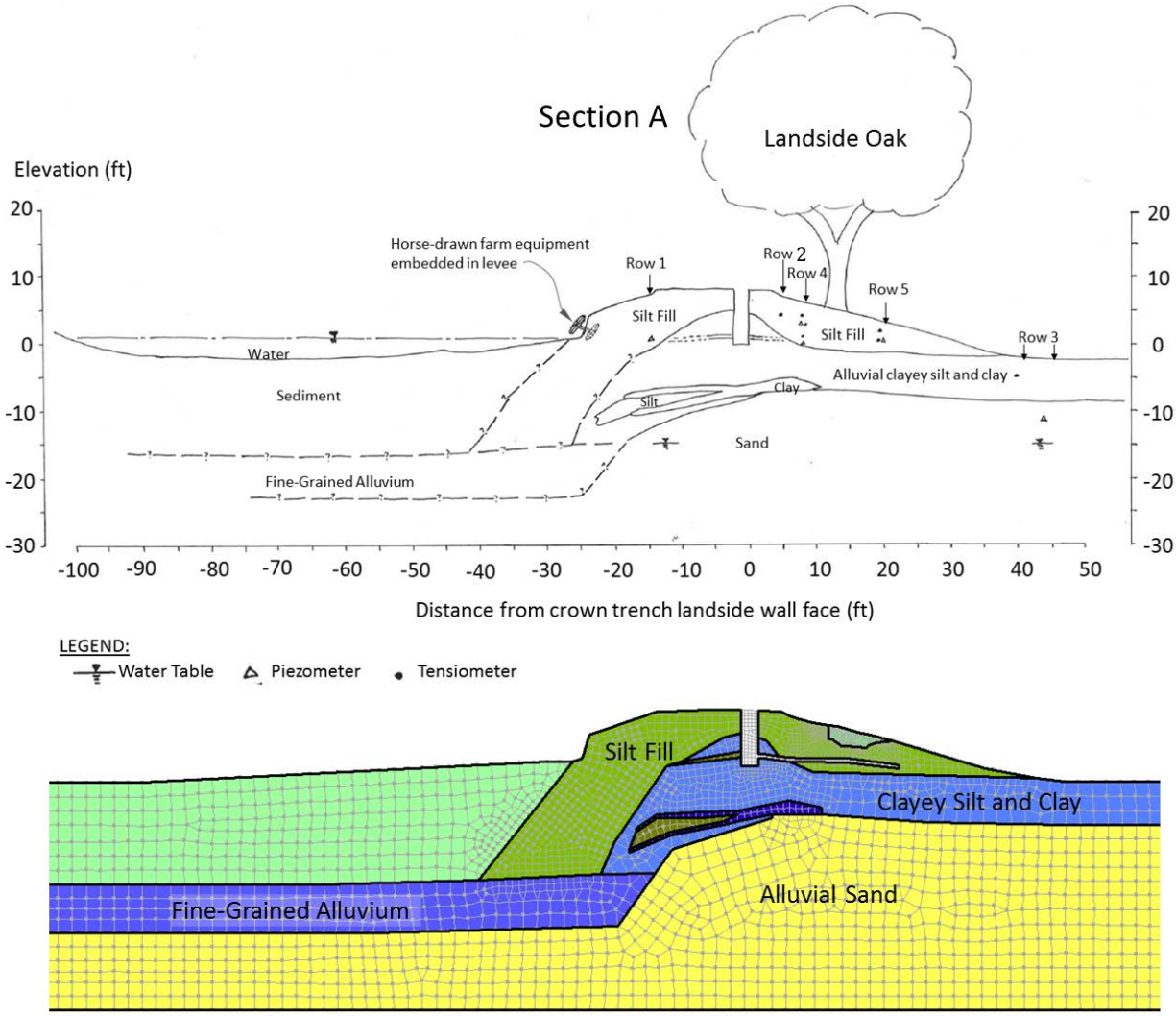

Figure 4-3. Section A interpreted section with model mesh.

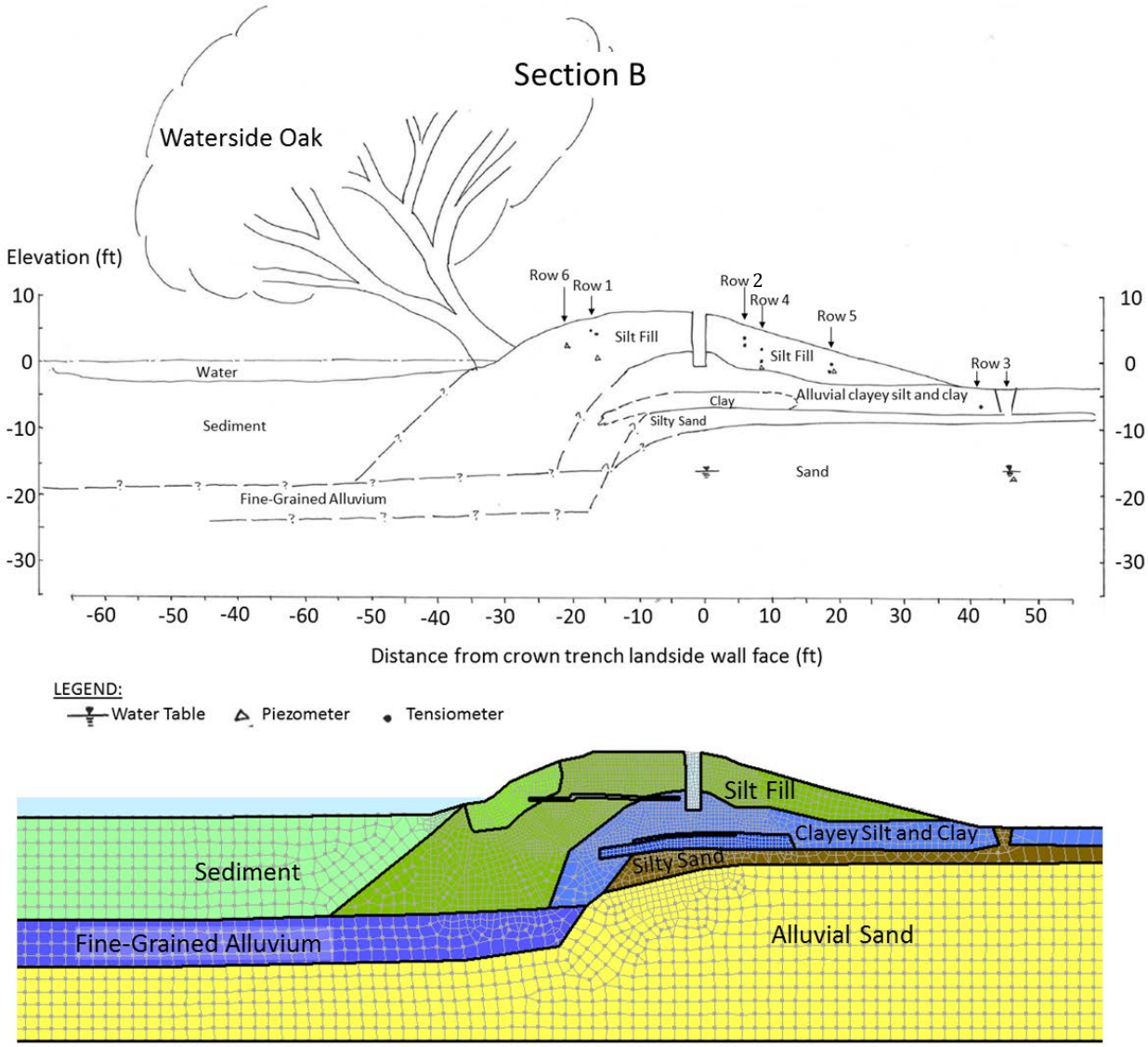

Figure 4-4. Section B interpreted section with model mesh.

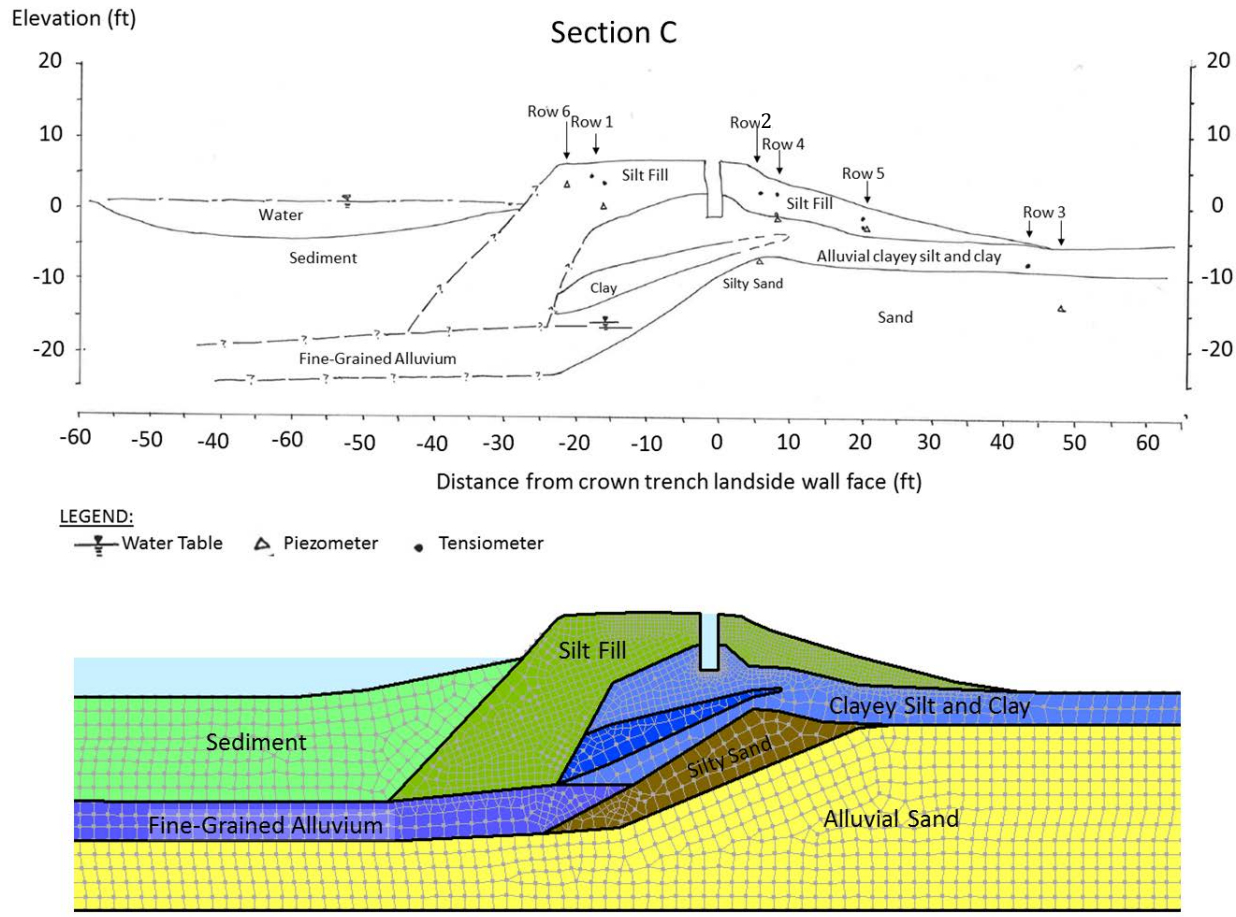

Figure 4-5. Section C interpreted section with model mesh.

4.3 SEEPAGE MODELING

Seepage modeling was performed to better understand patterns of seepage and flow on the landside during the flow test as well as for input into slope stability models. Deformations were observed within the levee before steady state pore pressures were reached ~~within the levee~~. As such, transient conditions were modeled and considered in stability analyses.

The first step of the seepage modeling component of the study consisted of estimating hydrogeologic properties of the different layers on the profile, and calibrating these values to the recorded instrument data. Calibration was performed using the data from instrument Line C, as it did not have a root system that would increase uncertainty in the calibration process. After a reasonable agreement between simulation and instrument data was achieved, the soil properties were fixed and used for modeling of other sections and analysis scenarios.

4.3.1 Hydraulic Properties and Calibration

Saturated hydraulic conductivities were initially assumed based on recommendations in DWR's urban levee guidance document (URS, 2014). Unsaturated behavior was

represented by creating SWCCs for the main soil types in the profiles and assuming Van Genuchten coefficients typical of each soil type. After the initial set of properties were defined for the layers in Section C, transient analyses to simulate the field test instrument data were performed to calibrate the assumed properties. No specific laboratory tests were performed for the Twitchell Island site.

The transient calibration model started from an initial steady state simulation with the pre-test water level at -15 feet located along the vertical edges of the model (approximately 1000 ft away from the levee centerline), as measured by piezometers prior to the start of the centerline trench; and a canal water elevation of 1 ft (Figure 4-1). After the initial pore water pressure field was established, the initial suction values at each instrument location were compared to the instrument data. A slight adjustment of the initial water levels was needed to obtain a reasonable match between simulation and instrument data. Similar to the Cal Expo models described before, the SWCCs were truncated so realistic values of initial hydraulic conductivity were calculated by the software.

A transient simulation applying a head of 7.25 ft inside the excavated trench followed the generation of initial conditions to simulate the arrival of the wetting front to the different instruments in the section. Values of saturated hydraulic conductivity, saturated volumetric moisture content, air-entry value and slope of the SWCC were varied during the calibration process until a satisfactory calibration was achieved for a number of instruments in the profile. Table 4-1shows the final parameter values obtained from the calibration process.

Table 4-1. Soil properties used for flow models.

Material	Color	Ksat (cm/s)	θ[1] sat	θ res	a (psf)	Ky/Kz
Alluvial Sand		$1x10^{-3}$	0.3	0.05	0.5	0.33
Old clay levee		$1x10^{-6}$	0.42	0.1	100	0.2
Weak clay		$1x10^{-6}$	0.42	0.1	100	0.2
Sediment		$1x10^{-8}$	0.42	Assumed saturated		1.0
Levee silt		$5x10^{-4}$	0.4	0.1	5	0.2
Silty sand		$5x10^{-4}$	0.35	0.1	20	0.3

[1]Volumetric water content, [2]coefficients used in the Van Genuchten (1980) equation for characteristic curves.

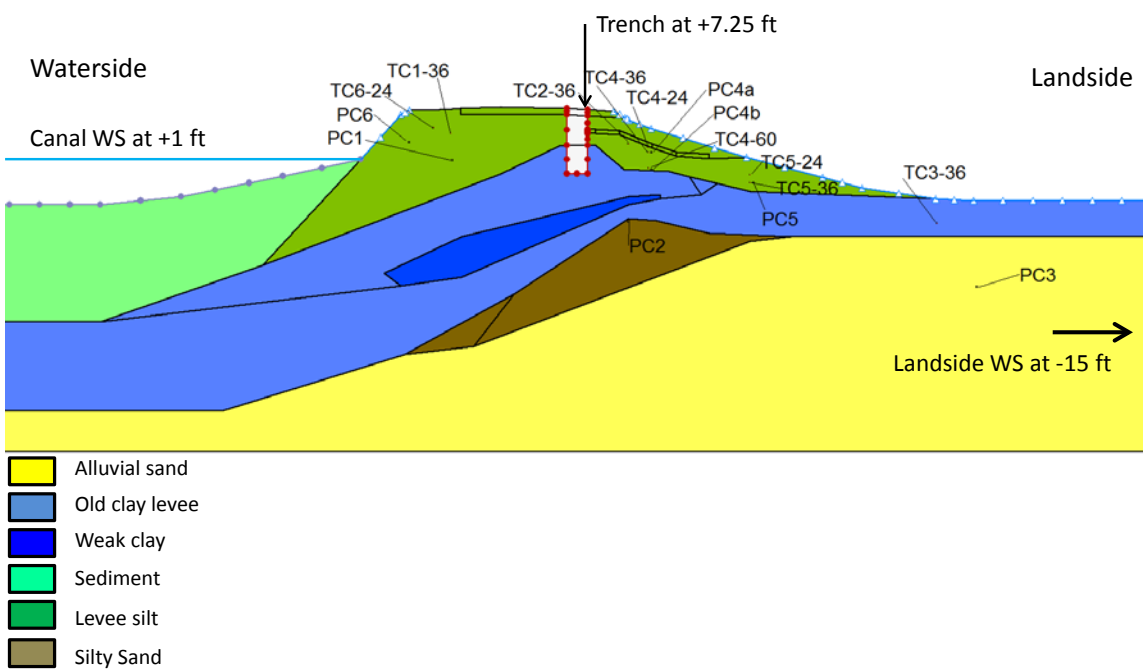

Figure 4-6. Instrument line C showing instrument location and boundary conditions.

The entire set of instrument data for Line C is shown on Figure 4-7, and calibrations for each instrument are shown on Figure 4-8 to Figure 4-9.

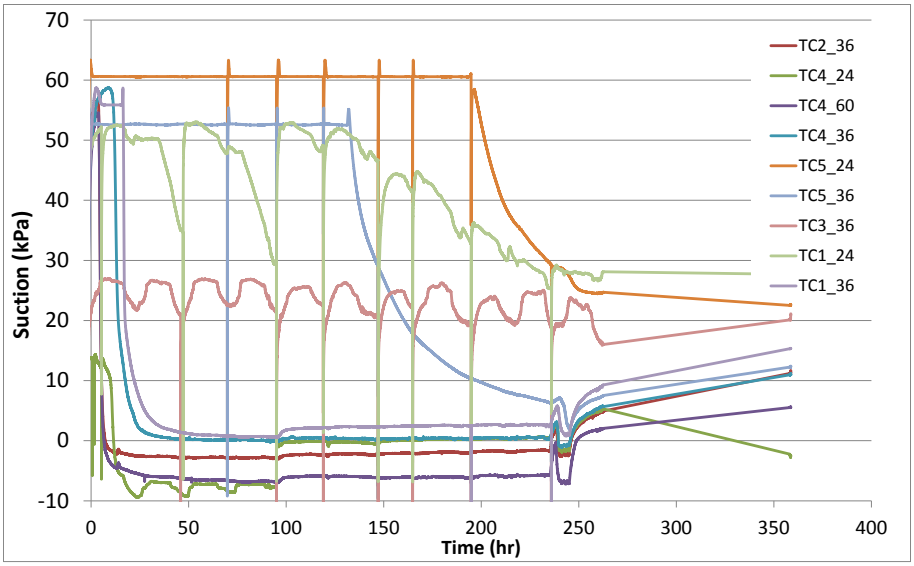

Figure 4-7. Instrument line C tensiometer data.

~~Calibration results for each instrument are shown on Figure 4-8 and Figure 4-9.~~ Calibration was successfully achieved for instruments TC2-36, TC4-24 and TC4-60; instruments TC4-36, and TC1-36 despite having similar initial suction values to those recorded during the test, achieved saturation in approximately half the time in the simulation than in the field test. Suction values on the waterside slope were not accurately predicted by the simulations, likely due to uncertainties in soil layering in the profile, loose pockets and burrows. The model predicts that shallow soils are moister than ~~they were in fact~~ observed in the field. In the transient simulations the final properties used in these and subsequent analyses were based on calibrations with landside instruments, whereas the waterside instruments focused on matching accumulation of positive pore pressures in piezometers for input into stability models.

Instrument Lines A and B included ~~animal~~ burrows and root systems. The burrows were modeled ~~assigning~~ a high value of hydraulic conductivity to allow continuity in the mesh and fast transmission of hydraulic heads from one end of the burrow to the other. The root systems were modeled as regions with constant hydraulic conductivity using a lower value equal to 1/5 of the saturated value of conductivity of the surrounding levee material.

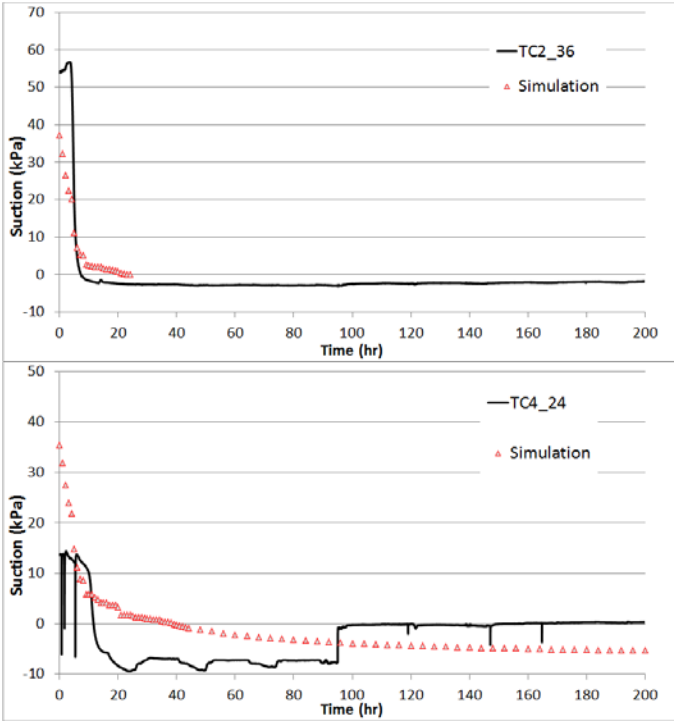

Figure 4-8. Instrument line C devices TC2-36 and TC4-24

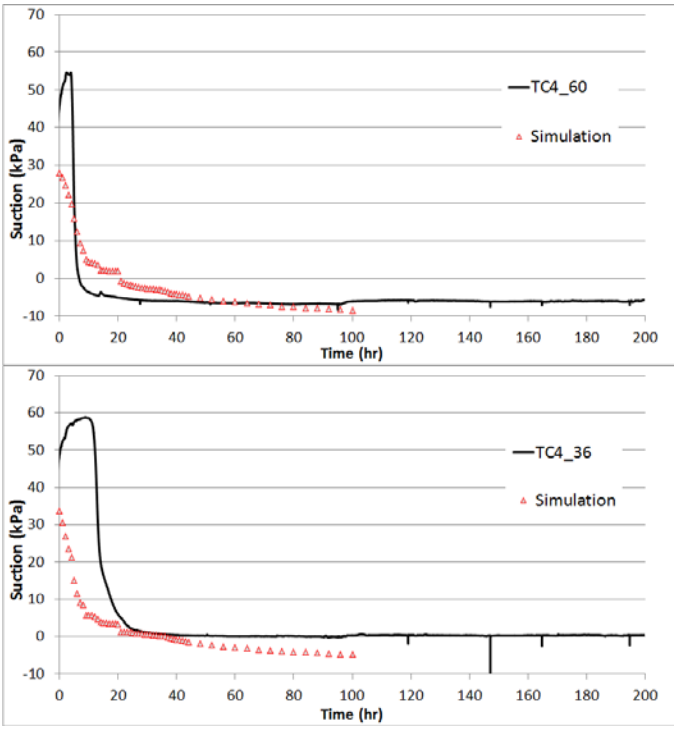

Figure 4-9. Instrument line C devices TC4-60 and TC4-36

Instrument Line B (Figure 4-10) includes a root zone on the waterside slope and a discontinuous ~~animal~~ burrow along the waterside half of the embankment. The transient simulation considers the same boundary conditions and time steps as control line C, results are shown on Figure 4-11and Figure 4-12. Similar to instrument line C, this section shows faster saturation of instruments on the waterside slope, given the much higher initial head condition of +1 ft on the canal side (compared to -15 ft on landside), making initial conductivity values on the waterside slope much higher and thus saturation times shorter than on the landside slope.

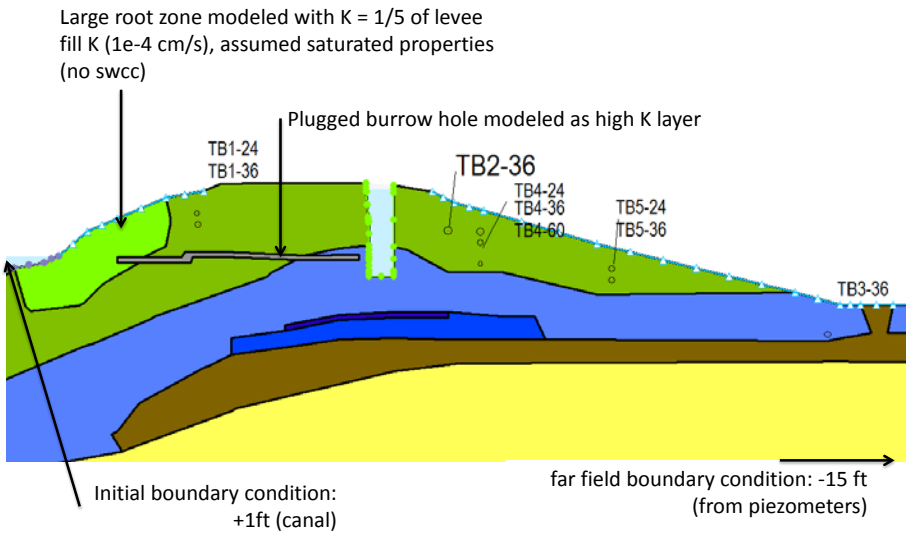

Figure 4-10. Instrument line B section and boundary conditions

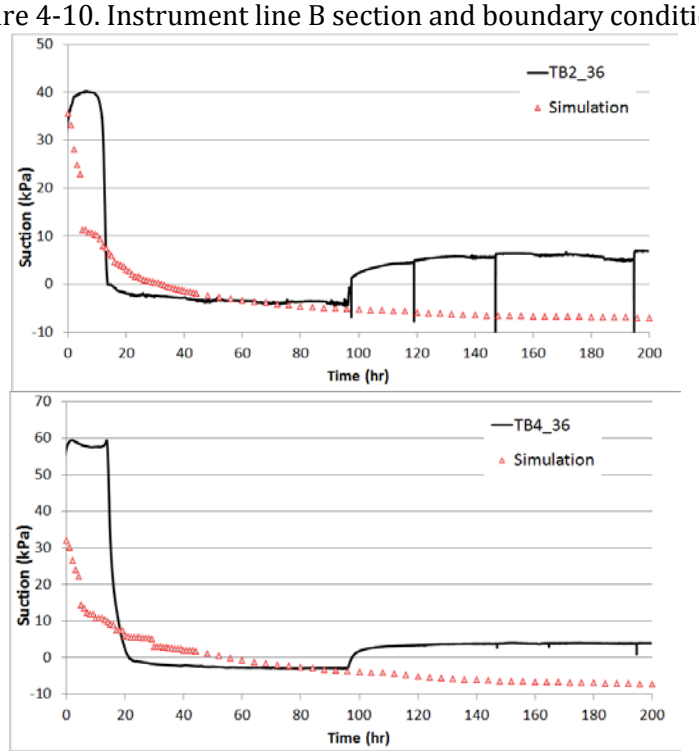

Figure 4-11. Instrument line B devices TB2-36 and TB4-36

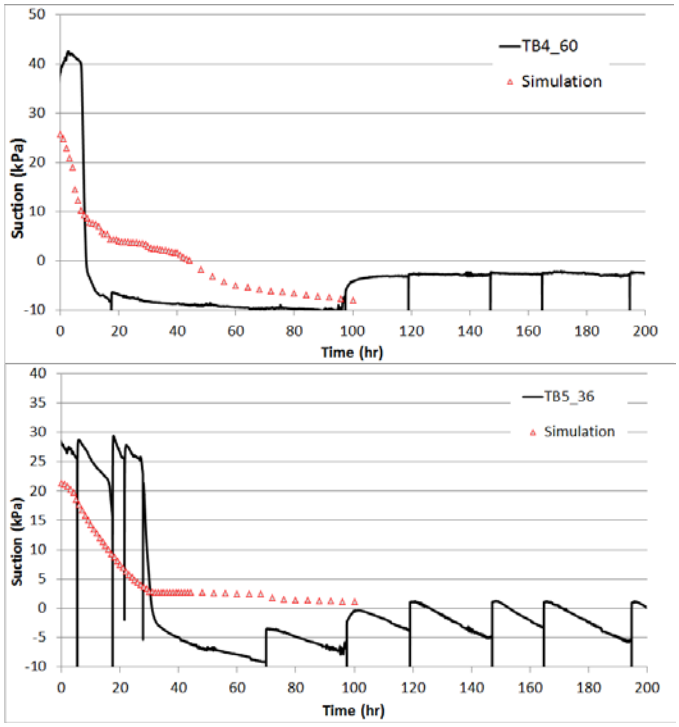

Figure 4-12. Instrument line B devices TB4-60 and TB5-36

Instrument Line A (Figure 4-13) includes a root zone on the waterside slope and a discontinuous ~~animal~~ burrow along the waterside half of the embankment. The transient simulation considers the same boundary conditions and time steps as control line C. The results are shown on Figure 4-14 through Figure 4-16. Similar to instrument line B, this section shows faster saturation of instruments on the waterside slope, given the much higher initial head condition of +1 ft on the canal side (compared to -15 ft on landside), making initial conductivity values on the waterside slope much higher and thus saturation times shorter than on the landside slope.

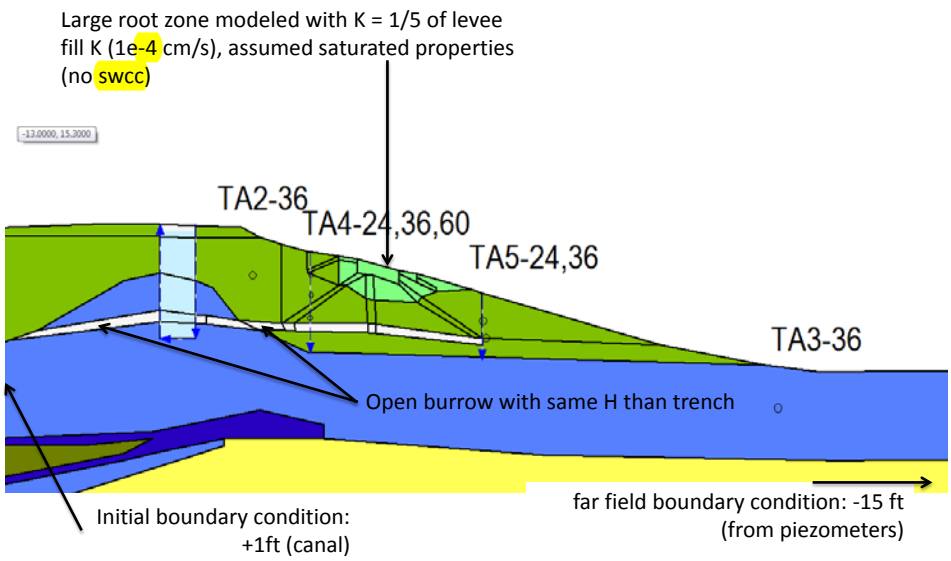

Figure 4-13. Instrument line A section and boundary conditions

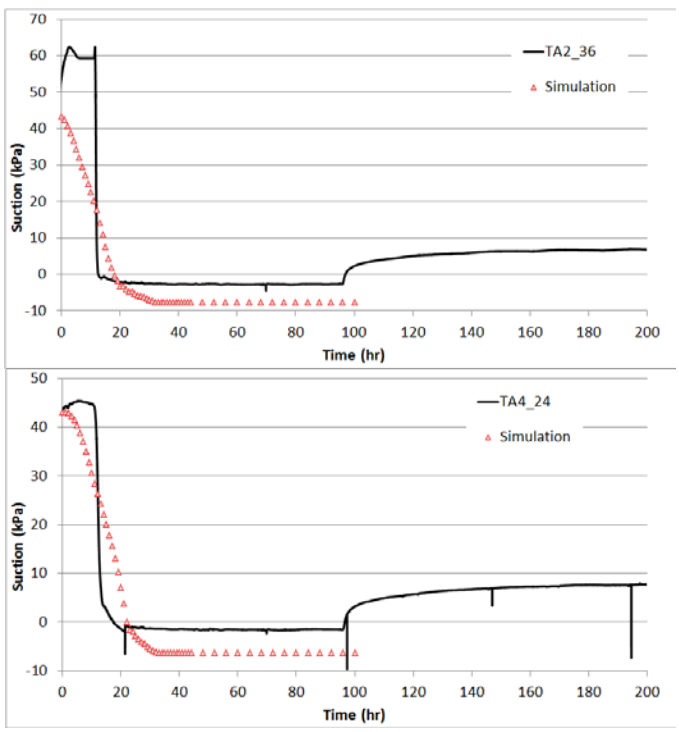

Figure 4-14. Instrument line A devices TA2-36 and TA4-24

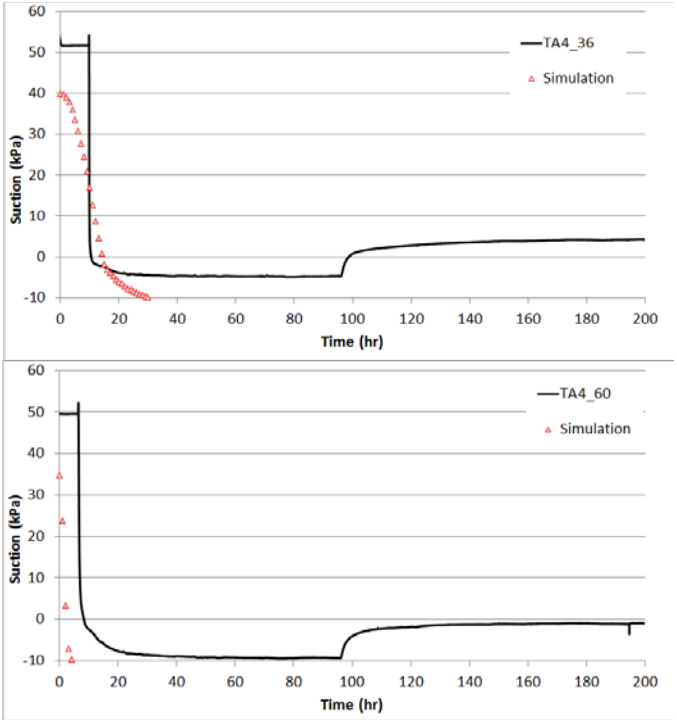

Figure 4-15. Instrument line A devices TA4-36 and TA4-60

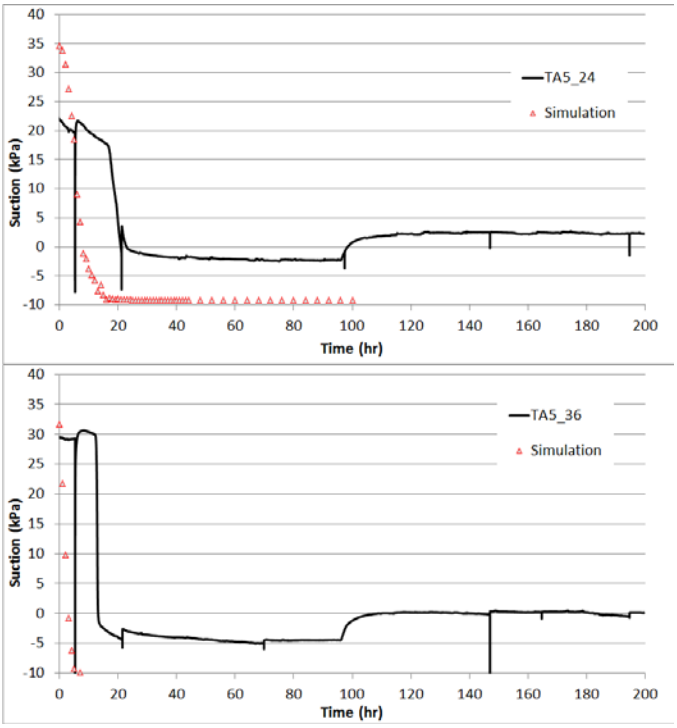

Figure 4-16. Instrument line A devices TA5-24 and TA5-36

Results of the 2D calibrations for the instrument lines at the Twitchell island test site were compared to instrument data and field observations of seeps on the landside levee slope. These 2D models employed a uniform region with a value of conductivity equal to roughly 1/5 of the saturated conductivity of the surrounding levee, obtaining an acceptable calibration for most instruments and a ~~similar effect than~~ observed in the Cal Expo test. These models were used as input for slope stability models described in Shriro (2014).

4.3.2 Seepage Modeling at Section A

4.3.2.1 Initial and Boundary Conditions

Initial conditions for Section A consider a slough water elevation of +1 ft, and a far-field phreatic level at -15 ft. Boundary conditions for the transient simulation are the 7.5 ft inside the trench and the same slough and far-field conditions (Figure 4-17).

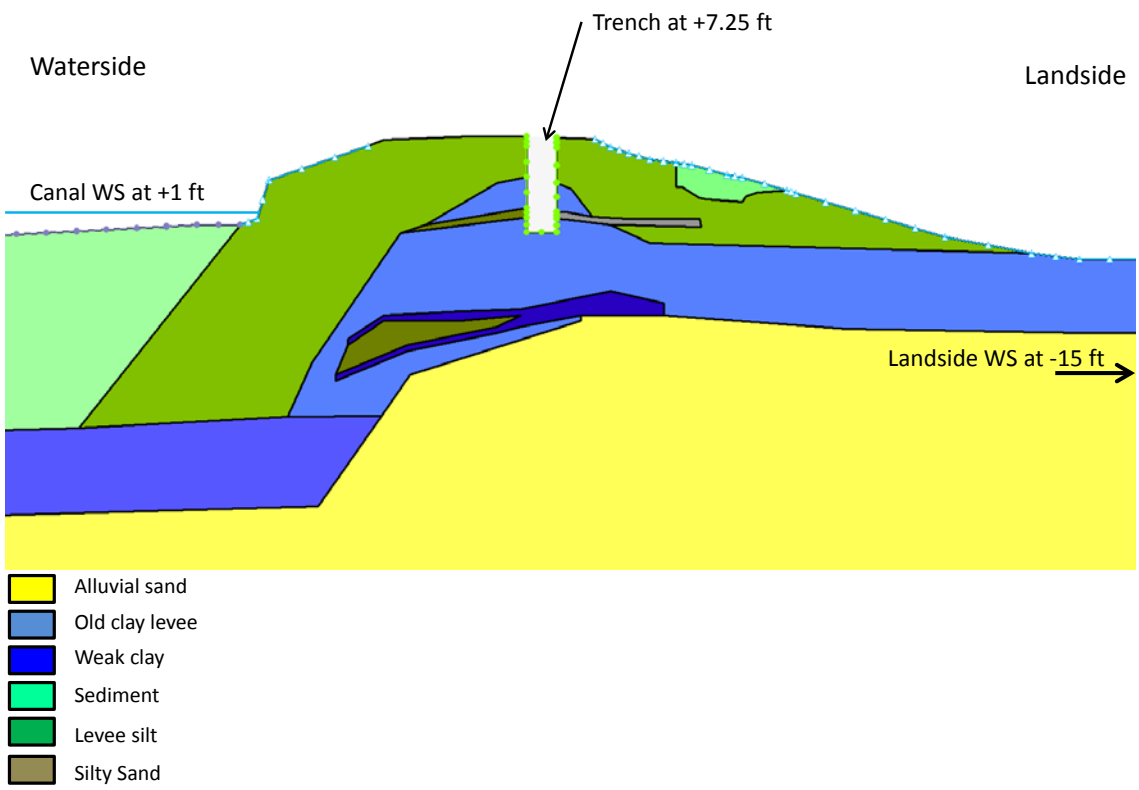

Figure 4-17. Section A layers and boundary conditions.

4.3.2.2 Transient and Steady State Seepage

A transient simulation considered the left (waterside) portion of the burrow filled with material to simulate a soil plug, and the right (landside) segment of the burrow open to the heads from the excavated trench and extending to about the center of the root mass (Figure

4-19a). Results of the transient simulations used for calibration of hydraulic properties are shown on Figure 4-20 through Figure 4-27. The computed heads on the waterside slope are the same for both simulations, creating a wetting front extending radially out from the open burrow, but the effect of the plugged burrow limits the development of a saturation front for most of the simulated time. Additional steady state simulations performed are used as input for the slope stability analyses described in this Volume.

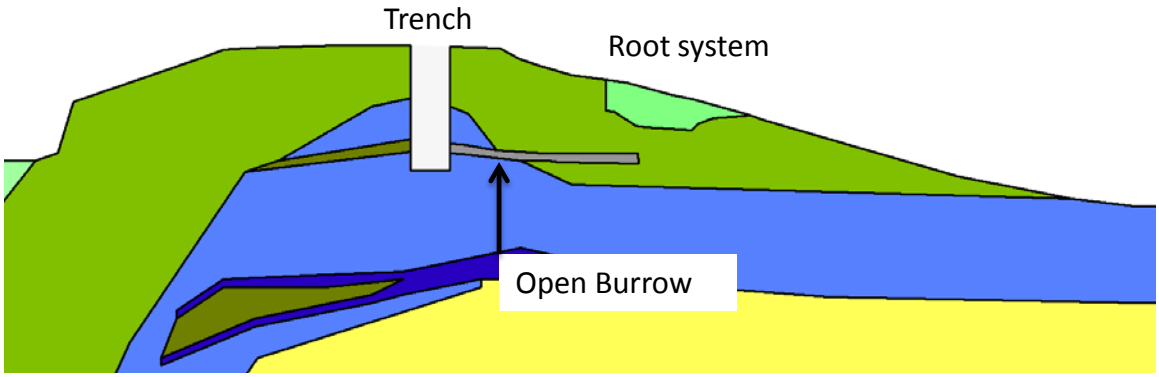

Figure 4-18. Section A transient analysis scenarios.

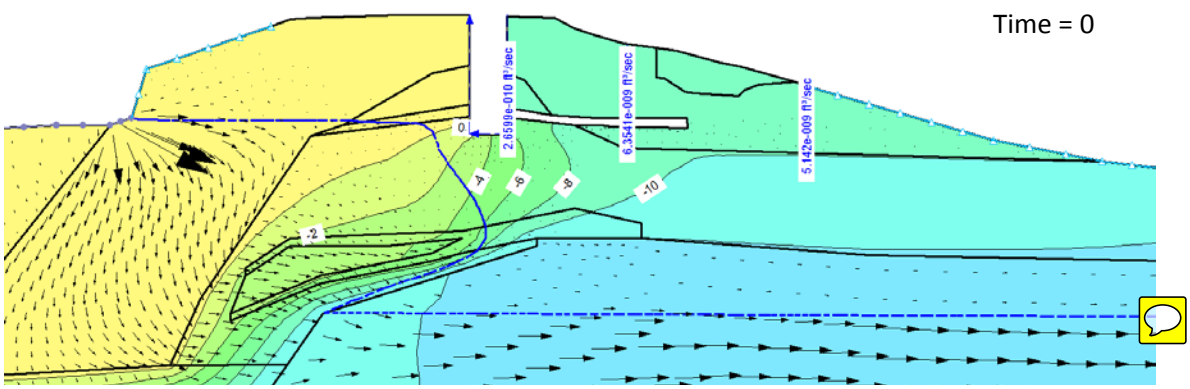

Figure 4-19. Section A transient analysis results, open burrow on landside. Simulation time 0 hours. Total head contours, 2 ft interval and flux sections ($ft^3/s/ft$) included in plot

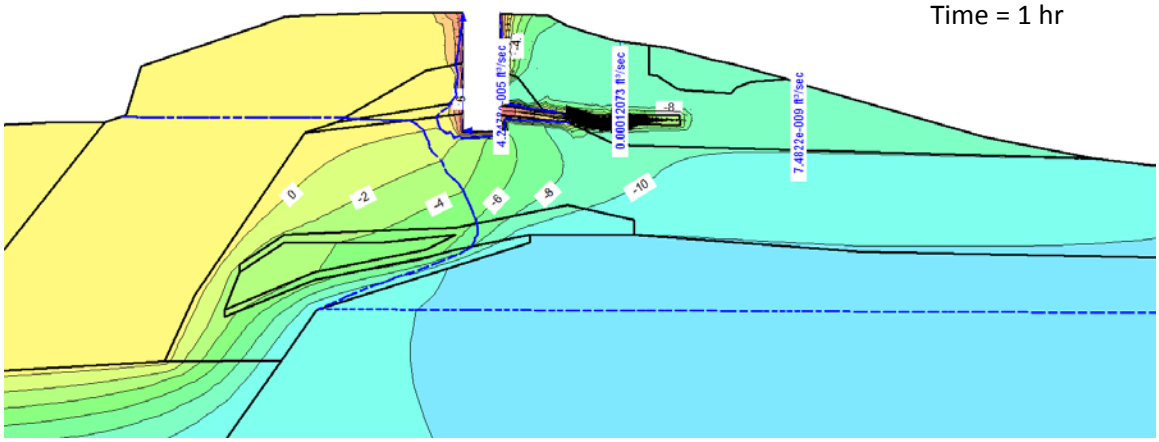

Figure 4-20. Section A transient analysis results, open burrow on landside. Simulation time 1 hour. Total head contours, 2 ft interval and flux sections (ft³/s/ft) included in plot

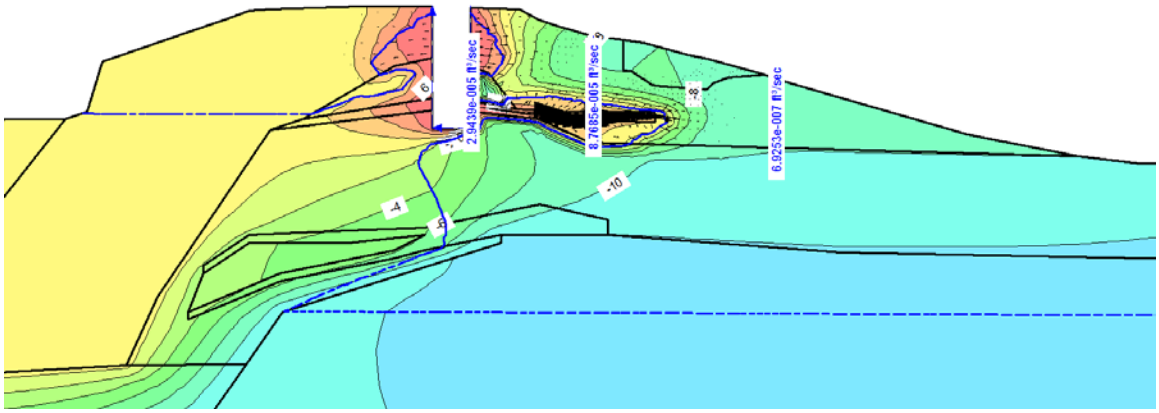

Figure 4-21. Section A transient analysis results, open burrow on landside. Simulation time 10 hours. Total head contours, 2 ft interval and flux sections (ft³/s/ft) included in plot

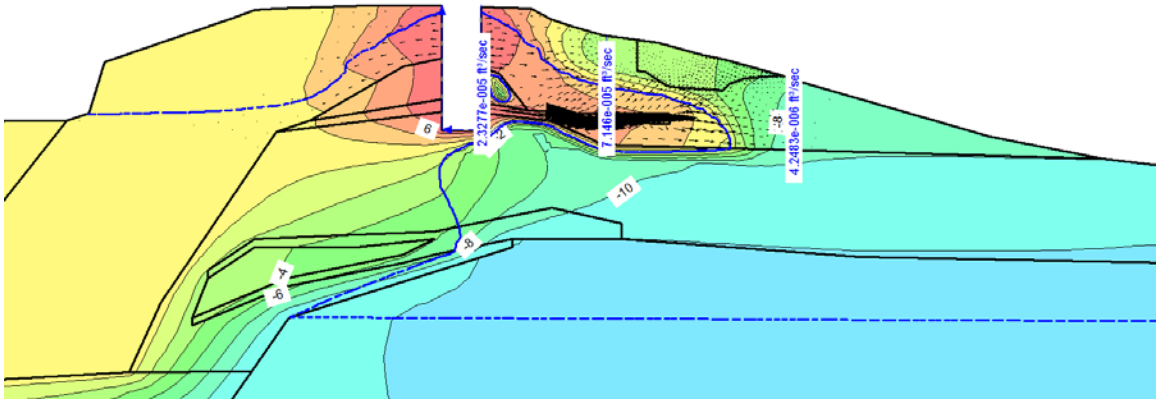

Figure 4-22. Section A transient analysis results, open burrow on landside. Simulation time 24 hours. Total head contours, 2 ft interval and flux sections (ft³/s/ft) included in plot

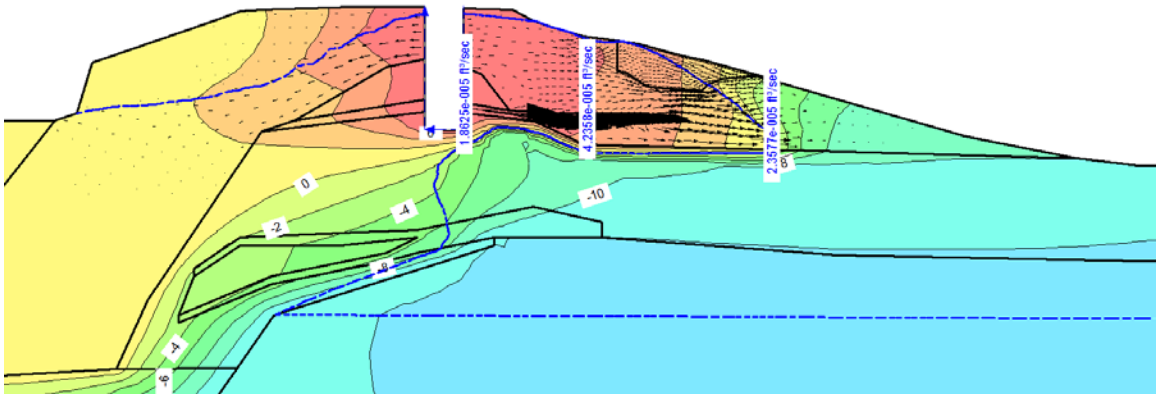

Figure 4-23. Section A transient analysis results, open burrow on landside. Simulation time 48 hours. Total head contours, 2 ft interval and flux sections (ft³/s/ft) included in plot

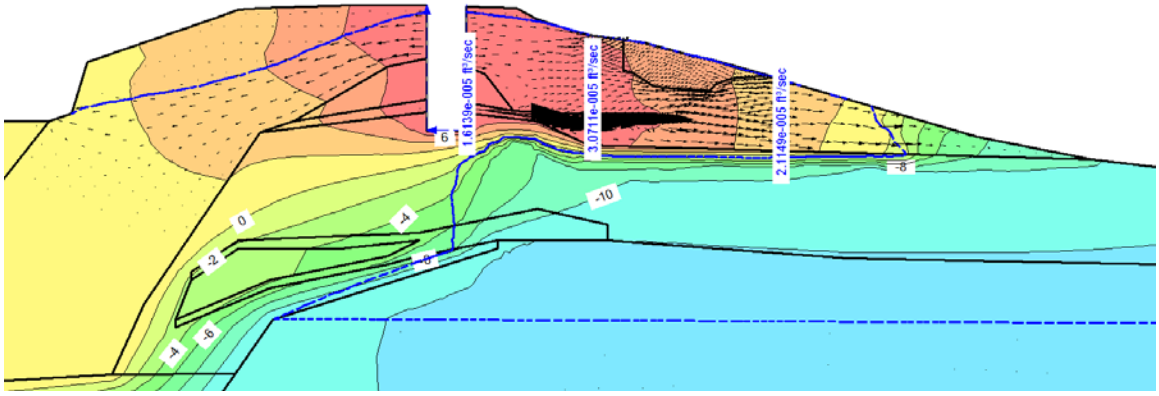

Figure 4-24. Section A transient analysis results, open burrow on landside. Simulation time 100 hours. Total head contours, 2 ft interval and flux sections (ft³/s/ft) included in plot

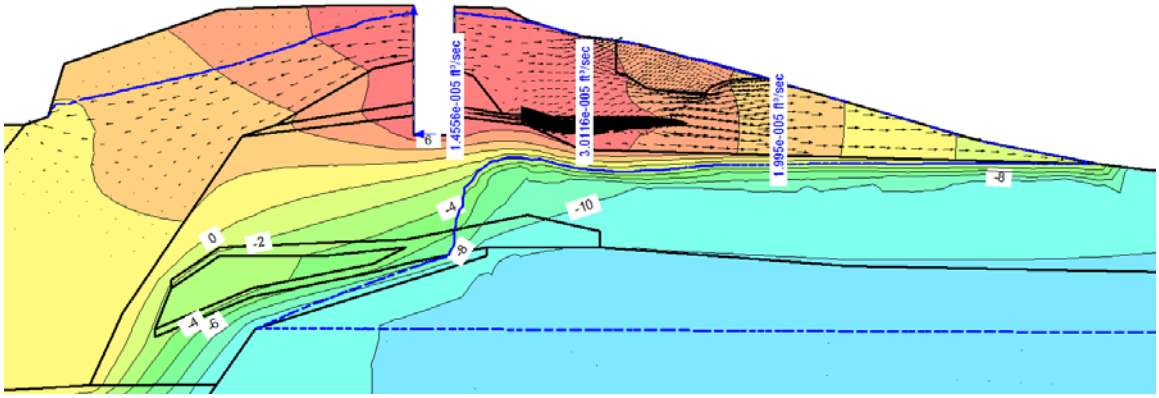

Figure 4-25. Section A transient analysis results, open burrow on landside. Simulation time 200 hours. Total head contours, 2 ft interval and flux sections (ft³/s/ft) included in plot

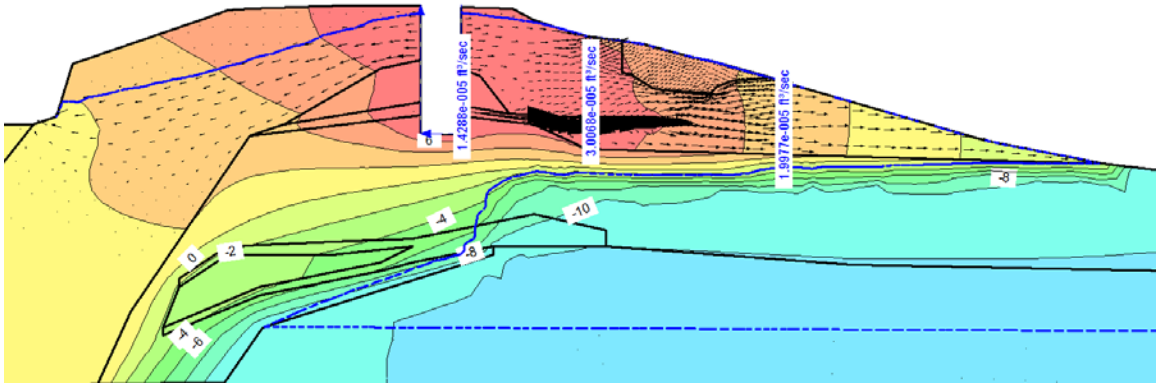

Figure 4-26. Section A transient analysis results, open burrow on landside. Simulation time 300 hours. Total head contours, 2 ft interval and flux sections ($ft^3/s/ft$) included in plot

Additional steady state analyses were performed for the following scenarios:

- Waterside inundation at El. +7 ft (Figure 4-28), with no ~~animal~~ burrow and varying the length of the burrow.
- Landside inundation at El. +7 ft (Figure 4-29), with no ~~animal~~ burrow and varying the length of the burrow.
- Test inundation at El. + 7.5 ft (Figure 4-30), with no ~~animal~~ burrow and varying the length of the burrow.

The models were constructed varying the length of open mammal burrows for input into slope stability models (Figure 4-18.)

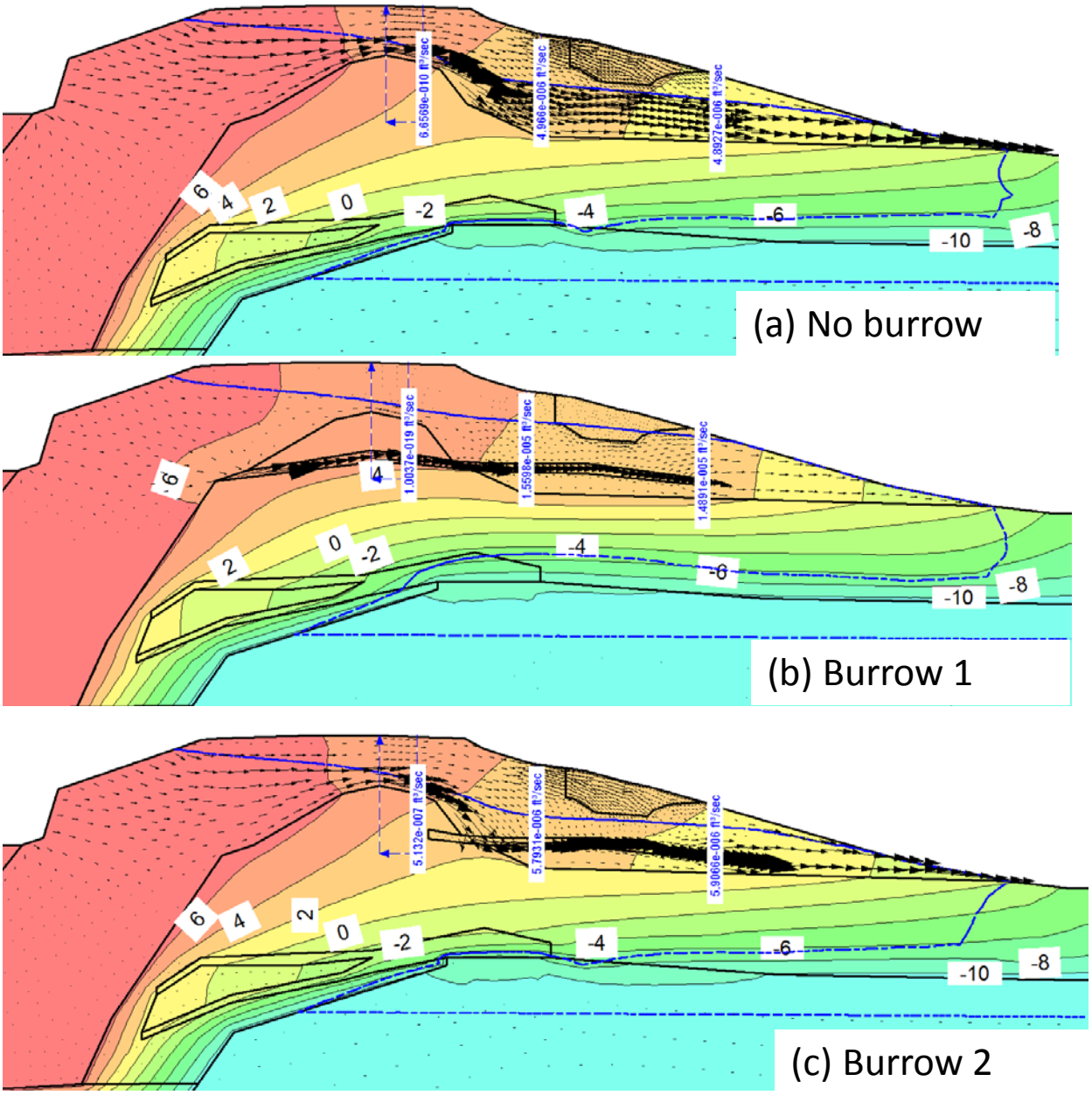

Figure 4-27. Section A waterside inundation steady state models.

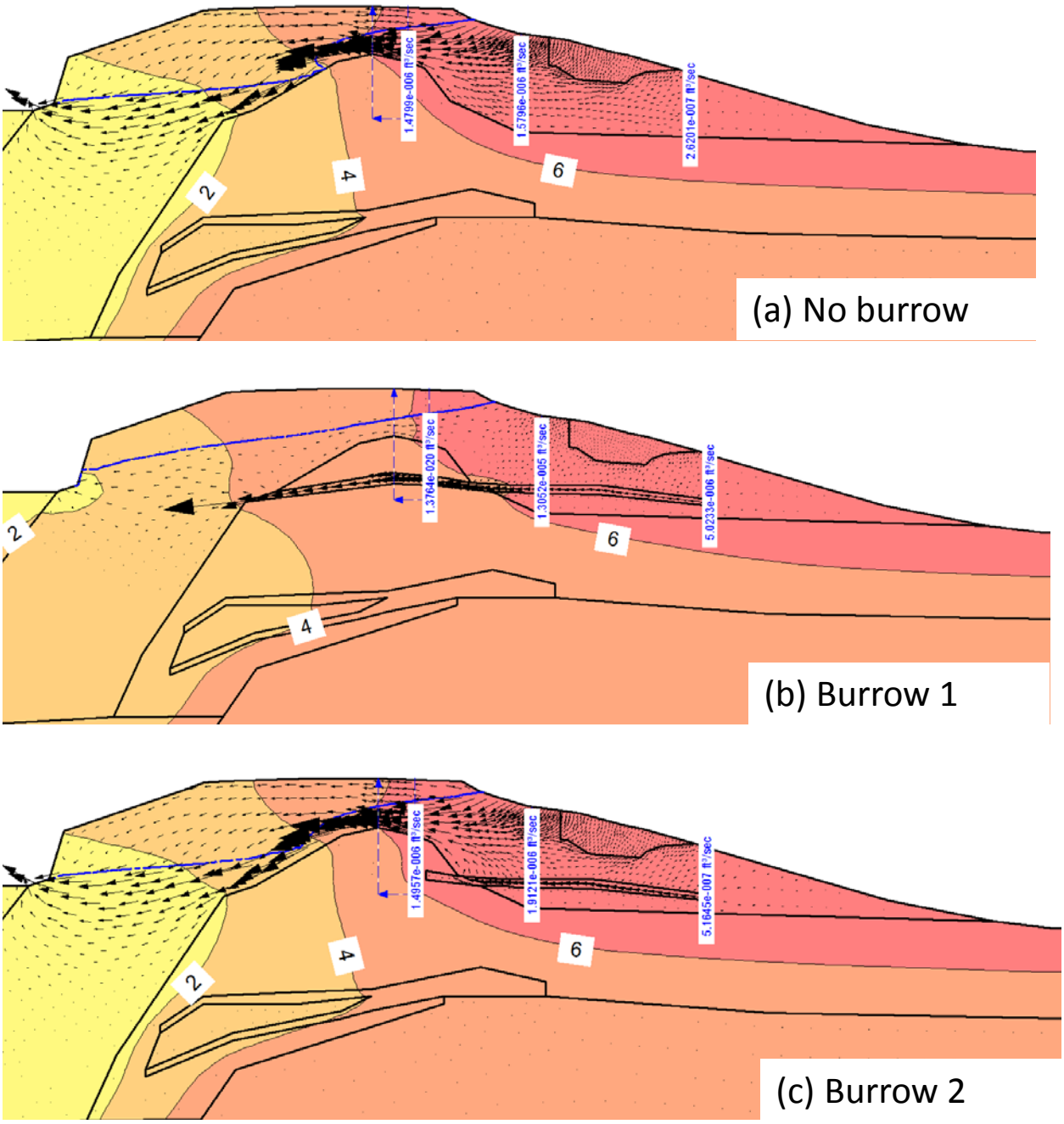

Figure 4-28. Section A landside inundation steady state models.

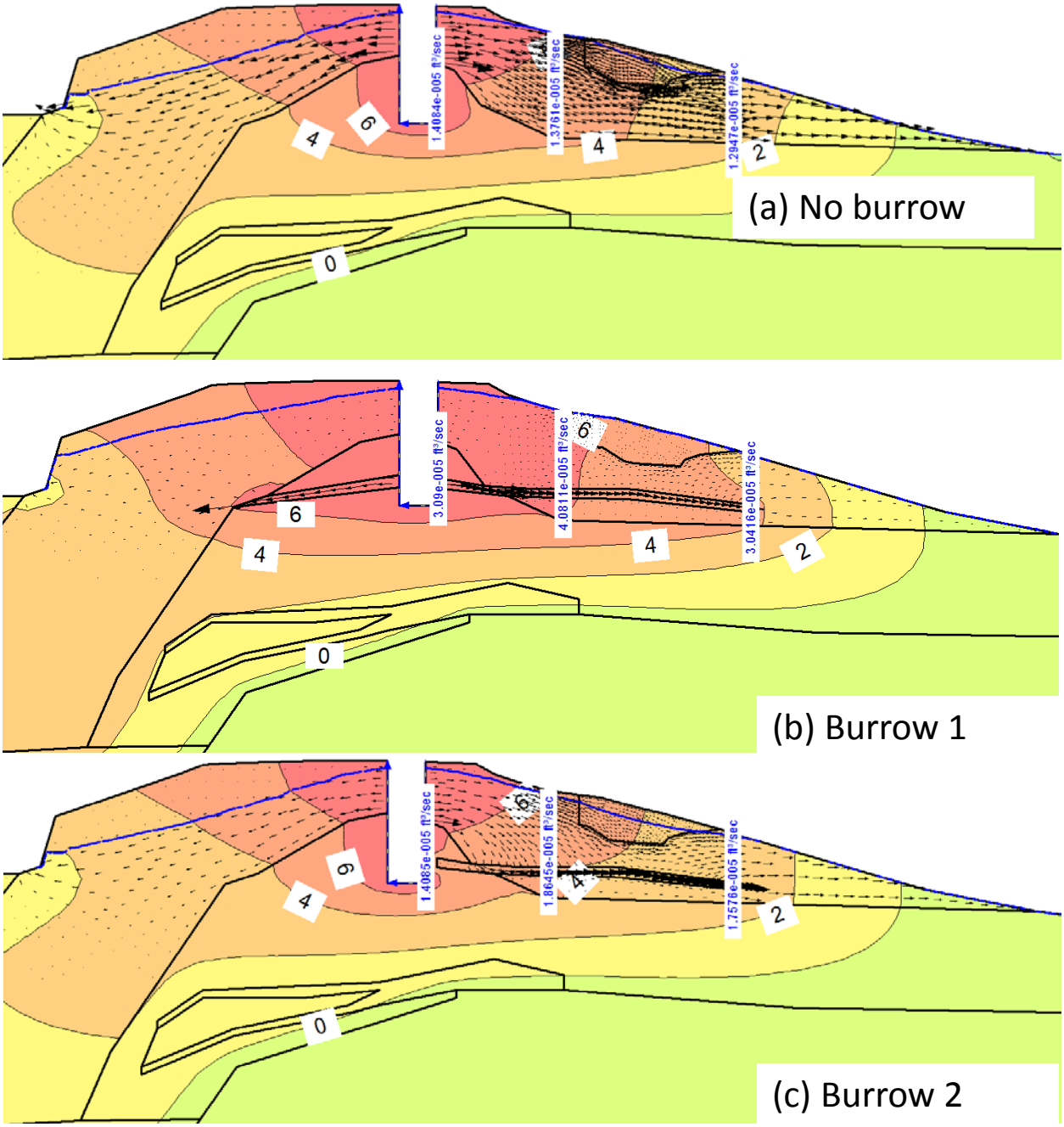

Figure 4-29. Section A centerline trench inundation steady state models.

4.3.3 Seepage Modeling at Section B

4.3.3.1 Initial and Boundary Conditions

Initial conditions for Section B consider a slough water elevation of +1 ft, and a far-field phreatic level at -15 ft. Boundary conditions for the transient simulation are the 7.5 ft inside the trench and the same slough and far-field conditions (Figure 4-31).

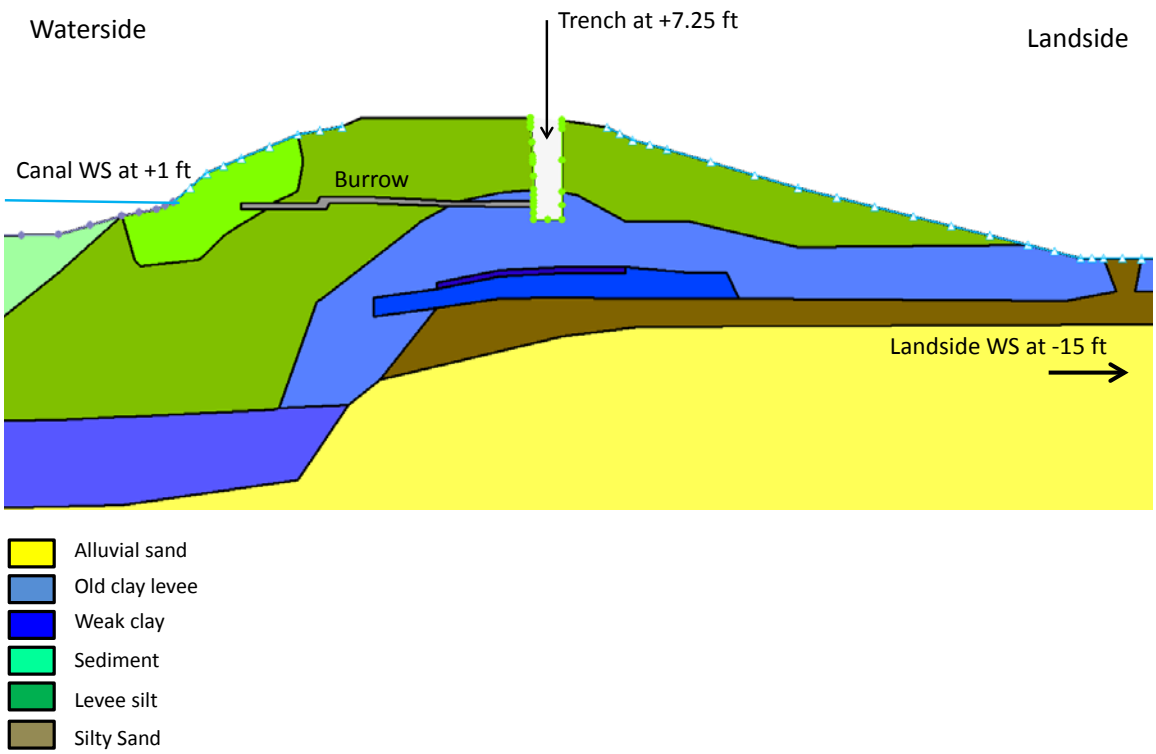

Figure 4-30. Section B layers and boundary conditions.

4.3.3.2 Transient and Steady State Seepage

Two transient simulations were run for Section B, considering different configurations of the burrow extending across the test trench and below the tree. The first scenario considers that the burrow is connected to the trench (Figure 4-33a) and a second scenario uses a small soil plug between the trench and the burrow to delay the progression of the saturation front towards the landside (Figure 4-33b).

Similar to the previous results, the presence, continuity and length of the ~~animal~~ burrow greatly influence the development of the saturation front. After 24 hours of simulation, the model with a plugged burrow shows the wetting front extending about 4 ft away from the centerline trench, whereas the model with the open burrow shows positive pore pressures along most of the waterside half of the embankment.

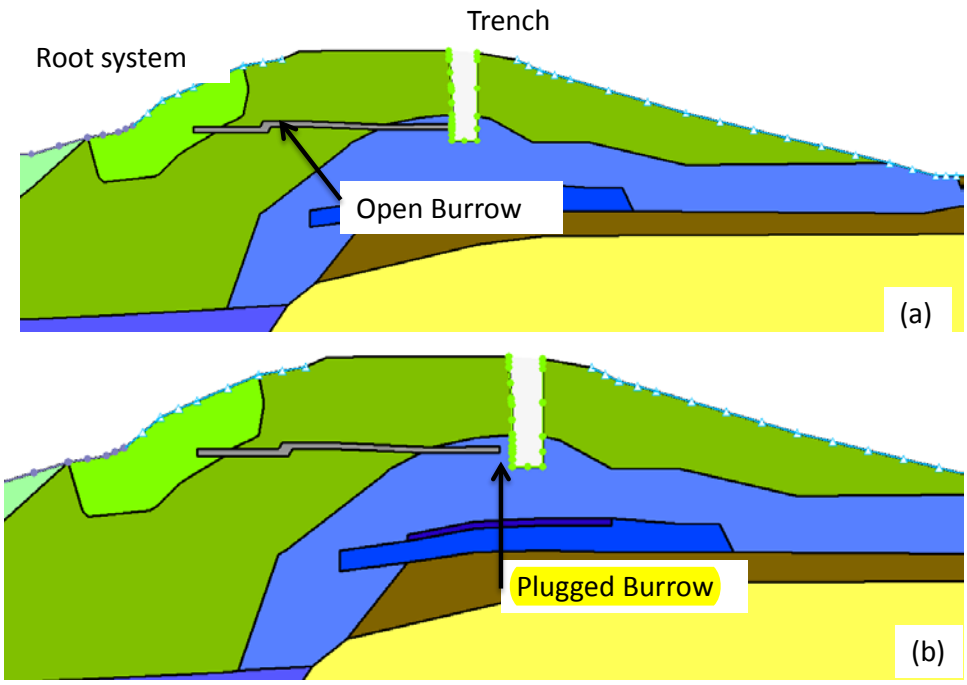

Figure 4-31. Section B transient analysis scenarios.

Results of the transient simulations are shown on Figure 4-34 through Figure 4-41. The computed heads on the waterside slope are the same for both simulations, creating a wetting front extending radially out from the open burrow, but the effect of the plugged burrow limits the development of a saturation front for most of the simulated time.

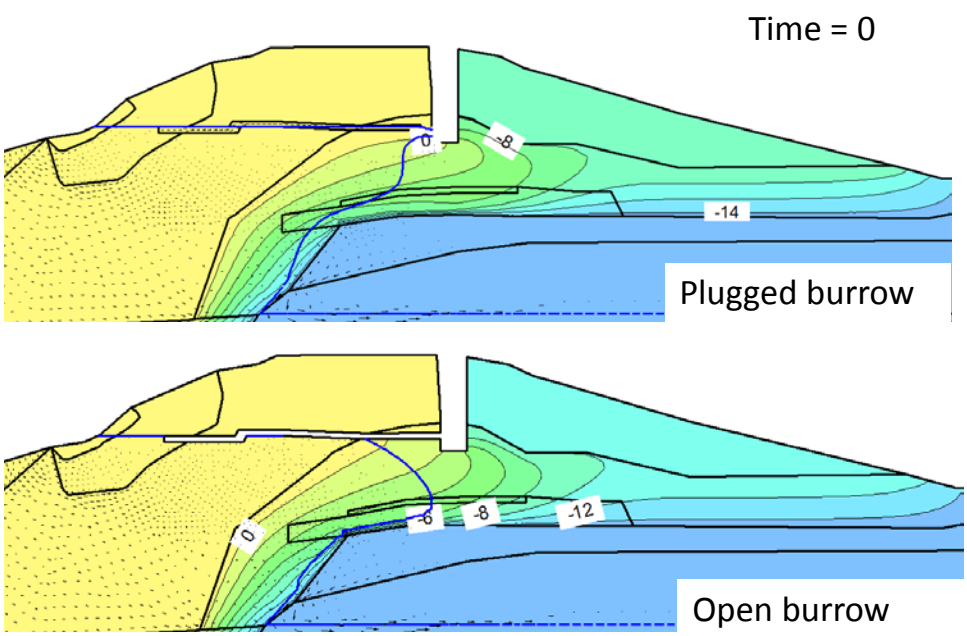

Figure 4-32. Section B transient analysis results, comparison between open and plugged burrows. Simulation time 0 hours. Total head contours at 2 ft intervals shown

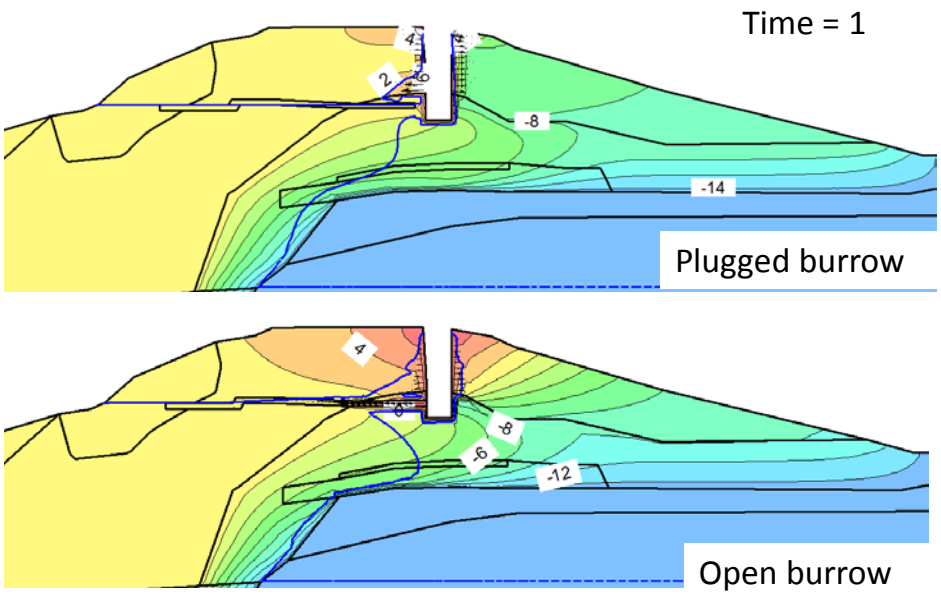

Figure 4-33. Section B transient analysis results, comparison between open and plugged burrows. Simulation time 1 hour. Total head contours at 2 ft intervals shown

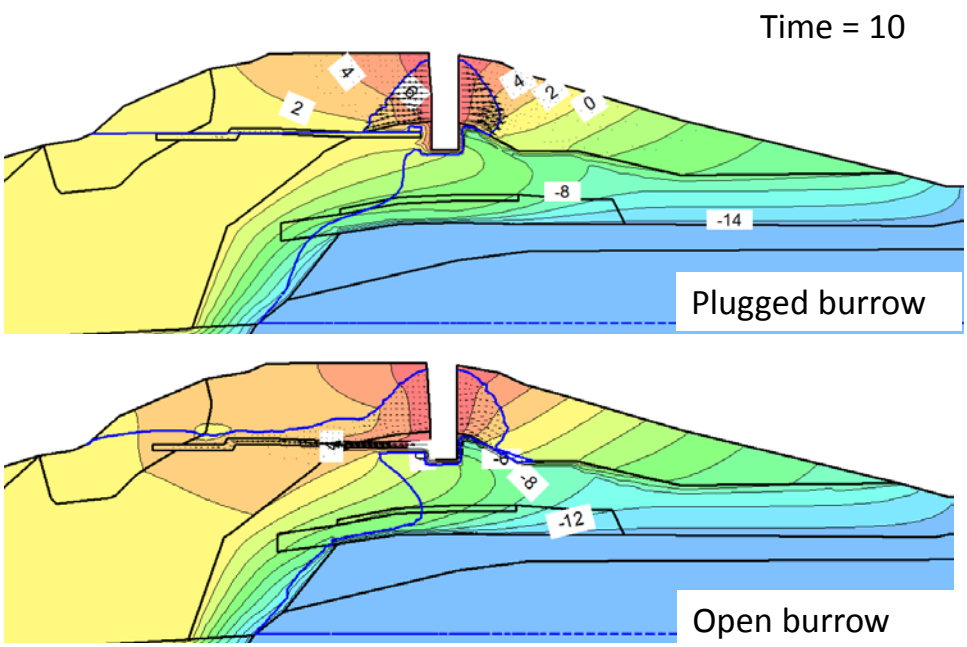

Figure 4-34. Section B transient analysis results, comparison between open and plugged burrows. Simulation time 10 hours. Total head contours at 2 ft intervals shown

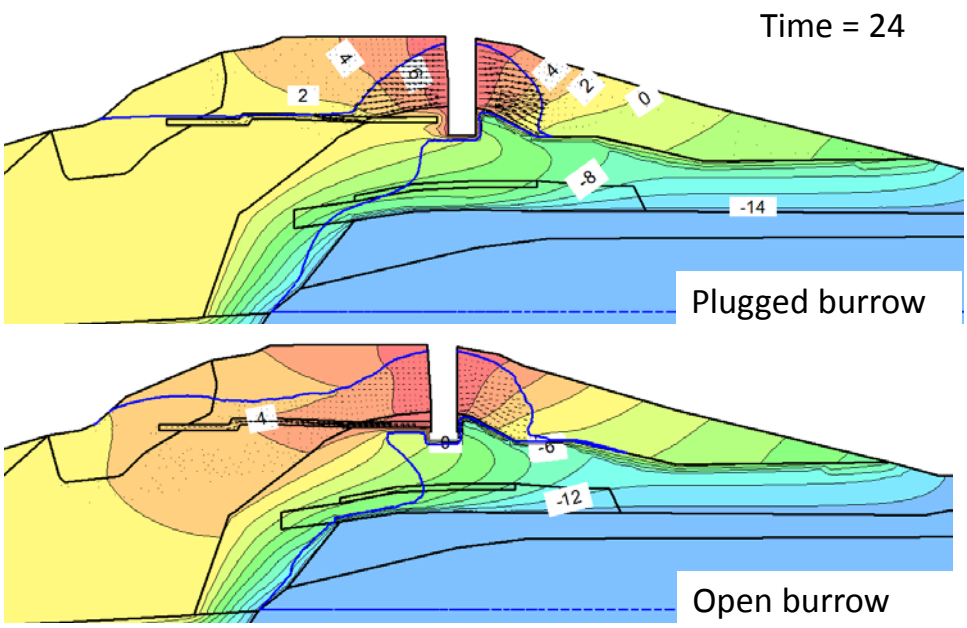

Figure 4-35. Section B transient analysis results, comparison between open and plugged burrows. Simulation time 24 hours. Total head contours at 2 ft intervals shown

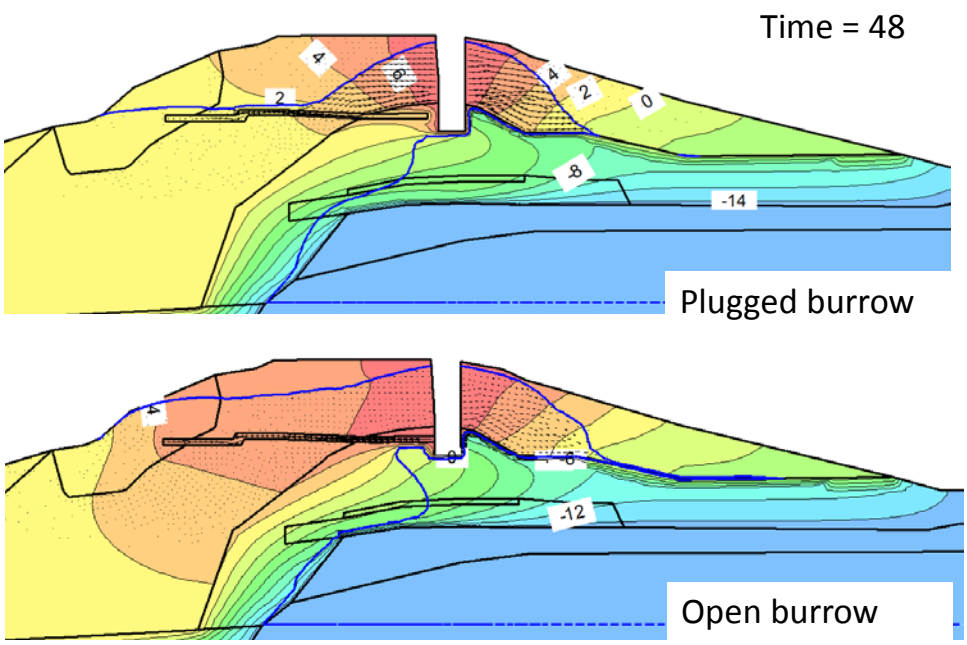

Figure 4-36. Section B transient analysis results, comparison between open and plugged burrows. Simulation time 48 hours. Total head contours at 2 ft intervals shown

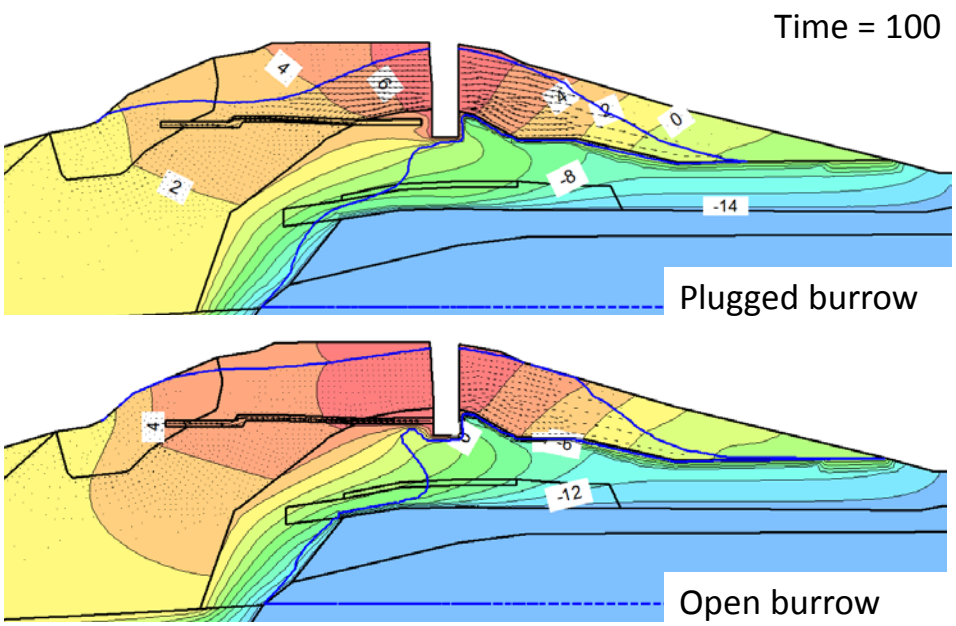

Figure 4-37. Section B transient analysis results, comparison between open and plugged burrows. Simulation time 100 hours. Total head contours at 2 ft intervals shown

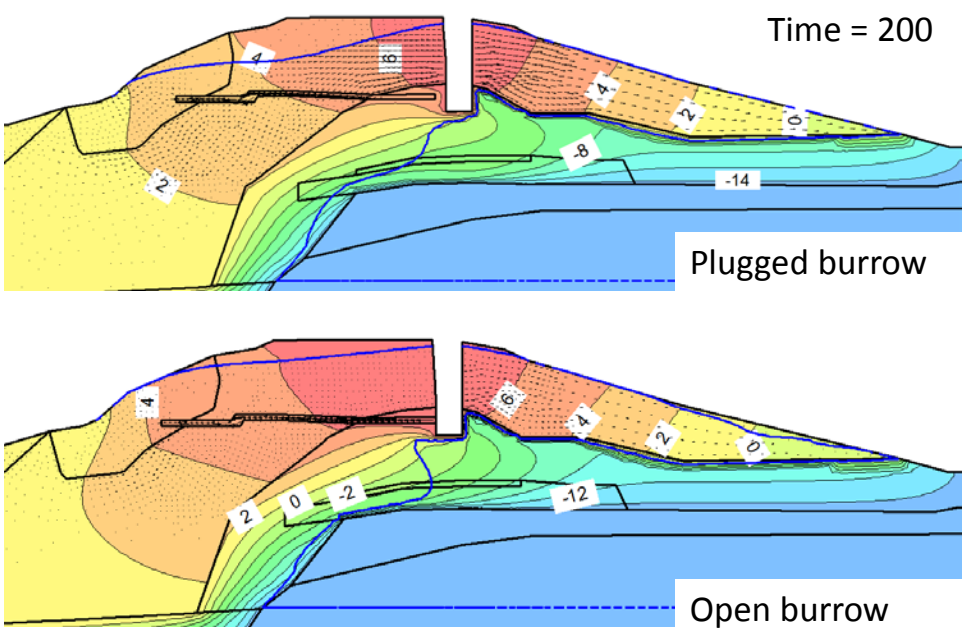

Figure 4-38. Section B transient analysis results, comparison between open and plugged burrows. Simulation time 200 hours. Total head contours at 2 ft intervals shown

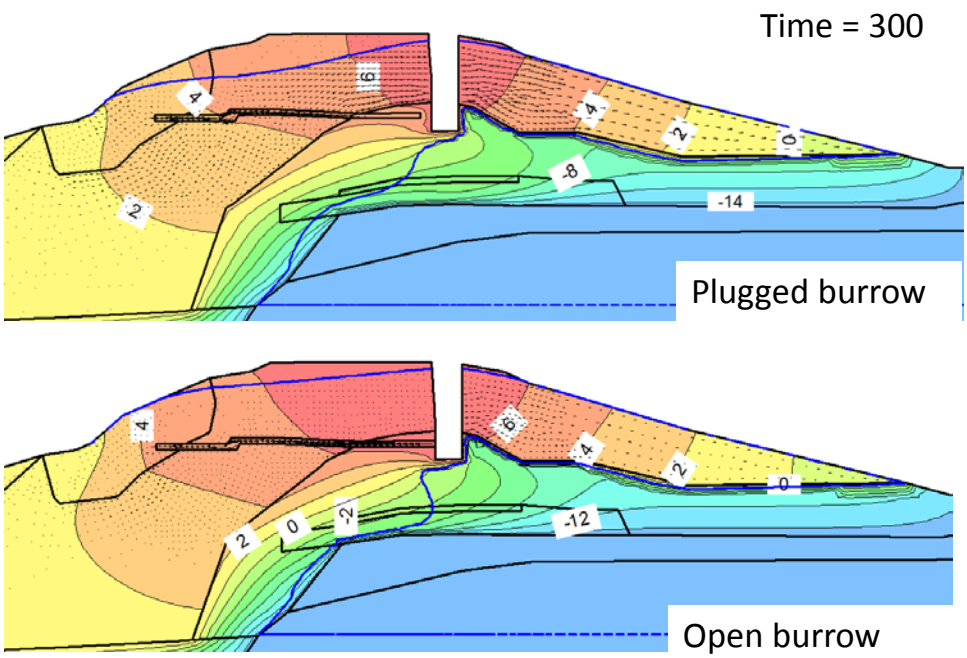

Figure 4-39. Section B transient analysis results, comparison between open and plugged burrows. Simulation time 300 hours. Total head contours at 2 ft intervals shown

Additional steady state analyses were performed for the following scenarios:

- Waterside inundation at El. +7 ft (Figure 4-42), with no ~~animal~~ burrow and varying the length of the burrow.
- Landside inundation at El. +7 ft (Figure 4-43), with no animal burrow and varying the length of the burrow.
- Test inundation at El. + 7.5 ft (Figure 4-44), with no animal burrow and varying the length of the burrow.

The models were constructed varying the length of open mammal burrows for input into slope stability models (Figure 4-33)

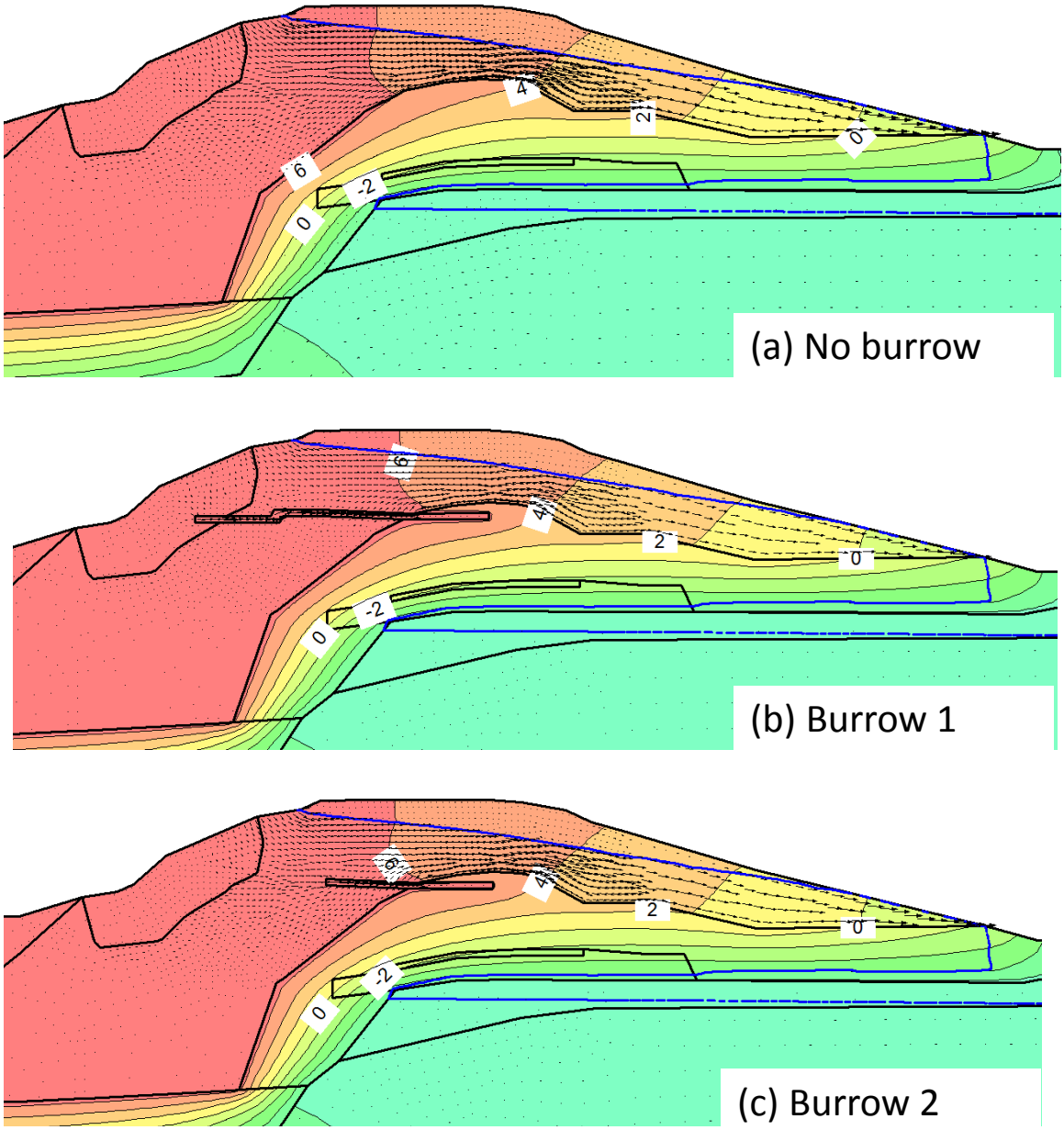

Figure 4-40. Section B waterside inundation steady state models.

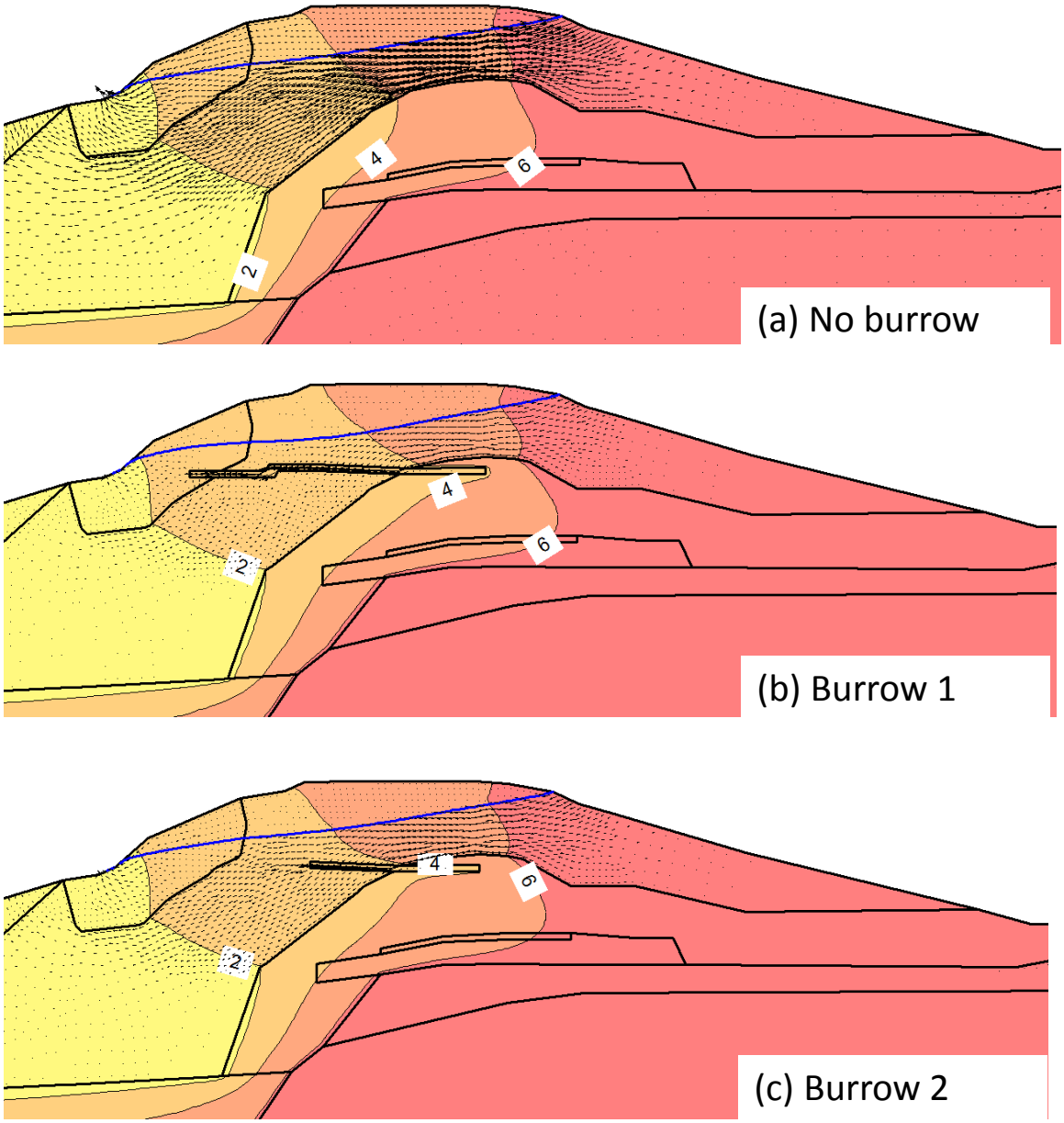

Figure 4-41. Section B landside inundation steady state models.

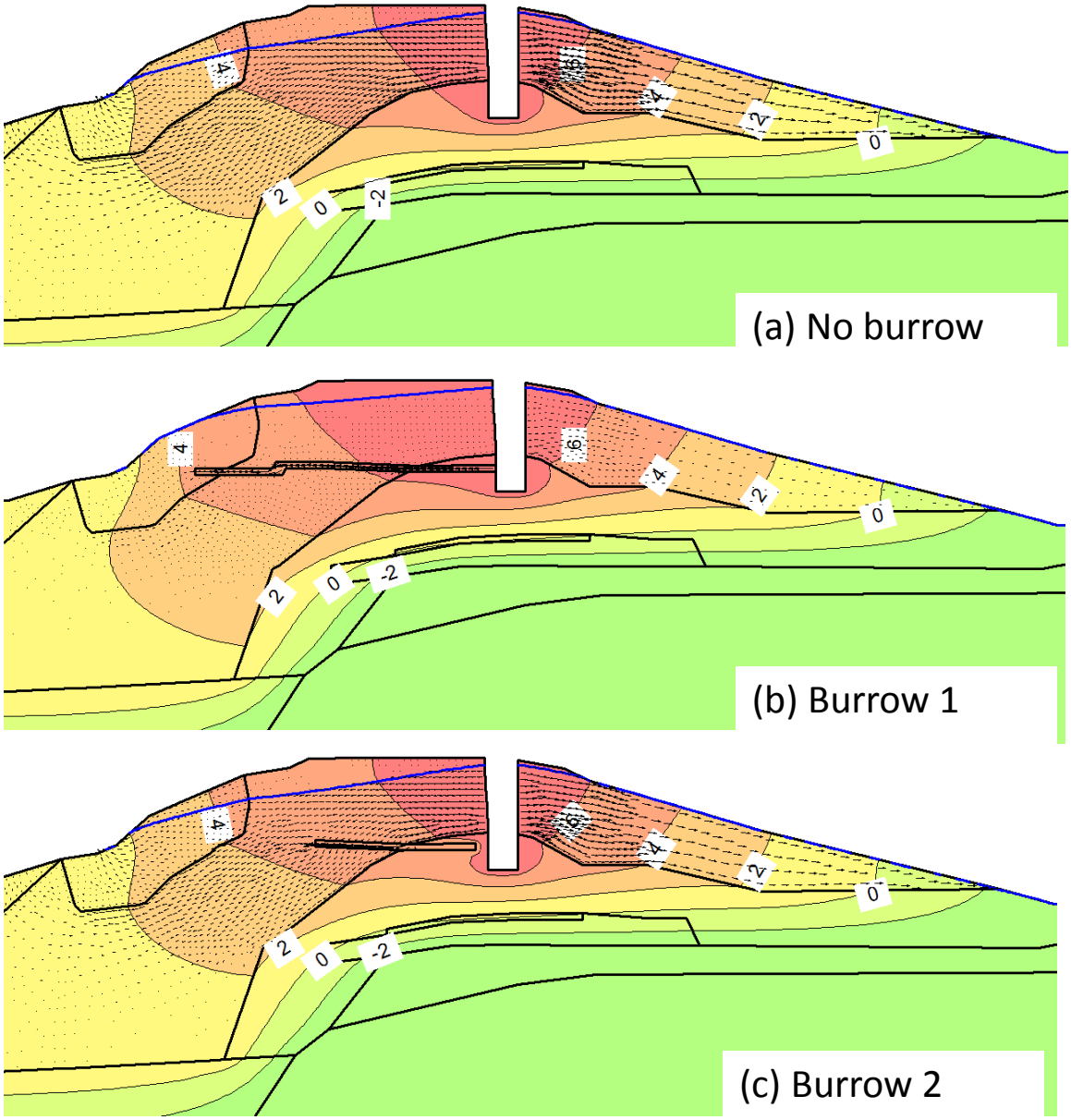

Figure 4-42. Section B centerline trench inundation steady state models.

4.3.4 Seepage Analyses at Section C

4.3.4.1 Initial and Boundary Conditions

Initial conditions for Section C consider a slough water elevation of +1 ft, and a far-field phreatic level at -15 ft. Boundary conditions for the transient simulation are the 7.5 ft inside the trench and the same slough and far-field conditions (Figure 4-45). Though present, localized burrows were located north of the instrument line. As discussed earlier, burrows that warranted their inclusion in the simulations and roots were scarce in the vicinity of Section C.

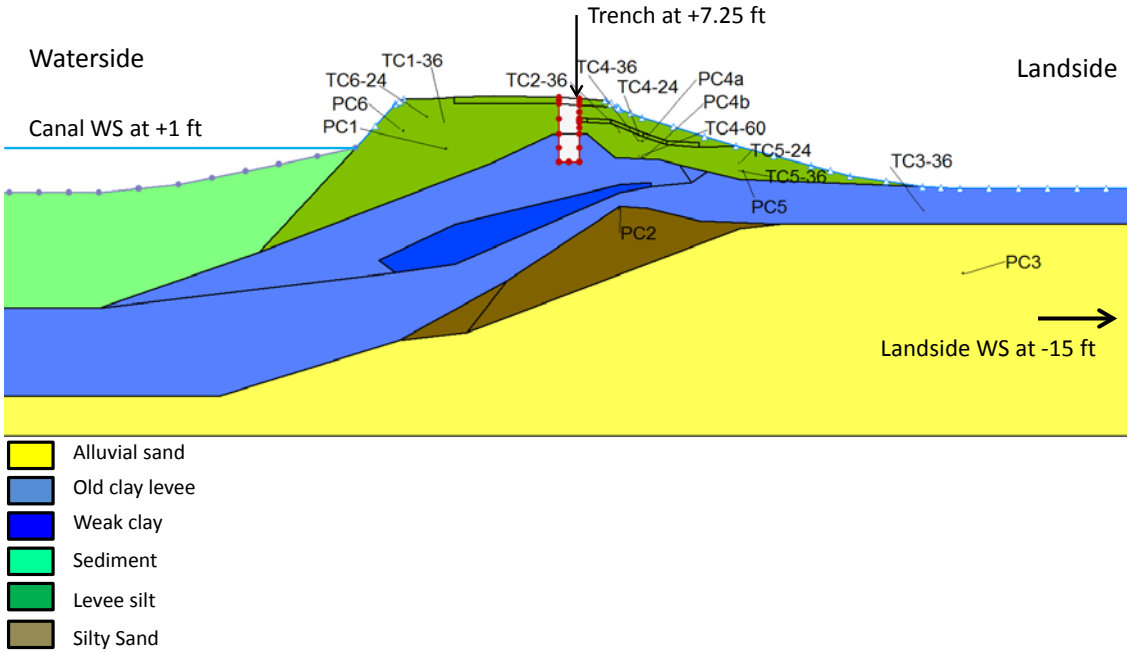

Figure 4-43. Section C layers and boundary conditions.

4.3.4.2 Transient and Steady State Seepage

The transient simulation for Section C corresponds to the section employed in the parameter calibration described in Section 4.3.1. Results of the transient simulations are shown on Figure 4-46 through Figure 4-53.

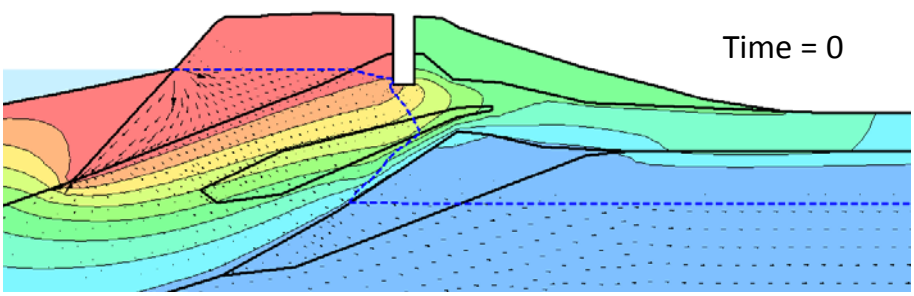

Figure 4-44. Section C transient analysis results. Simulation time 0 hours. Total head contours at 2 ft intervals shown

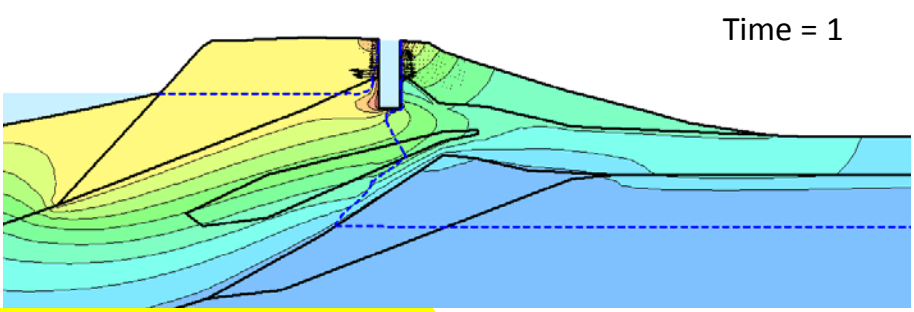

Figure 4-45. Section C transient analysis results. Simulation time 1 hour. Total head contours at 2 ft intervals shown

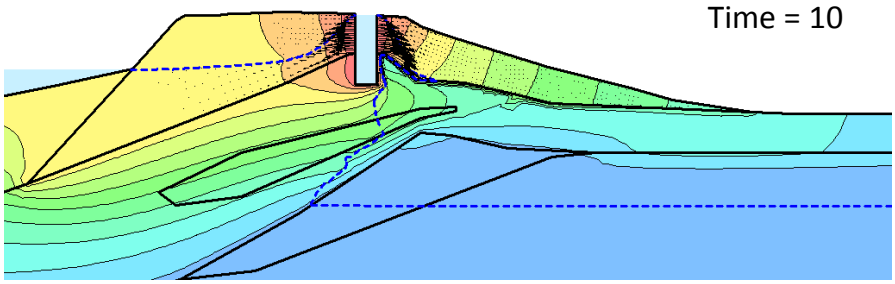

Figure 4-46. Section C transient analysis results. Simulation time 10 hours. Total head contours at 2 ft intervals shown

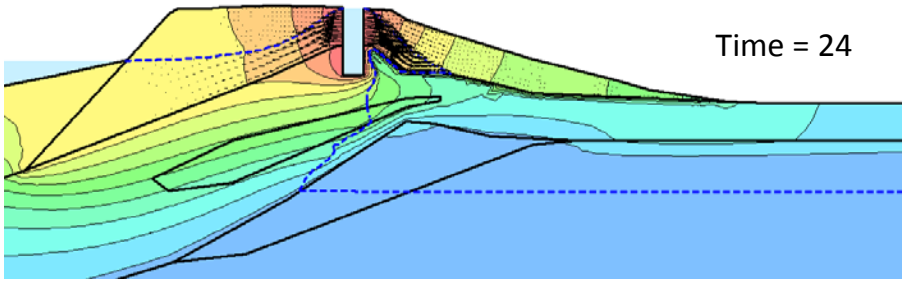

Figure 4-47. Section C transient analysis results. Simulation time 24 hours. Total head contours at 2 ft intervals shown

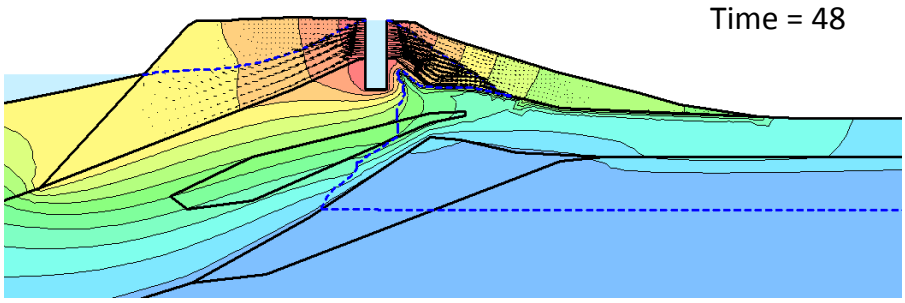

Figure 4-48. Section C transient analysis results. Simulation time 48 hours. Total head contours at 2 ft intervals shown

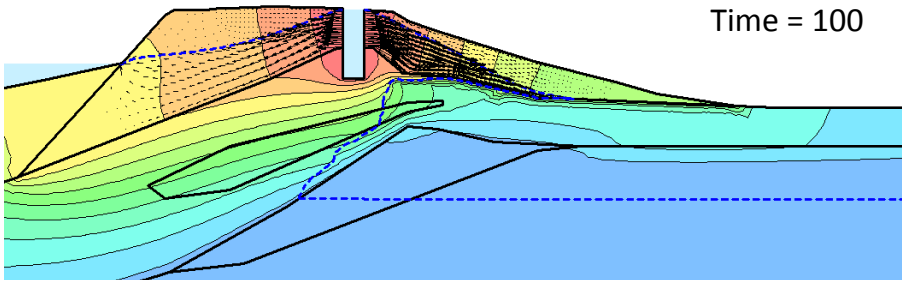

Figure 4-49. Section C transient analysis results. Simulation time 100 hours. Total head contours at 2 ft intervals shown

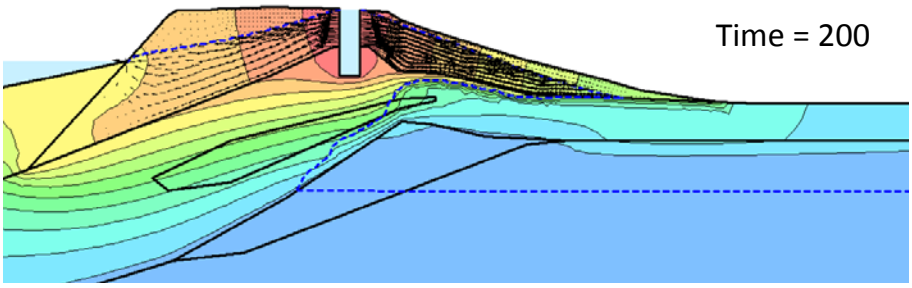

Figure 4-50. Section C transient analysis results. Simulation time 200 hours. Total head contours at 2 ft intervals shown

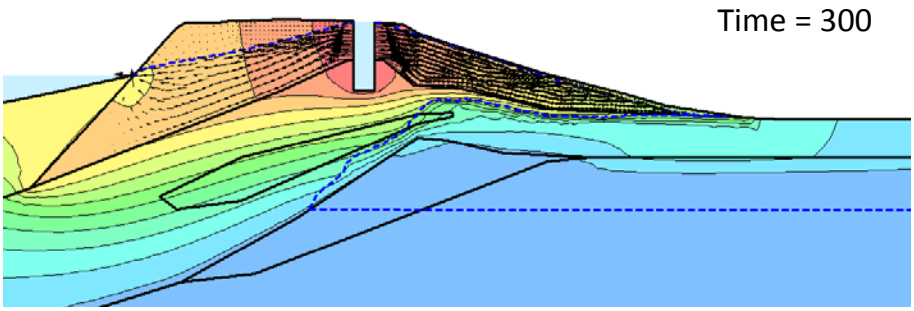

Figure 4-51. Section C transient analysis results. Simulation time 300 hours. Total head contours at 2 ft intervals shown

Additional steady state analyses were performed for the following scenarios:

- Waterside inundation at El. +7 ft (Figure 4-54), with no ~~animal~~ burrow and varying the length of the burrow.
- Landside inundation at El. +7 ft (Figure 4-55), with no animal burrow and varying the length of the burrow.
- Test inundation at El. + 7.5 ft (Figure 4-56), with no animal burrow and varying the length of the burrow.

The models were constructed varying the length of open mammal burrows for input into slope stability models (Figure 4-45)

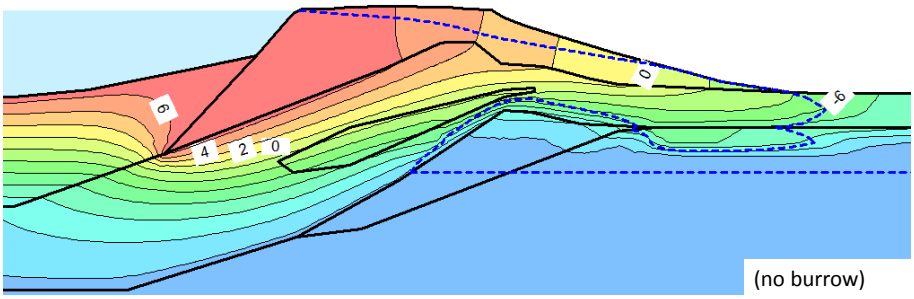

Figure 4-52. Section C waterside inundation steady state model.

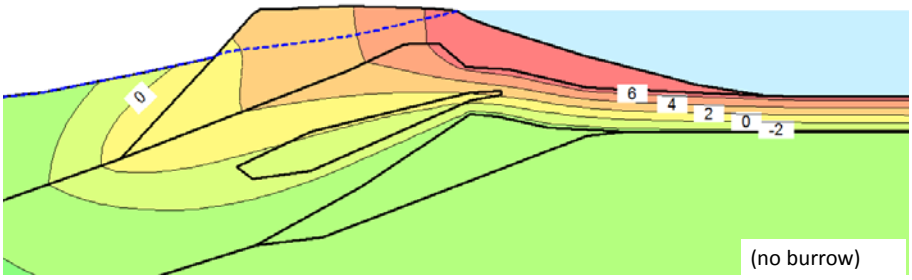

Figure 4-53. Section C landside inundation steady state model.

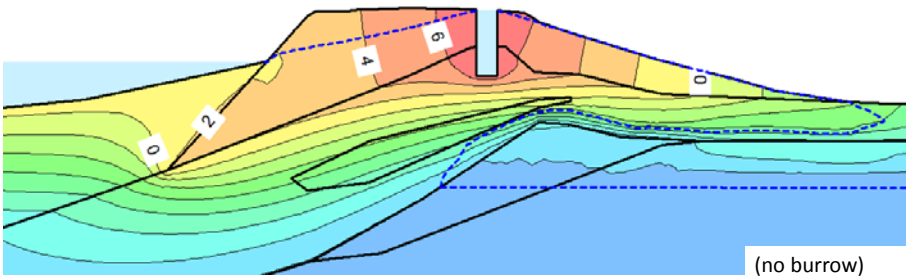

Figure 4-54. Section C centerline trench inundation steady state model.

4.4 SLOPE STABILITY MODELING

4.4.1 Modeling Root Reinforcement and Tree Loading

Roots within the root plate were modeled as a rigid body, similar to a footing foundation. Roots extending away from the root plate were modeled as reinforcing elements with zero shear strength in the Slope/W software. Total horizontal and vertical root loading for the landside and waterside oak trees are provided in Table 4-2 and Table 4-3, respectively.

Estimates for number and size of roots at closer distances to the tree were achieved based on available root architecture data as discussed in Shriro (2014) and Volume 3 of this series (Shriro et al., 2014b). Roots located between the tree and the trench were not captured in trench logs. Based on a review of raw data charts for several valley oak trees excavated, which were provided by Dr. Alison Berry and Shih-Ming Chung of UC Davis, roots were estimated to be about 5 times more abundant at distances of 25 to 50 percent of the canopy radius. Roots were about 2.5 times larger at 25 percent of the canopy radius than ~~the size~~ at 50 to 100 percent of the canopy radius. For roots that ~~are~~ too short to have ~~been~~ intersected ~~by~~ trench logs, the total load capacity of these roots ~~could be~~ estimated from the size and number of roots encountered at the trench. ~~The~~ roots extending from both the waterside and landside oak ~~trees~~ ~~intersected~~ during trenching extend to approximately 65 to 100 percent of the canopy diameter. Using these relationships, root load distributions were estimated for the landside and waterside trees as shown on Table 4-2 and Table 4-3, respectively. These assumptions were used in estimating values of

horizontal forces shown in Figure 4-57 and Figure 4-58 for the landside and waterside trees, respectively.

The horizontal component of force is divided over the 'slice width' to arrive at a unit horizontal force and is then further divided to create 5 forces, evenly distributed over the root zone within Slope/W model sections (Figure 4-57 and Figure 4-58). These forces represent the horizontal load on the embankment associated with the lean of the tree and a downhill wind force. Root reinforcement is modeled as a horizontal force acting into the slope, resisting movement. The bonded length of the reinforcement is equal to the length of the reinforcing element outside of the slide zone. Horizontal point loads are only active in the calculation of the factor of safety when included inside the slide circle. Combining the use of reinforcing elements with the use of horizontal forces allows for the inclusion of loading associated with wind and tree lean within the slide mass. In general, loads are higher near the tree (F1 and F2) and lower with distance.

The reaction force of the root plate on the levee slope was distributed over the root plate and entered as a unit weight for the root plate within the model. These loads were only applied through the cross section passing through the tree. This cross section is used to represent a 'slice width' equal to the square root of the root plate area.

Table 4-2. Horizontal and vertical root forces for landside oak tree.

	Total Loads (lbs)	Unit Load (per 1 ft slice) (lbs)
T_H (horizontal roots)	**9,170**	**1,200**
T_{H25} (inner 25% of canopy radius)	4,130	520
T_{H50} (25-50% of canopy radius)	3,210	400
T_{H75} (outer 75-100% canopy radius)	1,830	230
T_V (vertical roots)	**10,200**	**1,300**

Table 4-3. Horizontal and vertical root forces waterside oak tree.

	Total Loads (lbs)	Unit Load (per 1 ft slice) (lbs)
T_H (horizontal roots)	**74,500**	**9,300**
T_{H25} (inner 25% of canopy radius)	33,500	4,200
T_{H50} (25-50% of canopy radius)	26,100	3,300
T_{H75} (outer 75-100% canopy radius)	14,900	1,900
T_V (vertical roots)	**97,000**	**12,100**

A number of large roots originating from the waterside oak tree were cut during trenching. The impact of these roots on tree stability was considered using tables of root load capacity with effective stress provided for various root lengths in Appendix A. For the roots modeled in the root plate zone of the waterside oak tree (8-foot slice width), the additional capacity of the two roots is 1,330 lbs each if 10 additional feet were added to these roots.

This load applied over the root plate width yields a total load of 10,600 lbs of capacity, discounted to 6,400 lbs due to pore water pressure rise. Roots that were cut account for approximately 9 percent of the total horizontal demand of 73,000 pounds estimated in Table 4-3. A reduction of 9 percent in the capacity of the root system added to the 40 percent loss due to strength loss in response to pore water pressure accumulation leads to a reduction of 50 percent in the original estimate of 960 kip-ft of moment capacity. With moment demand on the order of 480 kip-ft (as previously discussed), and 960 kip-ft reduced to 490 kip-ft, the factor of safety against overturning is very close to unity (factor of safety of 1.02).

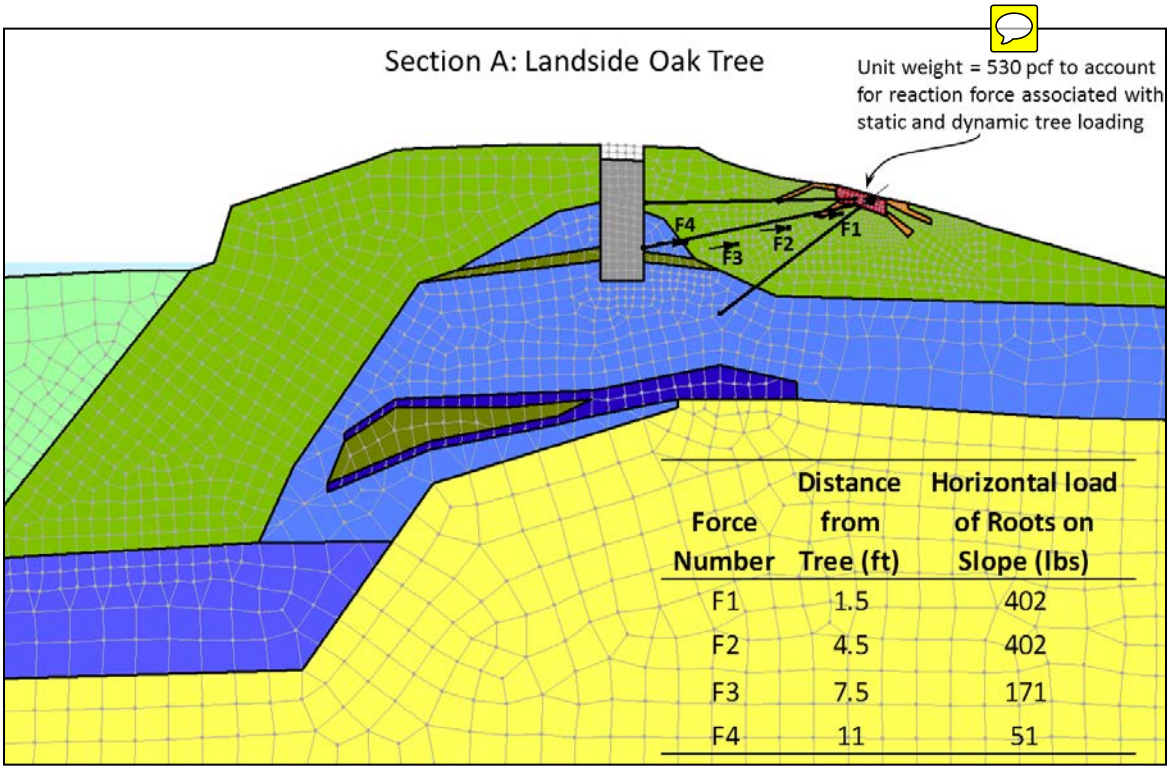

Force Number	Distance from Tree (ft)	Horizontal load of Roots on Slope (lbs)
F1	1.5	402
F2	4.5	402
F3	7.5	171
F4	11	51

Figure 4-55. Example of root reinforcing and distributed horizontal forces at the landside oak.

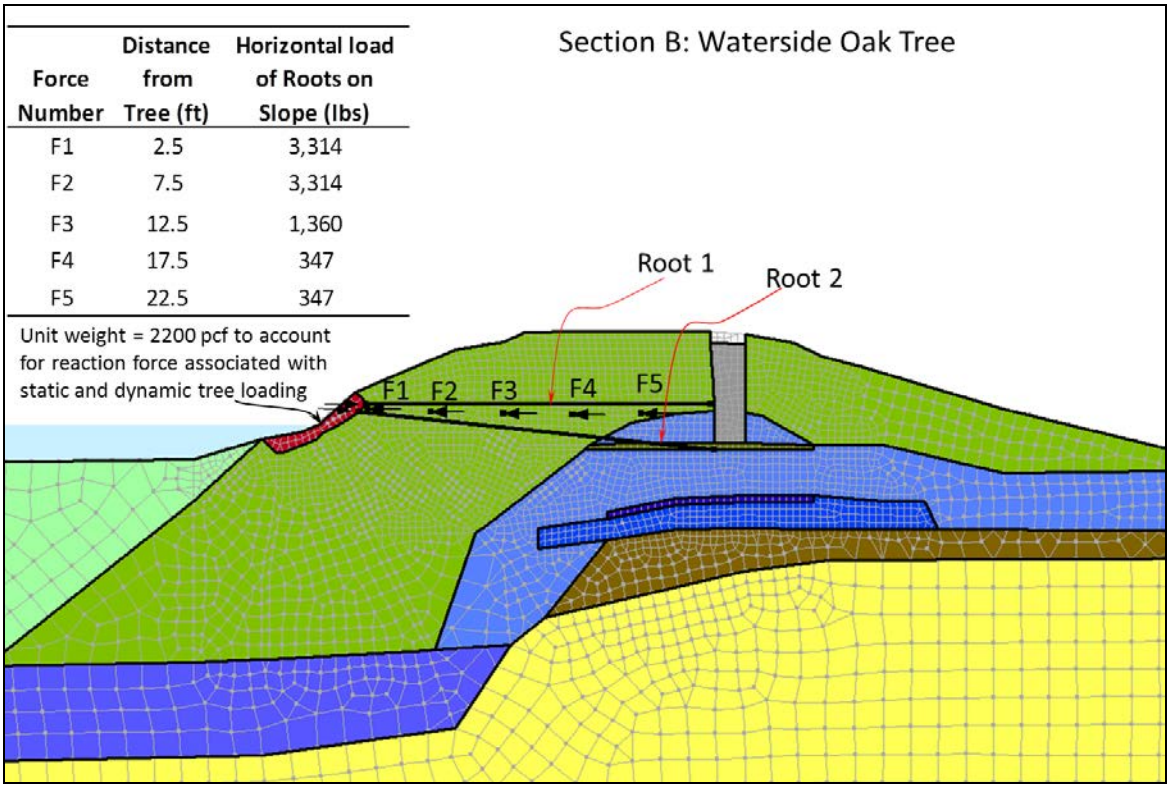

Figure 4-56. Example of root reinforcing and distributed horizontal forces at the waterside oak.

4.4.2 Shear Strength Assumptions

Coarse-grained soils were considered to be free-draining and were modeled using drained shear strength parameters. Non-free draining materials were modeled under long-term steady state conditions using drained shear strength values correlated from moisture content and index properties, standard penetration test data (SPT), and cone penetration test data (CPT).

Mayne (2007) was implemented to estimate drained friction angle for onsite soils based on normalized cone tip resistance as follows:

$$\phi' = 17.6 + 11Log(q_{t1})$$

Where $q_{t1} = normalized\ tip\ resistance = \frac{(q_t/\sigma_{atm})}{(\frac{\sigma'_{vo}}{\sigma_{atm}})^{0.5}}$

For silts and clays, values of drained friction angle calculated by correlation with CPT normalized tip resistance were compared with those derived using Mitchell (1976) for silts and clays with a plasticity index (PI) larger than 7:

$$\phi' = \sin^{-1}(0.8 - 0.94\ln(PI))$$

SPT blow count values were measured during drilling and were corrected for hammer efficiency, rod length, borehole diameter, overburden stress (Youd et al. 2001). Values of

corrected blow count -$(N_1)_{60}$ – were input into a correlation by Hatanaka & Uchida (1996) and summarized in FHWA (2002):

$$\phi' = (15.4(N_1)_{60})^{0.5} + 20°$$

Data were not available for waterside sediments. These sediments were given a low undrained strength with the assumption that strain compatibility may prevent full mobilization of shear strength for this material. Where site specific data was not available, typical values were used from Duncan and Wright (2005).

Strength values used in design are presented inTable 4-4. The shear strength of the levee fills controls the analysis, as most potential slide planes did not extend into the 'old levee soils'.

Table 4-4: Shear strengths used in modeling effort

	Unit Weight (pcf)	c' (psf)	φ' (degrees)
Levee Silt (ML)	120	0	32
Old Clay Levee	120	0	34
Sediment	100	150	0
Silty Sand	120	300	33
Alluvial Sand	125	0	37
Alluvial Silt	120	0	34
Fine-grained Alluvium	120	400	25
Soft Clay/Weak Clay	120	500	0
Gravel	135	0	38

A rapid loading condition was considered in the modeling of failure scenario BC3, a failure envelope extending to the trench that opened a little over 2 hours into the flow test. An undrained or partially drained strength envelope would need to be defined to model this condition. Supplemental exploration is recommended if a better understanding of this slide surface is sought. The program should be designed to explore the continuity of weak beds of silt and clay on the waterside as well as to collect undisturbed samples for high quality strength testing.

4.4.3 Pore Water Pressure Conditions

Transient and steady state seepage models were described in previous sections of this volume. Transient models generally captured the wetting front patterns observed during the flow test. In general, steady state in the transient model was defined as 15 days into the simulation. On the waterside, predictions matched well with 15 day 'steady state' simulation. On the landside slope, the transient model overestimated the measured steady state pore water pressures by approximately 25 percent. For landside models, steady state within the transient model simulation was defined as 2 days into the flow test to better match measured conditions.

4.4.4 Slope Stability Analyses Results

As discussed, a mass-averaged factor of safety was employed for each of the two landside and four waterside failure scenarios presented on Figure 4-2. A set of cross sections were placed within each mass to represent differing geometric and loading conditions. Each section represented a 'slice width'. Where trees existed within a mass, a section was drawn through the trunk representing a 'slice width' equal to the width of the root plate. Static and dynamic wind loading were applied in the area of the trunk and root system as discussed above. The width of the root plate was estimated as the square root of the pit area derived from windthrow data (Peterson, 2012). Cross sections adjacent to the root plate represented zones of root reinforcement without static and dynamic tree loading. Trench logs and root area ratios were used to estimate the size and placement of root reinforcement within each cross section. Each section was analyzed to calculate the factor of safety using the two-dimensional limit equilibrium slope stability modeling software Slope/W with pore water pressures generated within the Seep/W software.

4.4.4.1 Stability of Landside Failure Scenarios

Representative cross sections through failure scenarios Landside A and Landside C (Figure 4-2) are shown on Figure 4-59. Table 4-5 presents a summary by cross section of calculated factors of safety as well as the 'slice width' represented by each section, the mass of a 1-foot slice of the critical slide mass, and the mass-averaged factor of safety value of each failure scenario. Slope/W results for each section are presented in Appendix B.

Failure scenario Landside A was modeled under initial pore water pressure conditions (post trench construction but prior to inundation with water), and steady state flow test conditions as captured by instrumentation during the flow test. Overall, initial models found that transient seepage models over-predicted pore water pressures at steady state on the landside by about 25 percent, resulting in mass-averaged factors of safety very close to unity. Deformations or distress indicative of instability were not observed on the land side of the levee, indicating factor of safety values were likely higher than unity. These over-predictions in pore pressure were corrected by modeling with transient seepage models two days into the flow test to better match observed pore pressures.

Each pore water pressure condition was modeled with and without the loading and reinforcement of the tree. In general, the mass-averaged factor of safety was found to be similar with and without the tree for pore pressure conditions modeled. Factors of safety under initial conditions for the Landside A failure scenario are 2.52 and 2.46 with and without a tree, respectively. Similarly, under pore water pressure conditions representative of steady state conditions, factors of safety of 1.83 and 1.80 are calculated for the Landside A slide mass with and without a tree, respectively.

The factor of safety against instability under a steady state waterside flood condition (the levee is loaded with a water surface elevation 3 feet below the crest elevation) was compared with the steady state test condition. The Crown Trench Seepage Test generated higher pore water pressures within the levee than a simulated flood, resulting in a mass

averaged factor of safety value of 1.83, as compared with 1.99 during simulated flood conditions.

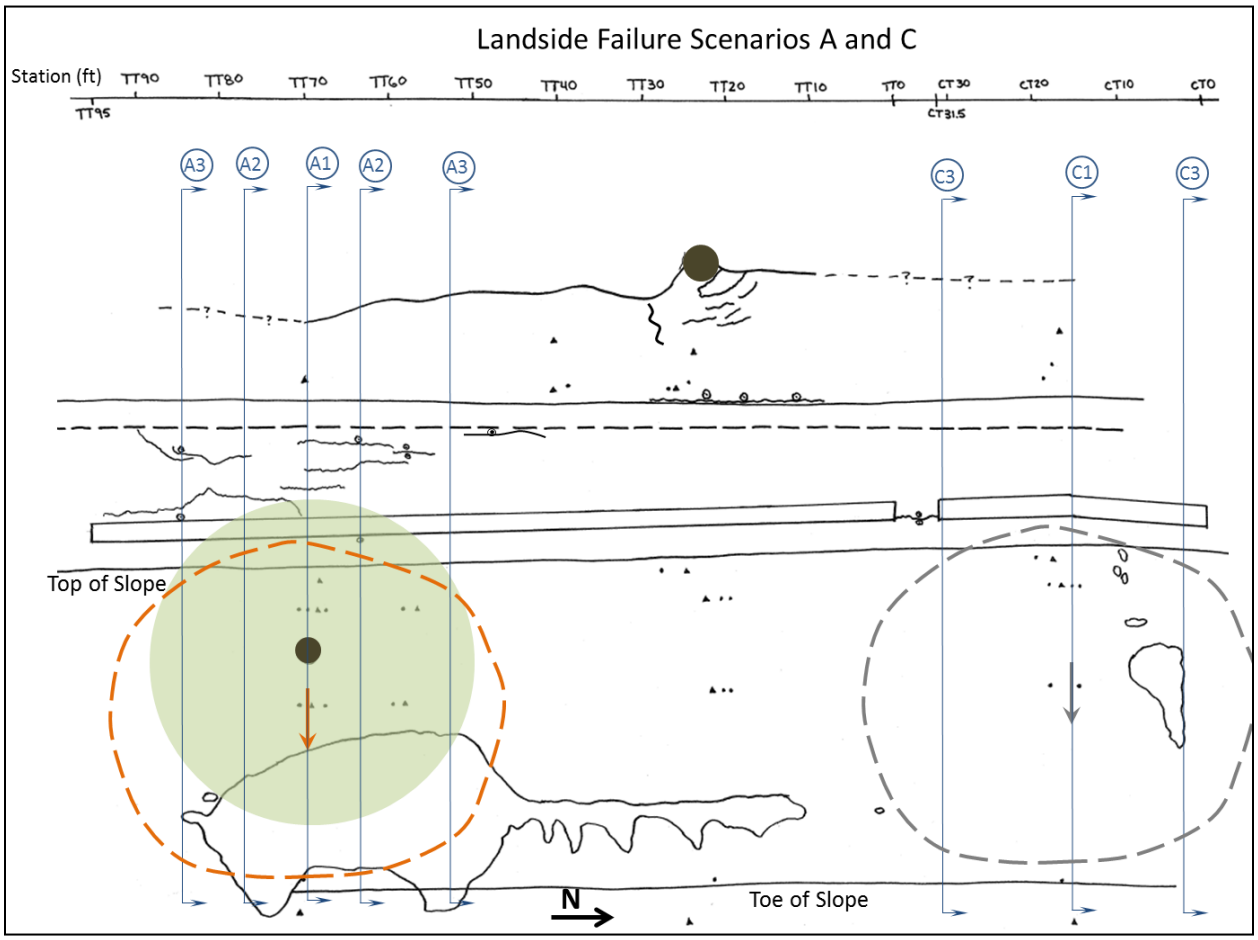

Figure 4-57. Landside failure scenarios modeled. Scenario A (orange) is in the vicinity of the landside oak tree while Scenario C (gray) is at the control section.

Table 4-5. Results of mass averaged factor of safety for landside failure scenarios

Model	Section	Pore Pressure Condition	Slice Width (ft)	Weight of Section (lbs)	Factor of Safety (FOS)	Total mass	Total mass x FOS	Mass averaged FOS
Landside A	A1	Initial pre-test without tree	7	6,397	2.50	44,780	111,949	2.46
	A2	Initial pre-test without tree	16	6,397	2.50	102,354	255,884	
	A3	Initial pre-test without tree	24	5,030	2.41	120,725	291,188	
	A1	Initial pre-test with tree	7	9,310	2.23	65,170	145,134	2.52
	A2	Initial pre-test with tree	16	11,484	2.73	183,744	501,254	
	A3	Initial pre-test with tree	24	3,830	2.30	91,920	211,232	
	A1 (2D)	Steady state test without tree	7	7,824	1.81	54,767	99,128	1.80
	A2	Steady state test without tree	16	7,824	1.81	125,181	226,577	
	A3	Steady state test without tree	24	5,563	1.79	133,512	238,986	
	A1	Steady state test with tree	7	8,502	1.56	59,514	92,842	1.83
	A2	Steady state test with tree	16	6,278	1.99	100,450	199,895	
	A3	Steady state test with tree	24	4,804	1.82	115,296	209,839	
	A1	Steady state - waterside flood	7	14,014	1.89	98,098	185,798	1.99
	A2	Steady state - waterside flood	16	10,893	2.14	174,288	373,673	
	A3	Steady state - waterside flood	24	8,230	1.91	197,518	377,851	
Landside C	C1 (2D)	Steady state test	23	4,548	1.94	104,597	202,918	1.98
	C3	Steady state test	24	4,214	2.03	101,136	205,306	

4.4.4.2 Waterside Stability

The four waterside failure scenarios presented on Figure 4-2 are modeled under various pore water pressure conditions. Mass-averaged factors of safety against slope instability are presented on Table 4-6.

Waterside failures began with the observation of cracking at just over 2 hours into the flow test, with a crack forming between the control and tree trenches. The failure scenario explored at this location is Waterside BC3 as shown on Figure 4-2. The locations of representative cross sections within the Waterside BC3 failure scenario are presented on Figure 4-60. The scenario was modeled under transient pore water pressure conditions at 2 hours (when cracking first observed) and at 39 hours (the approximate time when the waterside oak fell), resulting in calculated average factors of safety of 1.88 and 1.72, respectively. Without tree loading and root reinforcing, the same slide mass yields a factor of safety of 1.67 at 39 hours into the flow test.

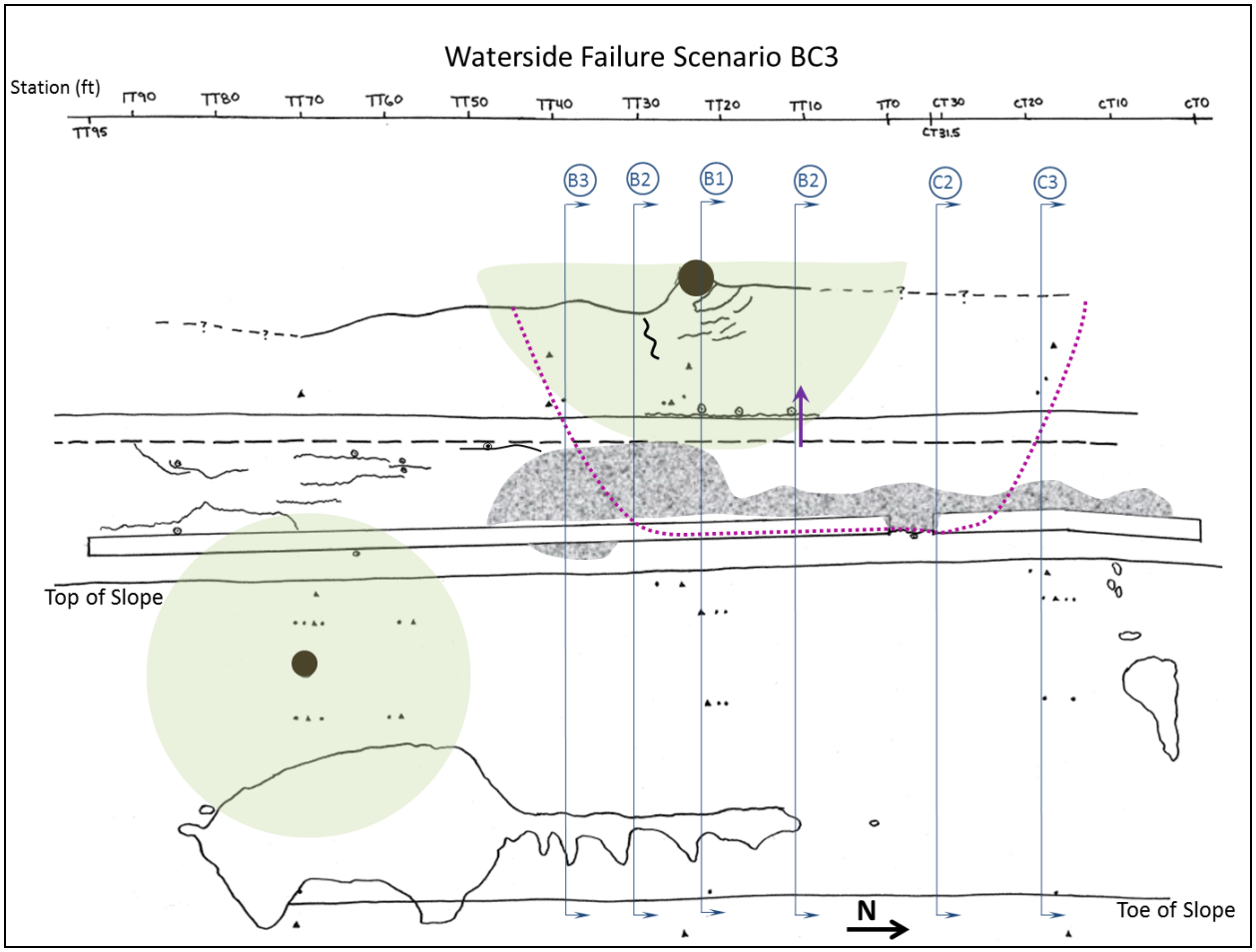

Figure 4-58. Failure scenario Waterside BC3

The levee crown road began to show pavement cracks after about 24 hours of flow in the vicinity of Section A. Stability at this location was explored through modeling of failure scenario Waterside A (Figure 4-2) under initial and steady state conditions before and during the flow test as well as under a landside flood condition (water surface elevation 3 feet below the levee crown) with average factor of safety values of 1.88, 1.48, and 1.45, respectively.

Figure 4-61 provides locations of representative cross sections modeled, results are summarized on Table 4-7, and Slope/W models are presented in Appendix B. Steady state test conditions produced a similar rise in pore water pressure to simulated steady state landside flood conditions (a viable flood scenario for Twitchell Island), and therefore saw similar factor of safety values.

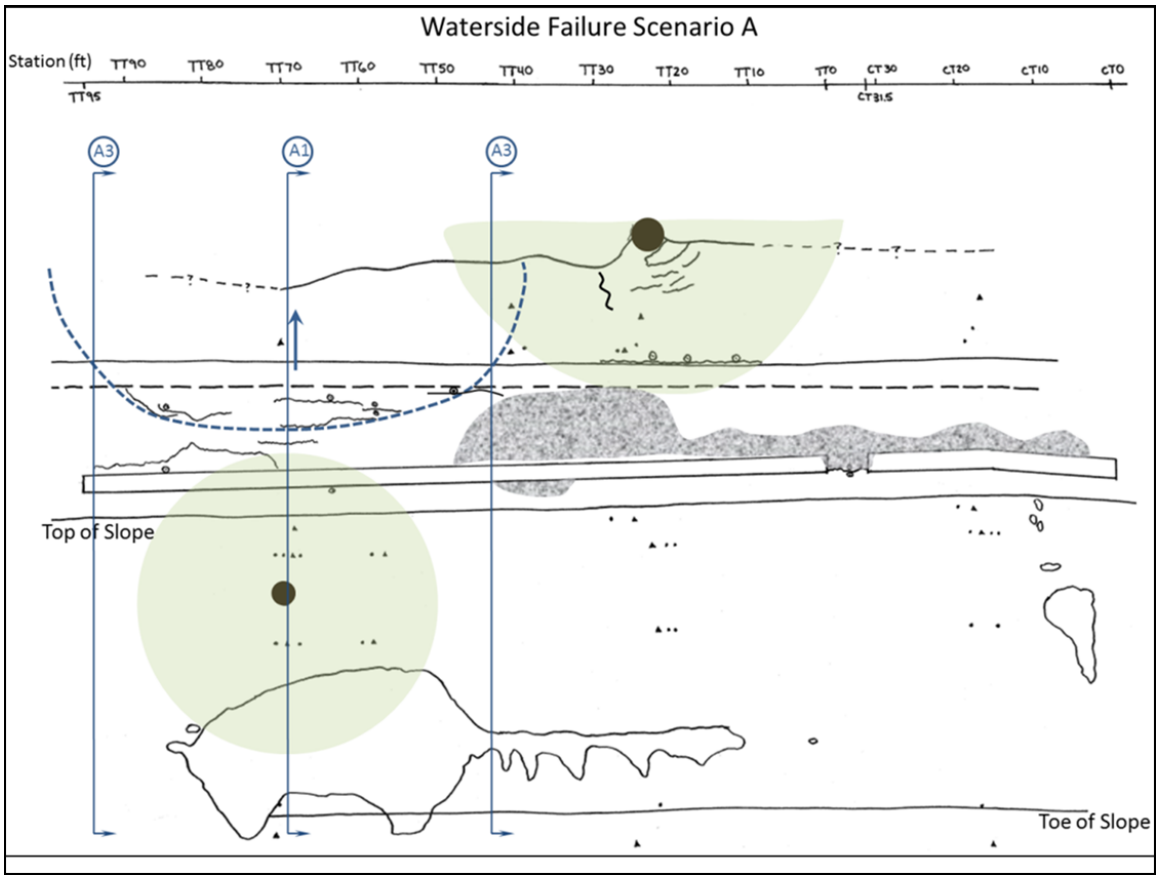

Figure 4-59. Failure scenario Landside A.

At 39 hours into the flow test, the waterside oak tree fell. Cracking was observed in the area immediately around the fallen tree. About 8 hours later, a crack along the top of the waterside slope was discovered, previously concealed by leaf litter and erosion protection. The time that the crack originated was not known. Two failure scenarios are shown on Figure 4-62 and Figure 4-63 named Waterside B-1 (limited to local area around oak tree) and Waterside B-2 (extending up to the top of slope). The Waterside B-1 failure scenario, modeled with transient seepage conditions at 39 hours into the flow test, has a factor of safety against instability of 1.04. The B-2 failure scenario, also modeled under transient seepage conditions at a time of 39 hours, has factor of safety across the slide mass of 1.16 and 1.03 with and without the waterside oak tree, respectively. All waterside results are summarized in Table 4-6 with Slope/W results presented in Appendix B.

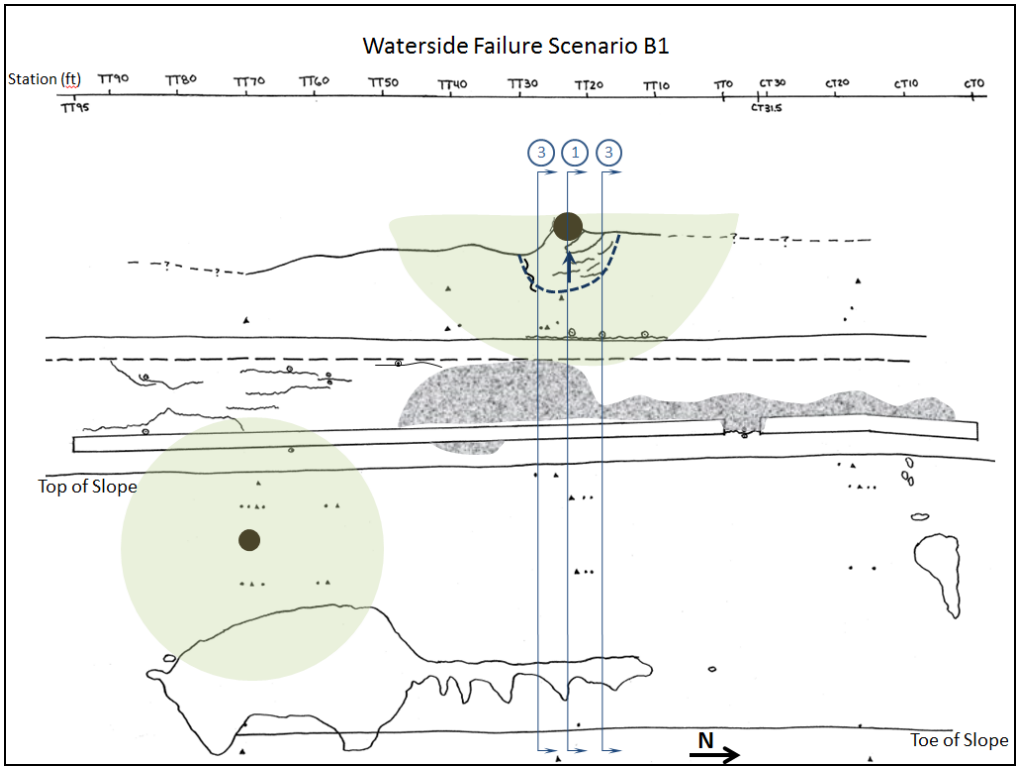

Figure 4-60. Waterside failure scenario B1.

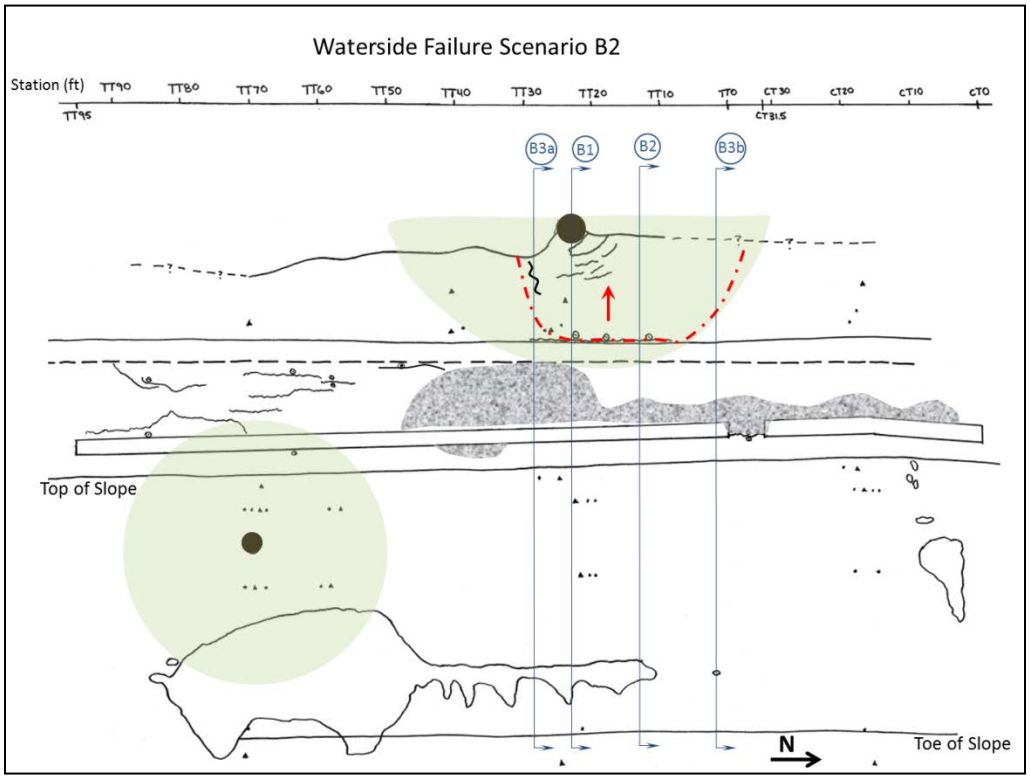

Figure 4-61. Waterside failure scenario B2.

Table 4-6: Results of mass averaged factor of safety against instability for waterside failure scenarios

Model	Section	Pore Pressure Condition	Slice Width (ft)	Weight of Section (lbs)	Factor of Safety (FOS)	Total mass	Total mass x FOS	Mass averaged FOS
Waterside A	A1	Initial pre-test	35	14,804	1.80	518,140	932,652	1.76
	A3	Initial pre-test	30	4,132	1.60	123,966	198,346	
	A1	Steady state test	35	13,456	1.50	470,960	706,440	1.48
	A3	Steady state test	30	4,072	1.40	122,148	171,007	
	A1	Steady state - landside flood	35	16,014	1.48	560,490	829,525	1.45
	A3	Steady state - landside flood	30	5,219	1.36	156,579	212,947	
Waterside B-1	B1	39 Hr transient - test	8	26,522	0.96	212,176	203,689	1.04
	B3	39 Hr transient - test	8	4,490	1.50	35,922	53,884	
Waterside B-2	B1	39 Hr transient - test	8	31,650	1.05	253,200	265,860	1.16
	B2	39 Hr transient - test	13	6,291	1.28	81,783	104,682	
	B3a	39 Hr transient - test	6	3,802	1.35	22,811	30,795	
	B3b	39 Hr transient - test	9	5,579	1.44	50,210	72,303	
	B1 - No Tree (2D)	39 Hr transient - test	8	6,641	1.07	53,130	56,849	1.03
	B2 - No Tree	39 Hr transient - test	12	6,641	1.07	79,694	85,273	
	B3a - No Tree	39 Hr transient - test	8	3,561	0.96	28,489	27,349	
	B3b - No Tree	39 Hr transient - test	12	3,561	0.96	42,733	41,024	
Waterside BC-3	B1	2 Hr Transient - Test	8	44,346	1.36	314,312	691,486	1.88
	B2	2 Hr Transient - Test	23	26,984	2.24	159,997	262,395	
	B3	2 Hr Transient - Test	10	10,784	2.03	443,460	603,106	
	C2	2 Hr Transient - Test	16	39,289	2.20	431,744	967,107	
	C3	2 Hr Transient - Test	12	6,956	1.64	129,408	262,698	
	B1	39 hrs - test	8	40,161	1.12	321,288	359,843	1.72
	B2	39 hrs - test	27	22,557	1.76	609,039	1,071,909	
	B3	39 hrs - test	10	5,633	1.28	56,326	72,097	
	C2	39 hrs - test	16	36,207	2.08	579,312	1,204,969	
	C3 (2D)	39 hrs - test	12	5,738	1.58	68,854	108,789	
Waterside BC-3	B1 No tree	39 Hr transient - test	8	29,926	1.69	239,408	404,600	1.67
	B2 - No Tree	39 Hr transient - test	27	29,926	1.69	808,002	1,365,523	
	B3 - No Tree	39 Hr transient - test	10	4,530	0.98	45,302	44,396	
	C2 - No Tree	39 Hr transient - test	16	29,926	1.69	478,816	809,199	
	C3 - No Tree	39 Hr transient - test	12	4,530	0.98	54,362	53,275	

4.5 DISCUSSION

4.5.1 Seepage Modeling

2-D and 3-D steady state and transient simulations were designed to recreate the flow tests and generate pore pressure distributions within the levees as input for slope stability modeling. The seepage simulations described in this volume are limited in terms of stratigraphy and the level of detail of the root system, particularly the Cal Expo 3D simulation. Nevertheless, the simulations were able to capture the retardation effect that a root system (alive or dead) has on the advancement of the saturation front across a levee prism.

Heave or uplift hydraulic gradients were not evaluated in these simulations, as the root systems were limited to the levee embankment; it is expected that for the analyzed cases the underseepage flow remains similar for scenarios with and without tree roots.

~~Animal~~ burrows were modeled as regions with high conductivity ~~for~~ potentially discontinuous holes, and open regions within the mesh ~~for holes~~ directly connected to the source of water. The high-conductivity regions were found to better represent pore pressure generation, as the open holes were assigned the same total head on the riverside or trench, overpredicting the pore pressures (especially for steady state conditions). For the slope stability analyses presented in this Volume, the simulations using high conductivity regions for simulation of the ~~animal~~ burrows were selected as input.

4.5.2 Stability Analyses

The landside tree did not have an important effect on global slope stability. Under steady state test conditions, failure scenario Landside A was modeled with and without tree loading. The factor of safety of Landside A with the landside tree and root system (1.83) was slightly higher than the factor of safety of the same section without a tree (1.80). Comparing the Landside A failure scenario with the control section, Landside C, the factor of safety of Landside A at steady state with a tree (1.83) was slightly lower than Landside C (1.98) at the control section. The difference appears to be due to differences in the pore water pressure accumulation in the lower portion of the slope in the area of Landside C. Pore water pressures within the Landside A area were heavily influenced by the extensive burrow network in the area as well as a gap in the overbank deposits on which the levee was founded that may have affected the patterns of pore water pressure accumulation. At Landside C, pore water pressures were also influenced by burrowing, but the network was far less extensive and geometry of the underlying low permeability overbank deposits are believed to have directed water away from the control instrument line (as discussed in Chapter 3).

Circular and block modes of failure were evaluated for each of the four (4) waterside and two (2) landside failure scenarios shown on Figure 4-2. In general, in the absence of horizontal loading or reinforcing, circular failure modes produced lower factor of safety values than block failure modes. Increasing the horizontal load through use of reinforcing elements or horizontal load forces (placed within the slide mass to represent the static tree lean and dynamic wind forces on the slide mass) influences the failure mode. Block failures were found to be critical for these cases with the waterside geometry.

The waterside oak tree case with various possible failure scenarios associated with observed cracking was evaluated. Based on hand calculations of the initial overturning moment of the tree, evaluated through tree weight, lean angle, and dynamic wind loading, the waterside tree initially had a pre-test factor of safety on the order of two with respect to overturning moments. Pore water pressures associated with the test conditions at steady state resulted in an estimated loss of approximately 40 percent of initial capacity, lowering the factor of safety against overturning to approximately 1.2. Shortening roots by making cuts at the crown trench during construction is estimated to have impacted

capacity by about 9 percent, reducing the factor of safety to about 1.02, just above unity. Seepage and slope stability modeling revealed that test conditions put greater demands on the levee than an actual flood scenario with a high water surface 3 feet below the levee crest.

Failure scenarios Waterside B-1 and Waterside B-2 exhibited low factors of safety under transient test conditions at 39 hours (approximate time that the waterside oak tree fell). Based on models, Waterside B-2 exhibits a slightly higher factor of safety with the waterside oak tree than without it. The Waterside BC3 failure scenario was found to have a factor of safety against instability of greater than 1.5. The movements may have been related to consolidation of loose fill deposits under wetting, instability related to ~~animal~~ burrows or preferential planes of weakness, soft soil layers or fractures within the fill that were not captured through careful logging of site conditions.

Waterside slopes were comprised of weak, uncompacted fills of variable quality. These weak fills were found to be riddled with burrows and pockets of very loose fill. The impact of the trees on slope stability was found to be minimally helpful in improving stability of these weak fills, to the extent that the tree remains stable to overturning due to wind or static loading associated with lean or steep slope angles. Trees that lean significantly (particularly those with a center of mass extending leeward of the root plate) should be evaluated carefully and removal considered. Trees not exhibiting excessive lean should be evaluated for other potential impacts such as erosion and windthrow to determine whether the tree may remain and possibly provide a small benefit to global stability.

5 MODELING ~~ANIMAL~~ BURROWS AND OTHER DISCONTINUITIES

5.1 IDEALIZED SIMULATIONS

To study the influence of ~~animal~~ burrows encountered in the two mammal burrow field tests (Volume 4) a series of two-dimensional seepage analyses was performed with the objective of simulating the effects of open discontinuities on wetting front progression, piping potential and time to saturation of an earthen embankment. More specifically, the objectives of the simulations presented in this section are to examine whether a discontinuity or a macropore in a soil mass can become an important source of flow that may induce piping or faster saturation of a levee.

The base case of analysis is an idealized box of soil (Figure 5-1) with a circular discontinuity to simulate the presence of a burrow in cross-sectional view. Initial conditions for the model consist of a phreatic line near the base of the model so a profile of vertically increasing suction is generated. Boundary conditions on the burrow are set by applying review nodes (potential seepage face) along the burrow walls. Transient conditions are achieved as a total head is applied along the nodes on the top of the model and a saturation front is created. Discharge into the burrow is estimated using a flux section across the discontinuity and saturation values are estimated on the nodes around the discontinuity for each time step of analysis. Results of the simulation are shown in

Figure 5-2 by normalizing the flux into the discontinuity (void) by its discharge capacity and plotting it as a function of saturation (volumetric water content for each time step divided by saturated volumetric water content for the soil).

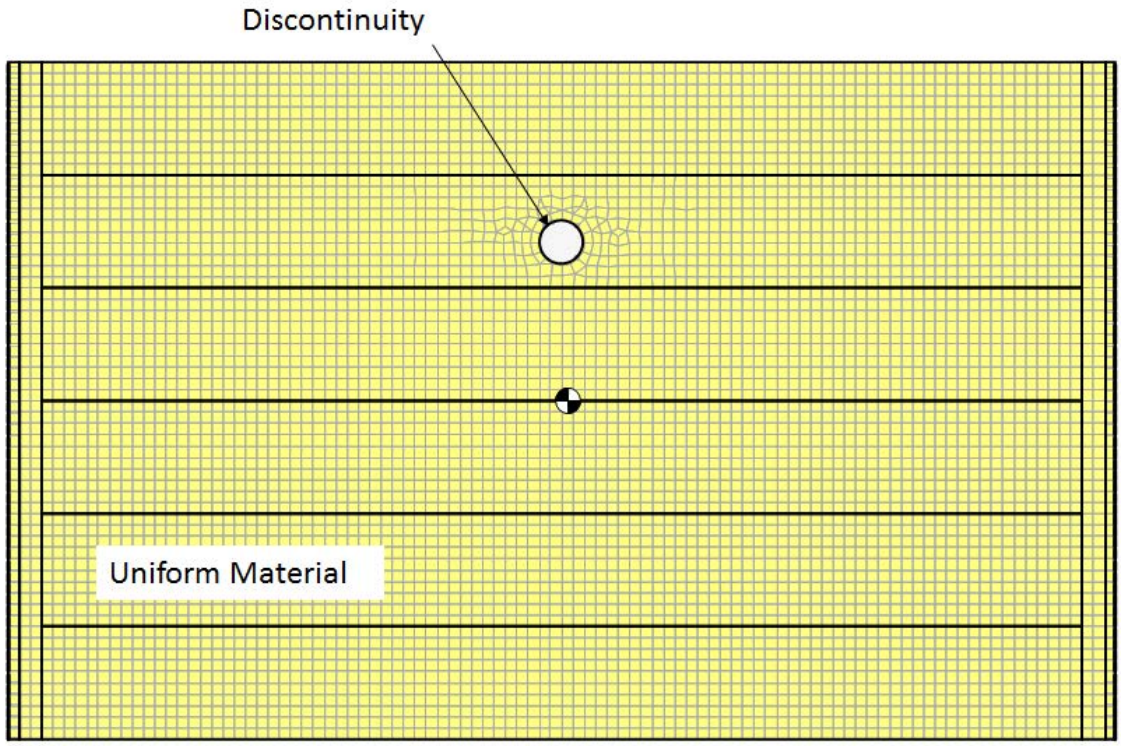

Figure 5-1. Idealized model section.

The plot in Figure 5-2 illustrates a simple yet important point. A void within an unsaturated mass of soil will not become an important flow channel unless the soil around it is either saturated or directly connected to a source of water. The flux values for saturation values below 50% are less than 1% of its capacity at saturation, and the flux becomes significant only after saturation exceeds 95% around the void.

The second conceptual model considered a single horizontal void shown in cross section view (Figure 5-3). This time, total heads are applied on the left vertical edge of the model to achieve a unit gradient across the idealized box of soil, and again flux into the cavity (grey cluster) was computed as a function of saturation and time. Two sets of analyses were performed using this configuration. In the first simulation the soil was assigned sand-like properties and in the second the soil was assigned silt-like properties. The soil water characteristic curves used for both ~~models~~ are shown on Figure 5-4; saturated hydraulic conductivities were assumed as $1x10^{-3}$ cm/s and $1x10^{-5}$ cm/s for the sand and silt, respectively. Unsaturated properties were derived using the Van Genuchten (1980) relationship.

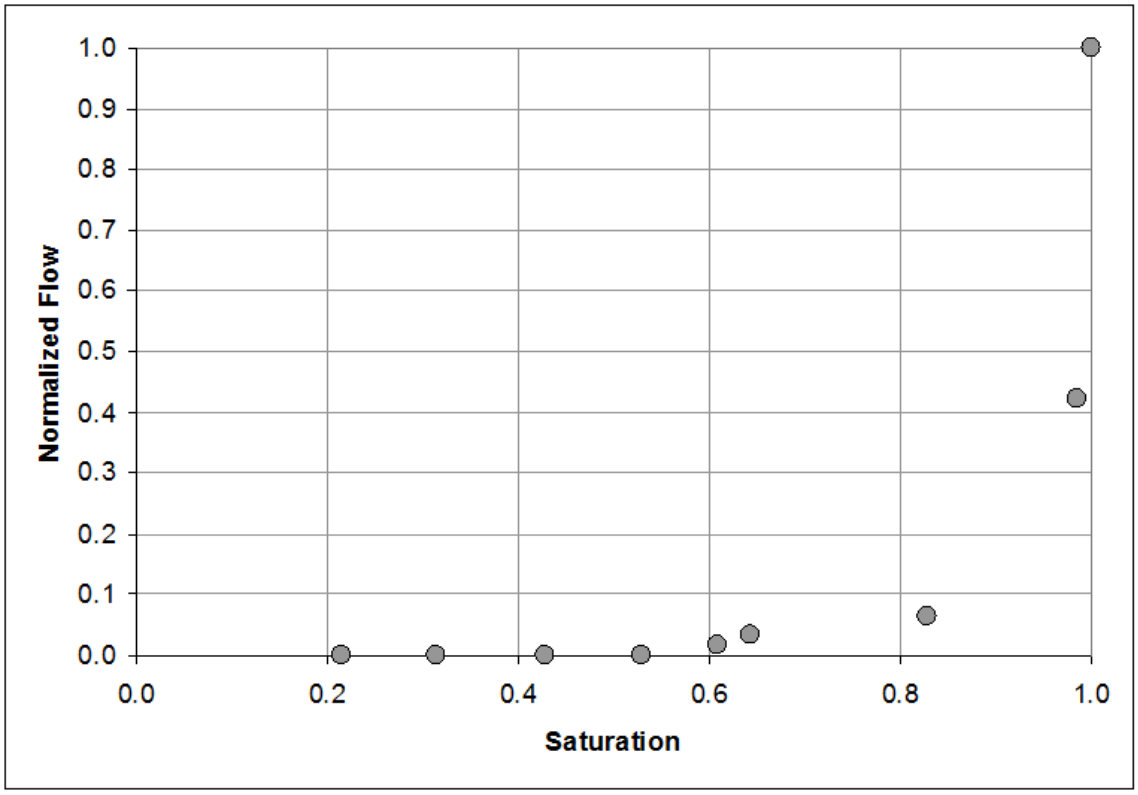

Figure 5-2. Results of idealized model.

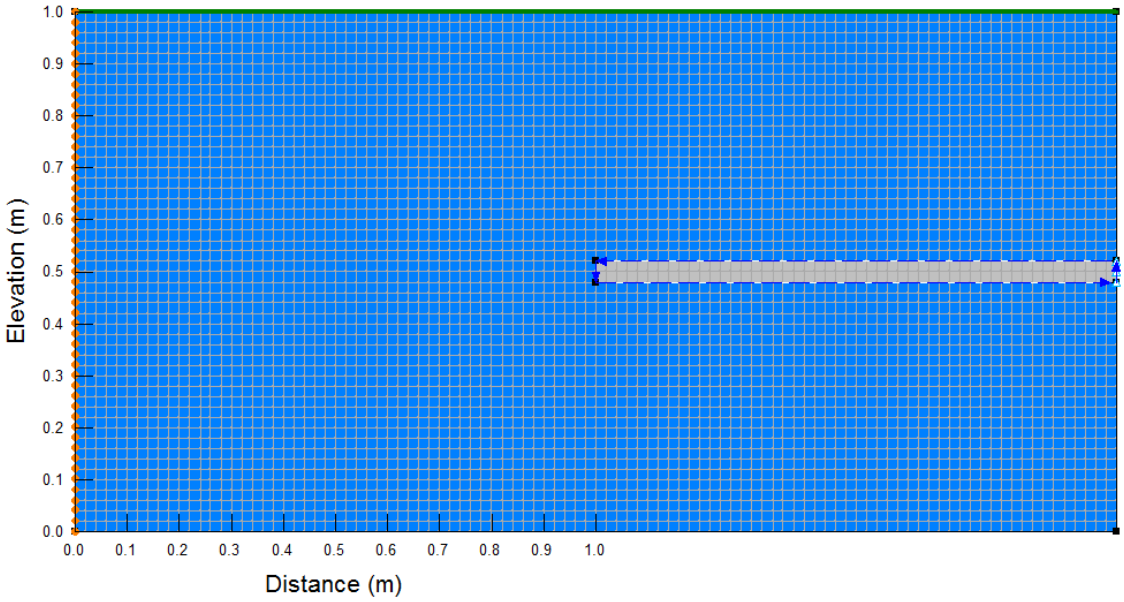

Figure 5-3. Idealized model for flow into a single cavity.

The normalized values of discharge as a function of saturation are shown on Figure ~~6-47 and Figure 6-48~~ for the coarse-grained and fine-grained materials, respectively. As can be seen, the coarse-grained material, which started from an initial saturation of 10%, saturates rapidly given the high hydraulic conductivity and correspondingly the flux into the cavity rapidly increases. In contrast, the fine-grained material saturates more slowly and the flux also increases much more slowly with its magnitude depending very much on the initial saturation. Maximum computed discharge for the sand model was on the order of 10^{-6} $m^3/s/m$, and for the fine-grained model 10^{-9} $m^3/s/m$. The hydraulic gradients were greater than 10, which may be indicative of the potential for large deformations of the soil near the walls of a discontinuity and, consequently, may lead to the collapse of the void before saturated water flow initiates.

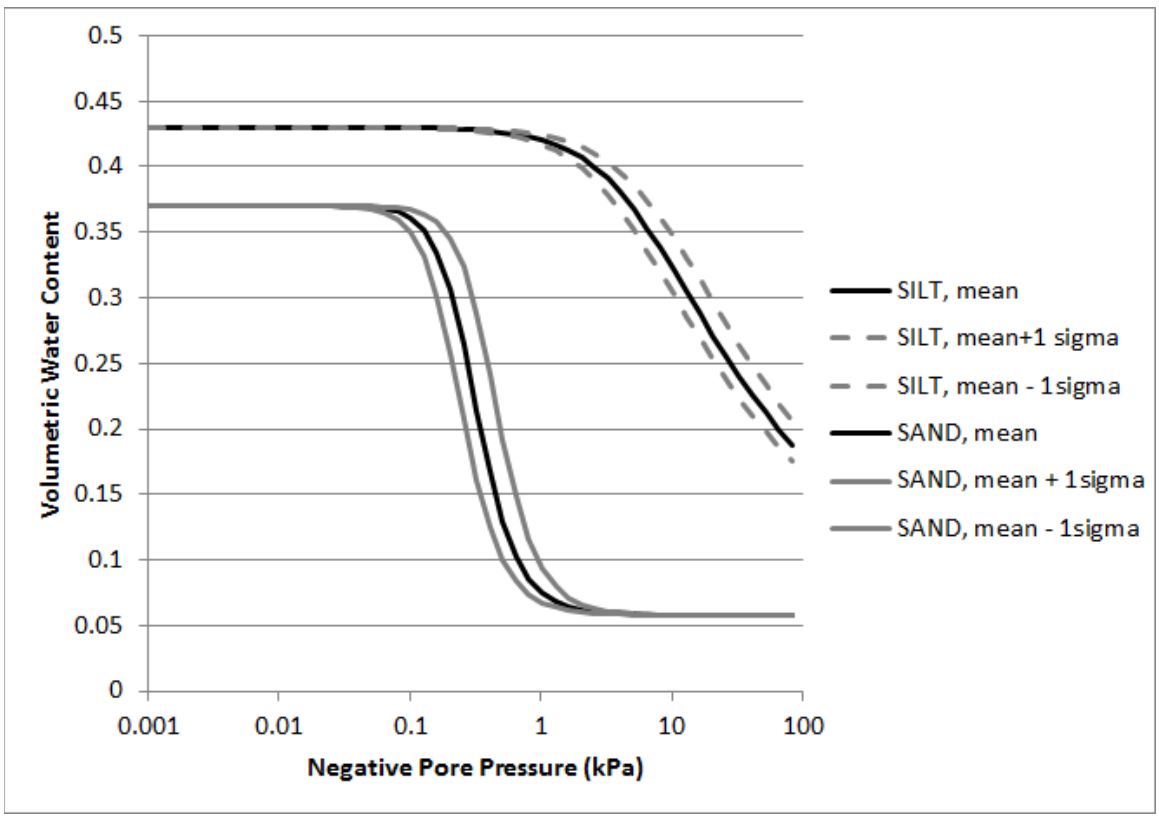

Figure 5-4. Material properties for single-cavity idealized model.

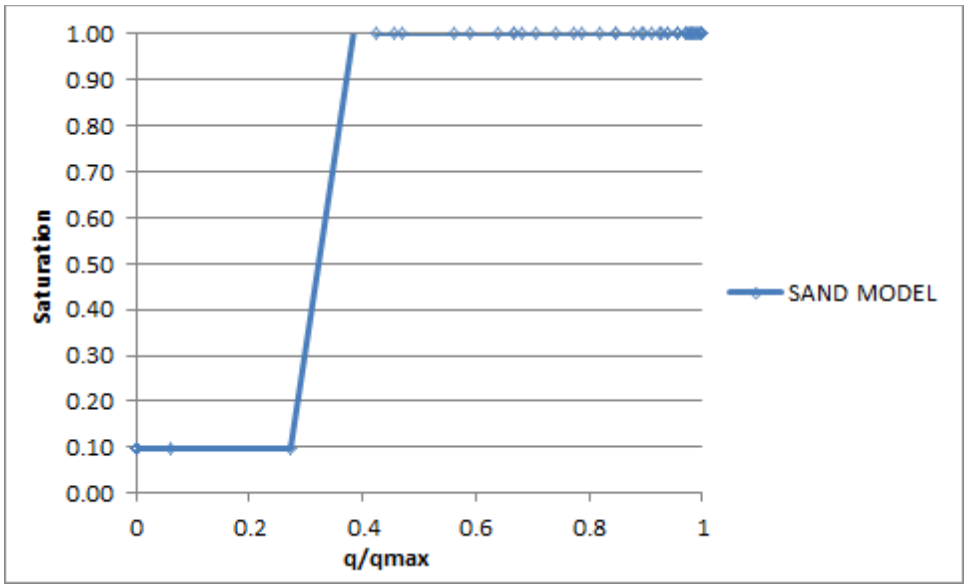

Figure 5-5. Results of the single-cavity idealized model using sand.

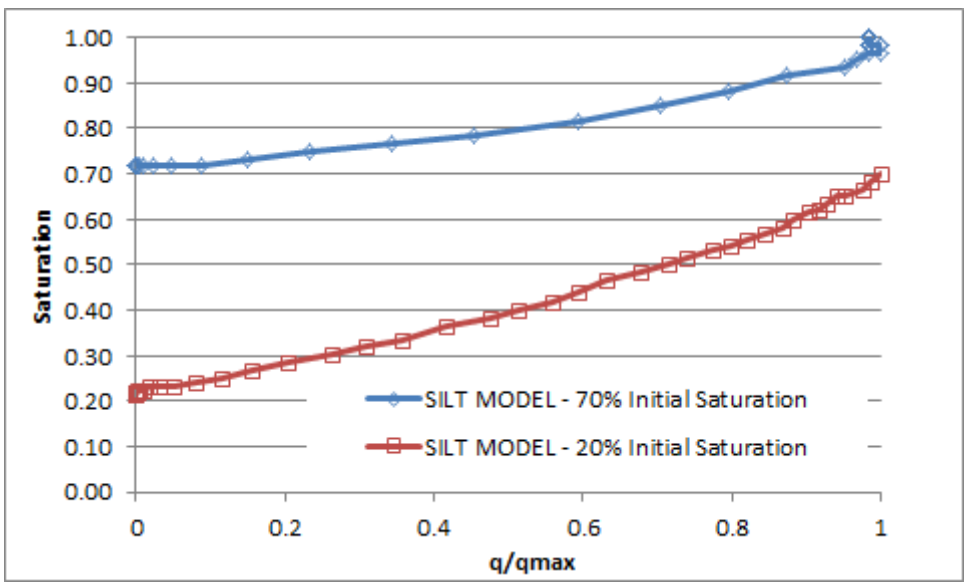

Figure 5-6. Results of the single-cavity idealized model using fine-grained soil.

The third idealized simulation considered three voids (green regions on Figure 5-7) within the mass of soil, two of these connected to the downstream 'seepage face', and a third one on the upstream edge of the model. Boundary conditions were the same as previously described, and the total heads were also applied along the interface of the hole on the upstream edge of the model. The fluxes into each cavity (Figure 5-8) after 5 days of simulation were $5x10^{-8}$ and $5x10^{-6}$ $m^3/s/m$ for the upper and lower discontinuity, respectively. These are similar to the computed flux through the entire cross section assuming no discontinuities were present (Figure 5-9), with a value of $1x10^{-6}$ $m^3/s/m$. The blue line represents the position of the saturation front at the time indicated in the plot.

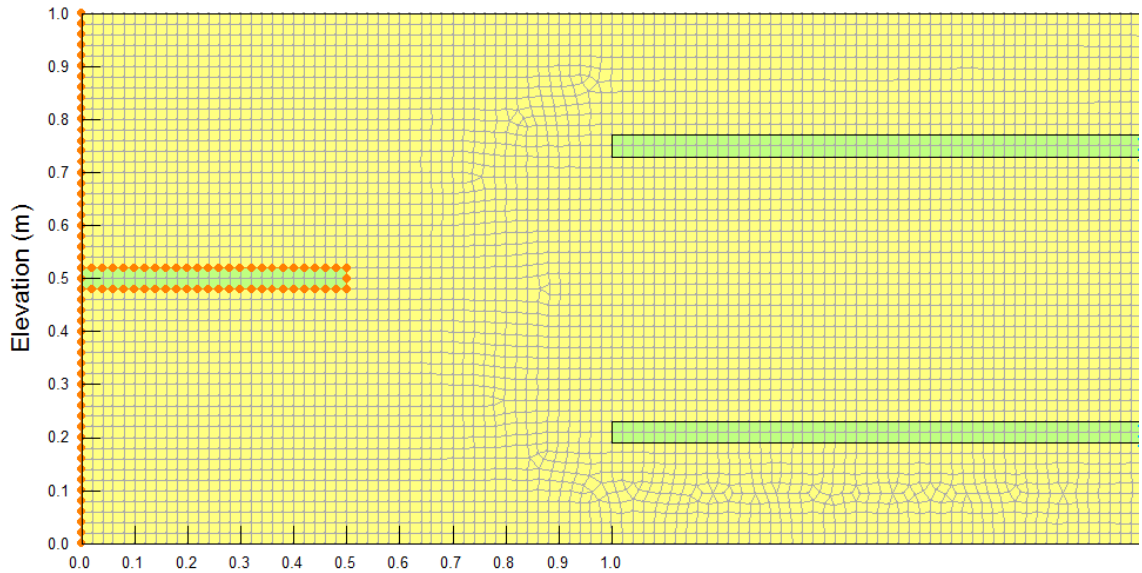

Figure 5-7. Multiple cavity idealized simulation.

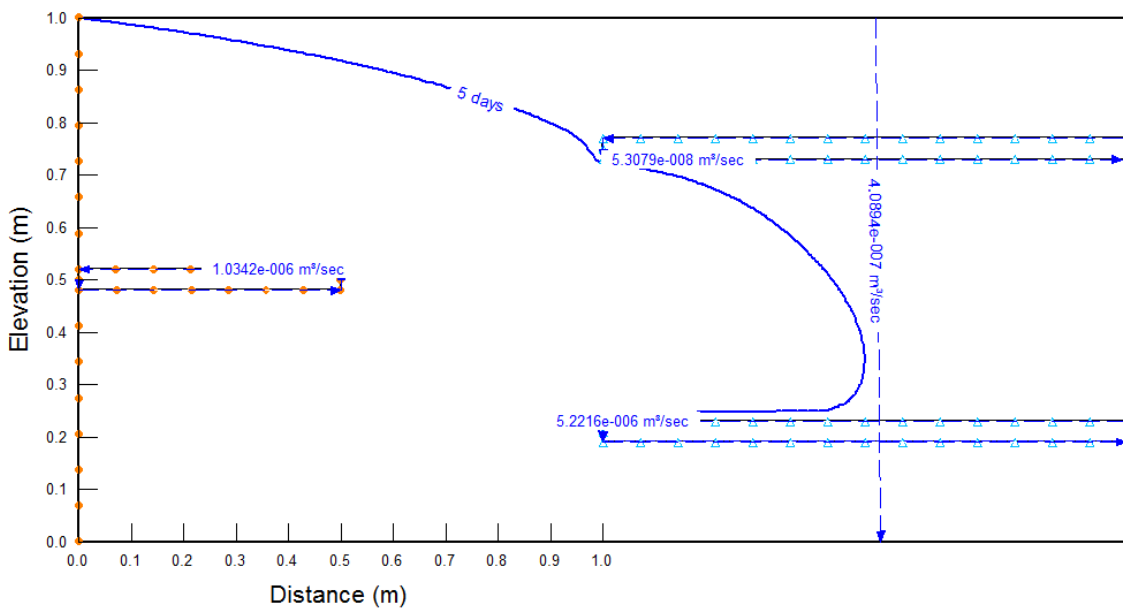

Figure 5-8. Multiple cavity simulation results.

These idealized models are intended to show the influence of open discontinuities on the wetting patterns of unsaturated masses of soil, and whether a hole can potentially become an important flow channel within the soil mass. The results show that the amount of water flowing into (and out of) a void depends on the hydraulic conductivity of the soil around the void, and the degree of saturation of the soil mass. For the case shown on Figure 5-8, the computed discharges into the discontinuities are in the same order of magnitude as the flux through the entire cross section (Figure 5-9).

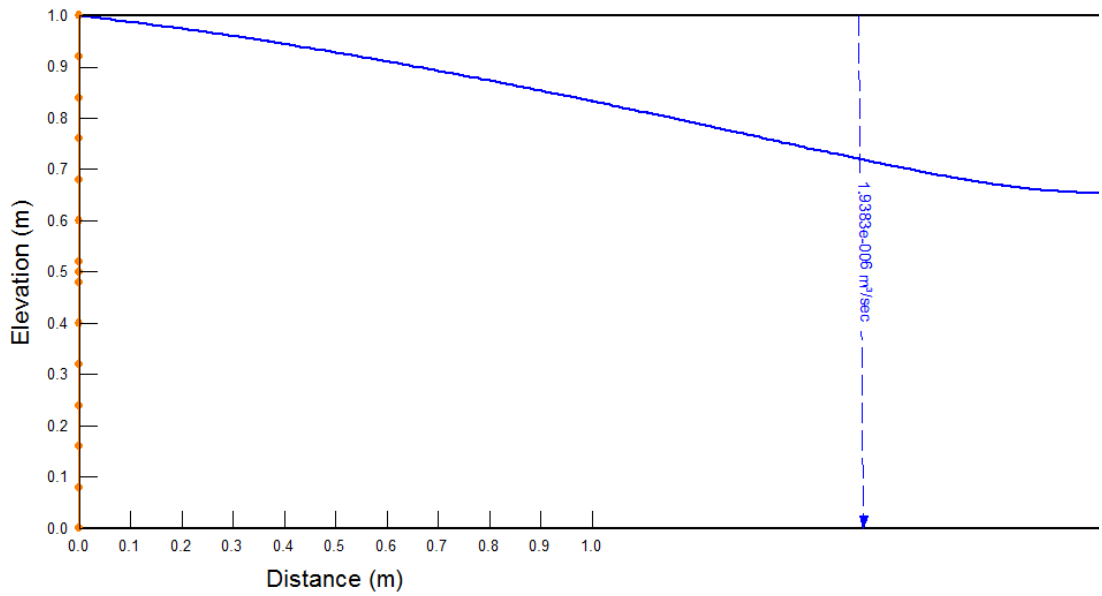

Figure 5-9. No cavity simulation results.

5.1.1.1 ~~ANIMAL~~ BURROW SEEPAGE SIMULATION

The two ~~animal~~ burrow field studies described in Volume 4 were used ~~to~~ as a basis for a series of simulations mimicking the discontinuous network of burrows. The first model is a two-dimensional representation of the burrows encountered in the 'Sandy Levee Site', where a single large burrow was encountered on the waterside toe, and a large complex of surficial burrows was found along the landside slope. For simplicity, the section was analyzed as a two-dimensional cross section, so the burrow system was 'collapsed' into a single cross section (Figure 5-10). The profile consists of a relatively clean sand levee with slopes of approximately 2H to 1V overlaying a silty foundation. Saturated hydraulic conductivities were assumed to be $1x10^{-3}$ cm/s and $1x10^{-5}$ cm/s for the sand levee and its silty foundation, respectively. Unsaturated properties were derived using the Van Genuchten (1980) relationship.

Boundary conditions consisted of a seepage face along the downstream levee surface and toe areas, as well as along the inner boundaries of the burrows open to atmospheric pressure on the downstream half of the embankment. Constant head boundary conditions were applied along the upstream levee slope and channel, assuming that the head was equal to the elevation of the levee crown.

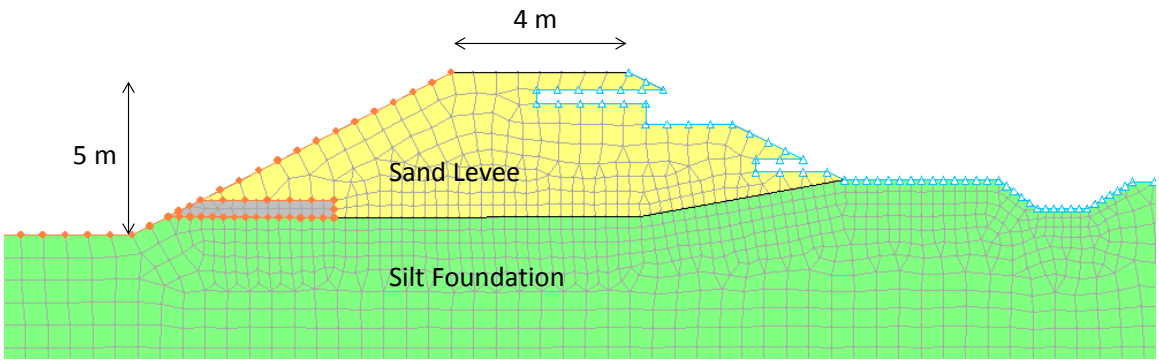

Figure 5-10. Simplified representation of animal burrow networks.

The results of the steady state simulation are shown on Figure 5-11. The resulting flow field indicates that the combined effect of the water side burrow and the burrow near the downstream toe of the levee ~~is to~~ shorten the seepage path and increase the gradient. The water side burrow allows the full water side head to ~~reach~~ into the levee ~~and~~ the land side burrow acts as a toe drain, concentrating flow paths and velocities toward the burrow. In contrast, ~~the~~ burrows located near the levee crown have little influence on the distribution of heads as the crown of the levee is likely to remain unsaturated even under steady state conditions

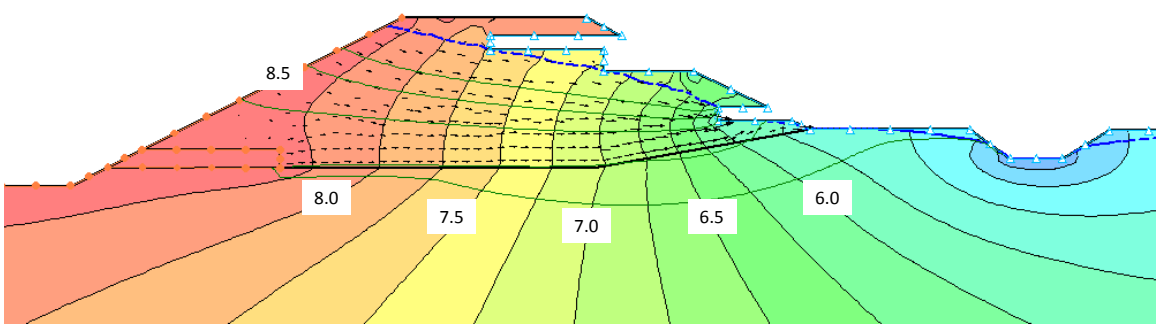

Figure 5-11. Steady state simulation of Sandy Levee Site burrows. Total head contour interval 0.25 m.

~~The~~ second simulation was performed to analyze the influence ~~that the~~ location of a ~~completely penetrating~~ burrow has on the distribution of gradients within the embankment and on ~~the~~ piping potential. Figure 5-12 ~~shows~~ the section ~~employed~~, with three model burrow locations labeled A, B and C, extending from one to three meters below the crown of the levee. Boundary conditions, material properties and model dimensions were ~~kept~~ the same as in the previous simulation.

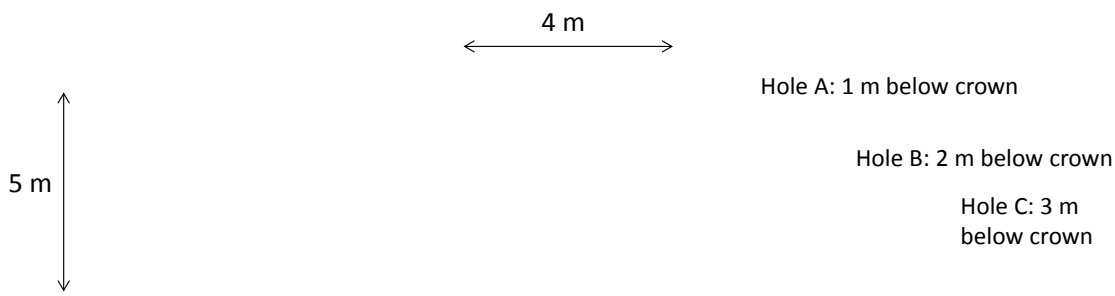

Figure 5-12. Input section for completely penetrating burrows.

Figure 5-13 shows the simulation results for model burrow C (3 m below levee crown) in terms of head distribution for a transient simulation of one day. At this point in time the geometry of the seepage front is similar to the saturation pattern observed in the case with no burrow (Figure 5-11). A pore pressure profile across a vertical section through the centerline of the embankment for this case is shown on Figure 5-14. The plot indicates that the presence of the burrow near the ~~foundation level~~ will ~~produce a~~ faster saturation of the embankment. After two hours, the section with a ~~hole~~ near the ~~bottom~~ of the embankment has reached the maximum head value (about 7.5 m), whereas the section with no ~~holes~~ reaches this value in about 20 hours.

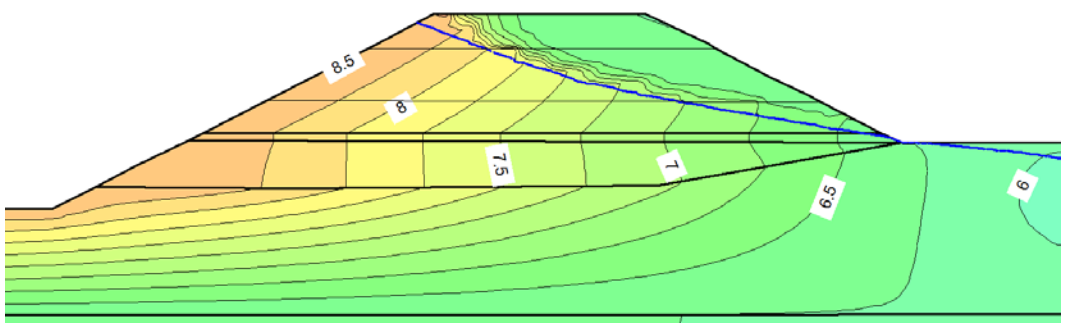

Figure 5-13. Results from transient analysis after one day of simulation with burrow C. Contour interval: 0.25 m.

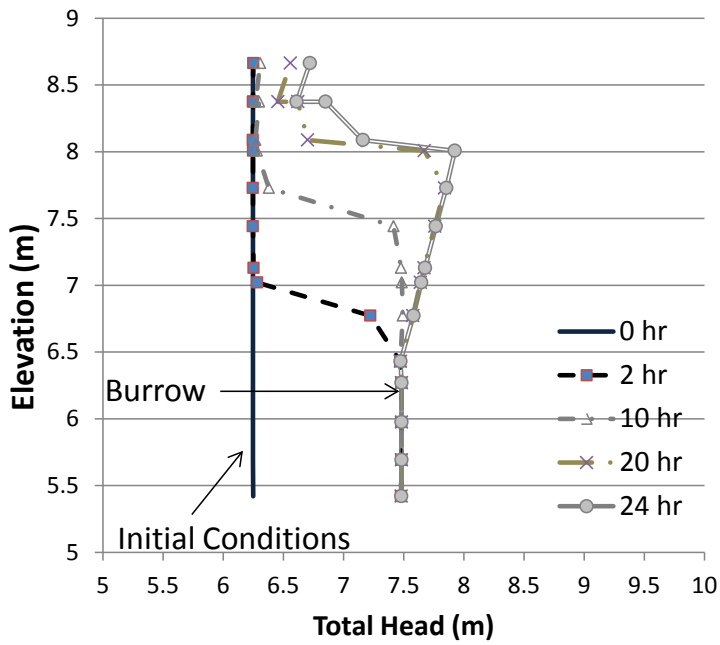

Figure 5-14. ~~Evolution of~~ pore pressures on a vertical section across the levee crown for burrow C.

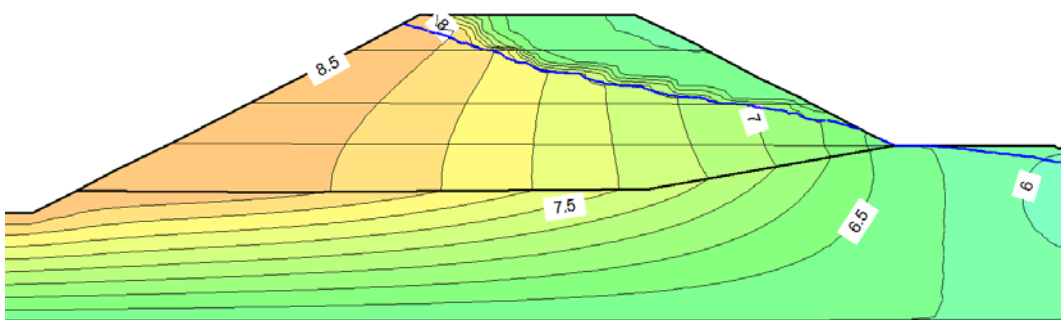

Figure 5-15. Results from transient analysis after one day of simulation. No holes present. Total head contour interval: 0.25 m.

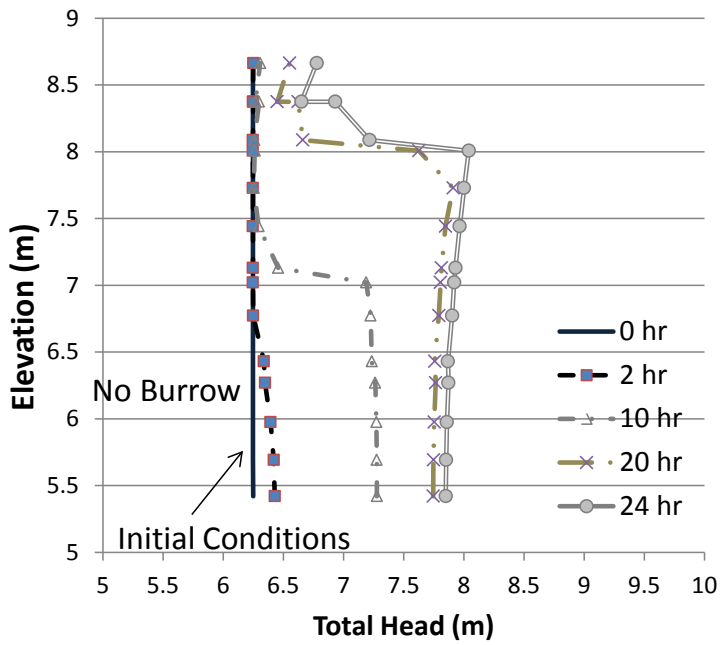

Figure 5-16. ~~Evolution of~~ pore pressures on a vertical section across the levee crown for the case of no ~~hole~~

The results from the simulations with a burrow at location A (1 m below levee crown) and B (2 m below levee crown) are shown in Figure 5-15 and Figure 5-16, respectively. The pore pressure evolution across the centerline of the levee along A (Figure 5-18) and along B (Figure 5-20) indicates a similar behavior similar to that observed with the burrow located near the bottom of the embankment: the soil in the vicinity of the hole reaches its maximum head very rapidly (two hours) because of seepage from the burrow, which results in a shorter saturation time for the entire embankment along modeled section.

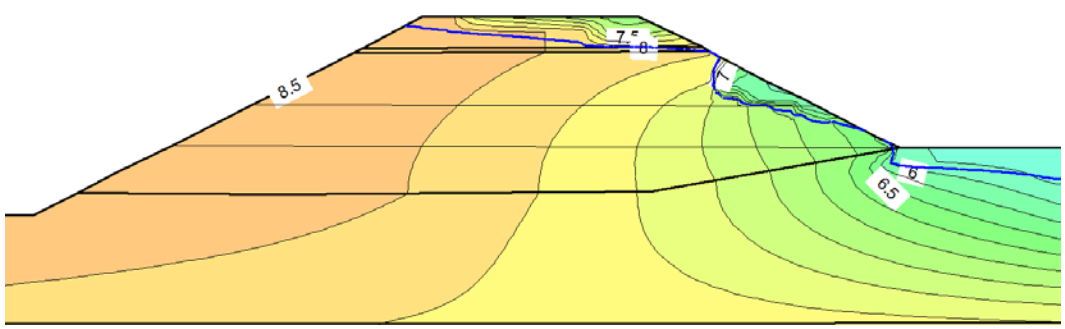

Figure 5-17. Results from transient analysis after one day of simulation with burrow at A. Total head contour interval: 0.25 m.

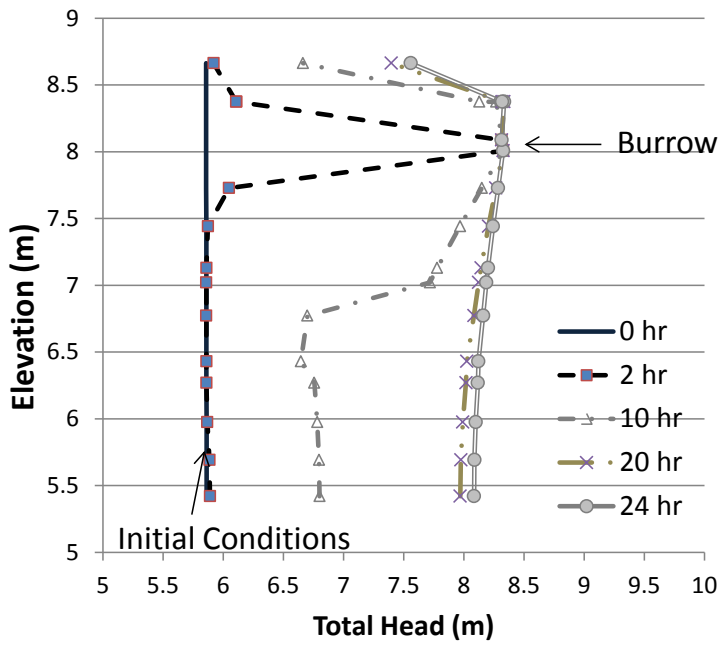

Figure 5-18. Evolution of pore pressures on a vertical section across the levee crown at burrow A

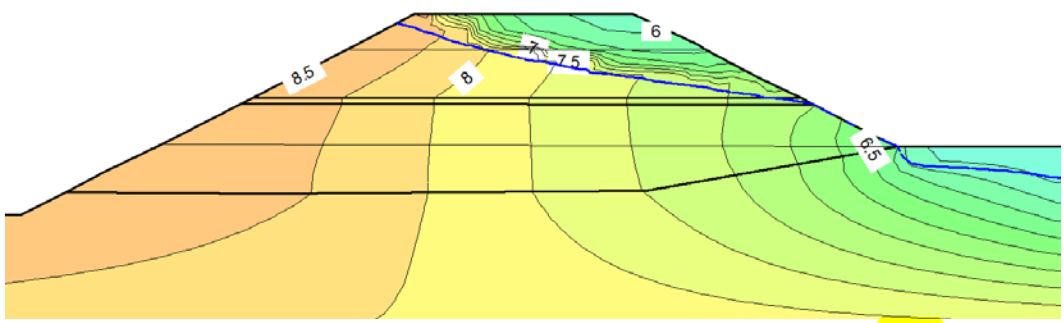

Figure 5-19. Results from transient analysis after one day of simulation at Hole B. Total head contour interval: 0.25 m.

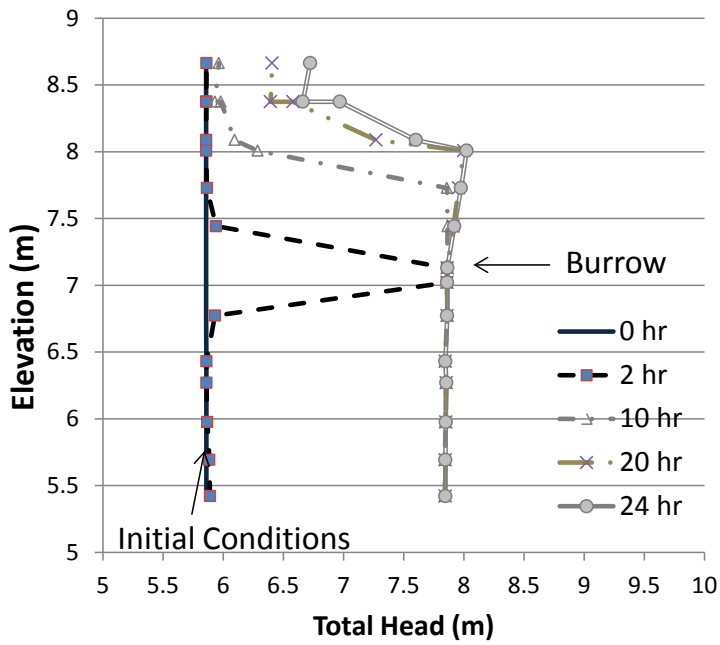

Figure 5-20. ~~Evolution of~~ pore pressures on a vertical section across the levee crown for the burrow at B

5.2 PIPING POTENTIAL OF COMPLETELY PENETRATING BURROWS

Piping is the development of a channel below or through a levee that is opened and widened by shear force of groundwater flow concentrated along a void. Piping potential is controlled by three processes (Sellmeijer, 2006): (1) groundwater flow through the soil matrix, (2) water flow along the pipe or discontinuity, and (3) the state of limit equilibrium of the particles at the bottom of the pipe or discontinuity. A model that incorporates these phenomena is not commercially available, yet empirical formulae have been developed to assess the triggering of this issue. The Lane (1935) and Bligh (1910) methods relate ~~the~~ levee geometry with a series of coefficients to estimate a critical head over which piping would occur. Sellmeijer (1988) created a more robust procedure that incorporates particle characteristics as well as the geometry of ~~the~~ levee to estimate a ratio of critical head to the width of ~~the~~ embankment. More recently, Ojha (2003) developed a procedure based on flow velocity along the soil/void interface and particle diameter to estimate a critical traction velocity for initiation of the piping process. The results of the transient simulation for burrow C (3 m below levee crown) were used for piping potential estimation, employing the Ojha (2003) and Sellmeijer (1988) formulas.

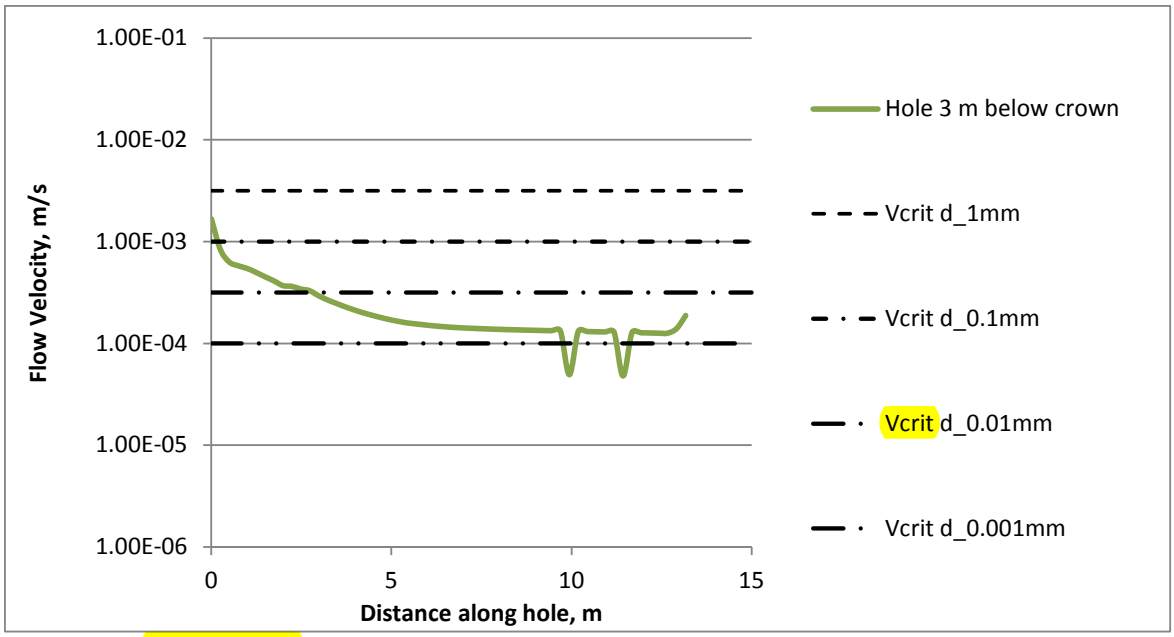

Figure 5-21. Piping potential evaluation using the Ohja (2003) formula.

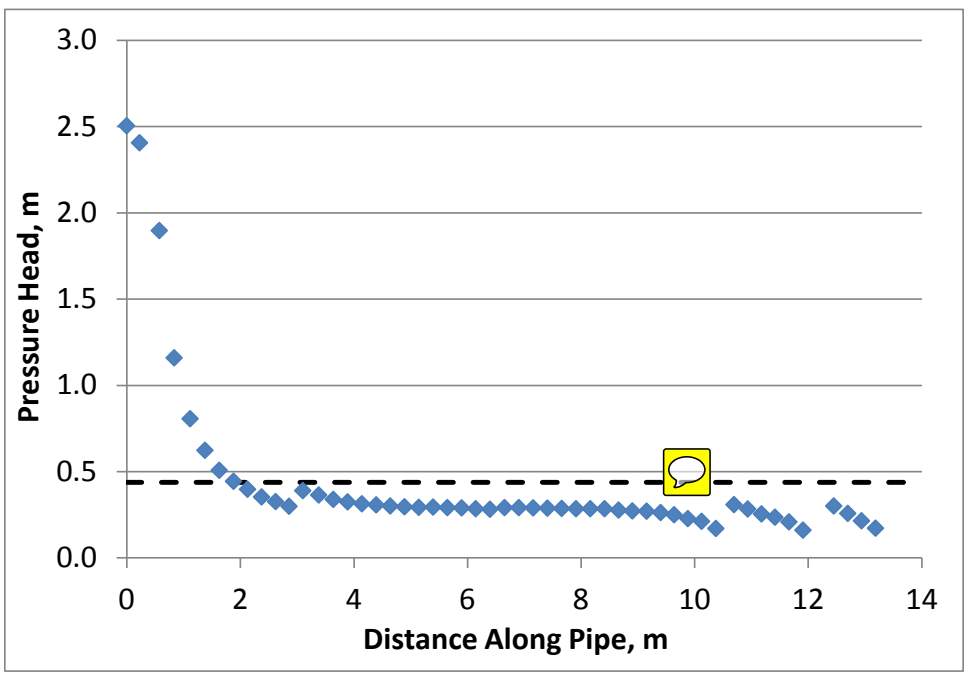

Figure 5-22. Piping potential evaluation using the Sellmeijer (1988) formula.

The green series on Figure 5-17 represents the longitudinal profile of velocities along the soil/burrow interface. The data is compared to four critical velocity values according to Ohja (2003), for particle sizes ranging from 1 mm to 0.001 mm. The plot shows that the computed velocity field along the bottom of the burrow is sufficient for piping initiation. Similarly, using the Sellmeijer (1988) formula for a critical potential head value for a sandy

soil with a D_{70} of 0.03 mm, piping would initiate along the first several meters from the upstream entrance to the burrow.

5.3 CLAYEY SITE LEVEE SIMULATION

A simulation of ~~the~~ conditions ~~in~~ March 1998 ~~during high water levels on the clayey~~ (Figure 5-~~19~~) ~~site~~ was performed to further compare the simulation results to a well-documented case history. A 3D finite element model of the 2 m (6 ft) tall levee, with 2:1 slopes and 2.4 m (8 ft) wide crown (Figure 5-2~~0~~) was constructed. The silty (67% fines) levee and foundation materials were assigned a saturated hydraulic conductivity of $5x10^{-6}$ cm/s, and unsaturated properties were estimated using the VanGenuchten (1980) equation, as before.

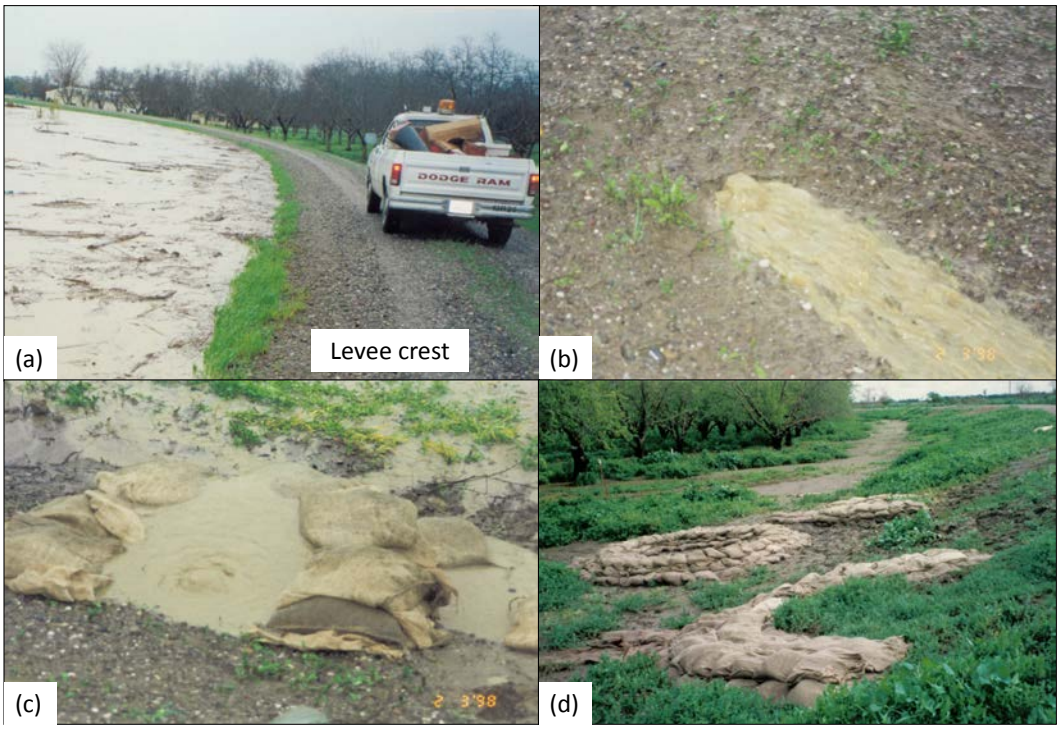

Figure 5-23 High water on Clayey Levee Site in 1998. Images courtesy Al Romero, DWR.

Waterside boundary conditions were a constant head corresponding to water level located 0.15 m (0.5 ft) below the levee crown. Landside boundary conditions were represented with a constant head corresponding to water level 1 m (3ft) below the levee toe along the right vertical mesh boundary. The continuous burrow was modeled using saturated high conductivity elements located 1 m below the levee crown. Potential seepage faces were assigned along surfaces on the landside slope face and ground surface. Only steady state simulations were performed, as the burrow was connected to the ~~river~~side, thus making the analysis of saturation progression of the fine-grained embankment irrelevant.

The value of hydraulic conductivity of the burrow was varied in the analyses and the resulting velocities along the hole/soil interface were compared with velocity values for piping potential according to Ohja (2003). Figure 5-21 shows the range of flow velocities obtained by varying the conductivity values of the burrow between 0.1 and 0.01 cm/s. Computed flow velocities along the hole range between 0.003 and 0.0003 m/s, which appear to be sufficient to trigger internal erosion for particle sizes above 0.01 mm. These velocity and piping potential estimations corroborate the observations during the high water in 1998 and show that a simplified approach to modeling burrows or other discontinuities in levees is adequate.

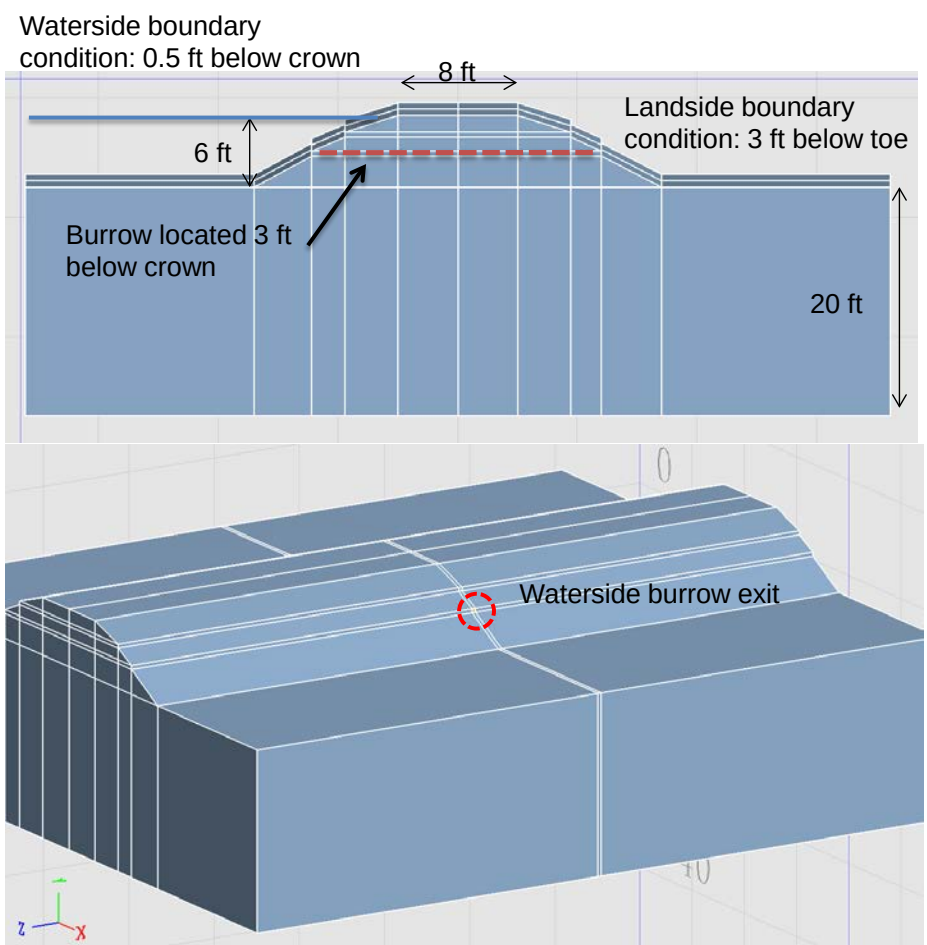

Figure 5-24. Clayey levee site 3D model

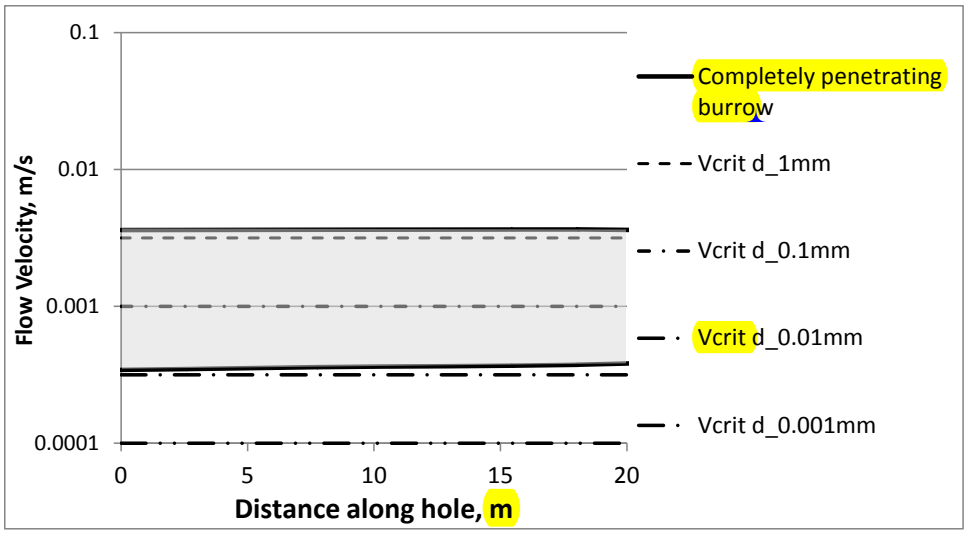

Figure 5-25. Critical flow velocities for ~~different~~ particle sizes compared to range of velocities along burrow

6 CONCLUSIONS

The data gathered during the seepage field test program ~~showed~~ that wetting fronts tend to progress ~~slower~~ through and around ~~the~~ root system than through sections with no roots, suggesting that the discontinuities found around some roots have little influence on accelerating groundwater flow and low likelihood of initiating erosion processes.

These observation are supported by the results of an extensive set of seepage simulations, which show ~~that~~ discontinuous voids, such as could be formed by decomposed root systems, do not provide a direct seepage path ~~such that for~~ high flow velocities could develop. In cases where a given root is completely decomposed, its space is generally filled with decomposed ~~matter, or *frass*,~~ and tends to be looser than the surrounding soil, creating zones of higher hydraulic conductivity. However, while this condition could produce a faster advance of the wetting front, by relatively rapid saturation of localized zones within ~~the~~ levee, the flow quantities and velocities would not be high enough to trigger piping or internal erosion processes.

~~Animal burrowing~~ clearly ~~has~~ a much larger influence than roots given their larger diameter, length and continuity throughout ~~the~~ embankment than the live and decomposed roots observed in this research program. Of special interest are burrows or burrow ~~systems~~ extend~~ing~~ from ~~the~~ waterside slope towards ~~the~~ landside slope, such as the one encountered on the clayey levee (Volume 4)~~, which~~ have the potential of eroding ~~the~~ levee material because the flow velocities can potentially reach critical values to trigger piping.

These observations are supported by numerical simulations performed to back-calculate the seepage tests and a historical account ~~in~~ one of the ~~animal~~ burrow sites. The models presented herein are relatively simple, yet intended to highlight the critical issues related to seepage performance of levee embankments when affected by biotic activity. ~~The animal~~

burrows were modeled using two different approaches: (a) using a void region and applying the total head values at the walls of the burrow when the burrow was directly connected to a source of water; and (b) using high-conductivity clusters to simulate the fast transmission of water along a potentially discontinuous hole. In general, the first method of simulating the voids proved to overpredict pore pressures in the vicinity of the holes (especially for steady state analysis conditions) and produced very low factors of safety in slope stability calculations. Overall, a number of factors govern the specific seepage patterns in a levee including, the continuity of the macropores, their location and distribution vertically and horizontally, and the type of soil which governs the rate of saturation. In general, deeper animal holes or macropores connected to the waterside will be subject to larger hydraulic heads, and thus higher flow velocities than those located near the crest. However, piping can be triggered even along relatively shallow discontinuities, as long as they are directly connected to the source of hydraulic loading and have an exit face.

On the clayey levee piping occurred along a burrow which experienced a head of only about 80 cm (2.5 ft). The degree of saturation and the amount of water flowing into a macropore not directly connected to the river side is dependent on the hydraulic conductivity of the soil. Unsaturated fine-grained soil will have a very low conductivity and thus the flux of water into the hole will consequently be low and as saturation increases the discharge into the discontinuity will increase. Conversely, for a macropore/burrow open to the water side the saturation level of the soil surrounding soil controls the rate of seepage out. Finally, the continuity of macropores is equally important as water side macropores terminating a short distance from a land side macropore will tend to produce very high hydraulic gradients and potential for piping.

The slope stability analyses using the data from the field wetting tests and from seepages simulations show that the presence of a tree has little to no effect on the factor of safety against seepage-induced instability. Factors of safety were nearly identical or slightly higher for the sections with a tree as opposed to those without a tree. The effects of tree lean and wind can place a load on the slope that is likely to vary with conditions and tree species. This load can be evaluated using a simplified approach consisting of mass-averaged 2D modeled sections. Tree loading is applied over a zone determined by the size of the root plate, estimated with windthrow data for the particular. Advances in root architecture and windthrow understanding as applied to these types of analyses, as well as advances in slope stability software to add flexibility in the application of tree and root reinforcement and loading would greatly facilitate the modeling of trees in future slope stability analyses.

- The presence of a tree has little to no effect on the factor of safety against instability. Factors of safety were nearly identical or higher for the sections with a tree as opposed to those without a tree.

- The Twitchell Island field test waterside tree appears to have fallen due to horizontal forces placed on the root system associated with extensive tree lean and wind loading. The most likely failure scenario for the waterside oak tree is B-2.

where the failure ~~scenario~~ extends to the hinge-point of the waterside slope. ~~The~~ slope ~~is likely to have experienced movement during the flow test~~ with or without the presence of the waterside tree.

- The Twitchell Island ~~field test~~ landside tree ~~performed acceptably~~ under saturated conditions and gusting wind conditions, showing ~~a modest~~ rotation of about 0.12 degrees (or about 2 inches measured 6.5 feet up from the base of the tree) based on LiDAR data provided by ~~Gerald Bawden of the~~ USGS.

7 REFERENCES

Bligh, W., 1910, Dams Barrages and Weirs on Porous Foundations, Engineering News, p. 708.

Chapuis, R., 2004, Predicting the Saturated Hydraulic Conductivity of Sand and Gravel Using Effective Diameter and Void Ratio. Can Geotech J. 41: 787-795.

Chung, S., Bawden, G., Keightley, K., Bond, S., Lichter, J., Berry, A., (in press), Tree Dimensional Quantitative Characterization of in-situ Tree Root Architecture using Ground-Based Tripod LiDAR Scanning, New Phytologist.

Cobos-Roa, D., Shriro, M., Sitar, N., Bray, J.D., Bawden, G., Lichter, J., and Evans, R., 2012, 3-D Stratigraphy and Root Geometry From Trench and Ground-Based LiDAR Mapping, American Society of Civil Engineers GeoCongress 2012, Oakland, CA, March.

Cobos-Roa, D. (2014, in press). *The Role of Transient Conditions on Levee Performance*. Ph.D.. University of California, Berkeley.

Duncan, J. M., & Wright, S. G. (2005). *Soil strength and slope stability*.

Federal Highway Administration (FHWA) (2002), NHI Course No. 132031, Subsurface Explorations – Geotechnical Site Characterization.

Gerke, H., Van Genuchten, M. Th., 1993, A Dual-Porosity Model for Simulating the Preferential Movement of Water and Solutes in Structured Porous Media, Water Resources Research, Vol. 29, No.2, pp 305-319, February.

Hatanaka, M. and Uchida, A. 1996. Empirical correlation between penetration resistance and effective friction of sandy soil, Soils & Foundations, Vol. 36 (4), Japanese Geotechnical Society, 1-9.

Hatheway, A. W. (1982). "Trench, shaft and tunnel mapping". Association of Engineering Geologist Bulletin, v.19, p.173-180.

Lane, E.W., 1935, Security from Under-Seepage under Dams on Sand, Proceedings ASCE, Paper No. 1920.

Mitchell, J.K. 1976. *Fundamentals of Soil Behavior*, Second Edition, John Wiley & Sons, New York, 437p.

Ohja, C., Singh, V., Adrian, D., 2003, Determination of Critical Head in Soil Piping, ASCE Journal of Hydraulic Engineering, Volume 129, Issue 7, July.

Peterson, C. (2012). *California Levee Vegetation Research Program Windthrow Project*, California Levee Vegetation Research Program (CLVRP) Symposium–, August 28, 2012. http://www.safca.org/2012_Symposium_Presentations_Day1.html

Seed, R.B., Mitchell, J. K., and Seed, H.B. (1990). Kettleman hills waste landfill slope failure. II: stability analysis. Journal of Geotechnical Engineering 116 (4), 669-690.Sellmeijer, J.B., 1988, On the Mechanism of Piping under Impervious Structures, LGM-Mededelingen, No. 96, October.

Sellmeijer, J. B., 2006, Numerical Computation of Seepage Erosion below Dams (piping).

Shriro, M., Cobos Roa, D., Bray, J., Sitar, N., Lichter, J., Evans, R., Kroll, R., 2011, Study of Levee Seepage and Slope Stability in Relation to Roots, Association of Dam Safety Officials 2011 Conference, Washington D.C., September.

Shriro, M., 2014, Static and Seismic Performance of California Levees, Doctoral Report, University of California, Berkeley.

Shriro, M., Cobos-Roa, D., Bray, J., Sitar, N., Lichter, J. and Evans, R. (2014a). *Volume 2. – Parallel Trench Wetting Front Test, North Levee of the American River at Cal Expo Sacramento, California*. Influence of Tree Roots and Mammal Burrowing Activity on Levee Performance. Report UCB GT 13-03 vol.2, Geotechnical Engineering, University of California, Berkeley.

Shriro, M., Bray, J., Sitar, N., Cobos-Roa, D (2014b). *Volume 3. – Crown Trench Wetting Front Test, Twitchell Island on the Sevenmile Slough, Rio Vista, California*. Influence of Tree Roots and Mammal Burrowing Activity on Levee Performance. Report UCB GT 13-03 vol.3, Geotechnical Engineering, University of California, Berkeley.

URS (2009). *General Reevaluation Report*. American River Common Features, Sacramento County, California: U.S. Army Corps of Engineers Sacramento District, Contract Number W91238-08-D-0001, Delivery Order CM04.

URS, 2014, Guidance Document for Geotechnical Analyses, Urban Levee Evaluations Project, prepared for Department of Water Resources, Version 14, February.

USACE 1999 – American River Watershed

U. S. Department of the Interior Bureau of Reclamation. (1998). “Engineering Geology Field Manual”. Second Edition.

Van Genuchten, M. Th., 1980, A closed-form equation for predicting the hydraulic conductivity of unsaturated soils. Soil Science Society of America Journal, 44:892-898.

Youd T.L., Idriss I.M., Andrus R.D., Arango I., Castro G., Christian J.T., Dobry R., Finn W.D.L., Harder Jr. L.F., Hynes M.E., Ishihara K., Koester J.P., Liao S.S.C., Marcuson III W.F., Martin G.R., Mitchell J.K., Moriwaki Y., Power M.S., Robertson P.K., Seed R.B., & Stokoe II K.H., 2001. Liquefaction resistance of soils: summary report from the 1996 NCEER and 1998 NCEER/NSF workshops on evaluation of liquefaction resistance of soils. *Journal of Geotechnical and Geoenvironmental Engineering*. Vol. 127(10): 817-903.

APPENDIX A

ROOT REINFORCING – TWITCHELL ISLAND TEST SITE, RIO VISTA, CALIFORNIA

Model	Section	Pore Pressure Condition	Root Number*	Root Embedment (ft)	Diameter (in)	Bond Stress (psf)	Tensile Strength (lbs)
Landside A	A1	Steady State Test	1	4	0.5	101	570
			2	6	0.5	122	570
			3	10	0.5	223	570
	A2	Steady State Test	1	6	0.3	122	205
			2	10	0.5	223	570
	A3	Steady State Test	-	-	-	-	-
	A1 (2D)	Steady State Test No Tree	-	-	-	-	-
	A2	Steady State Test No Tree	-	-	-	-	-
	A3	Steady State Test No Tree	-	-	-	-	-
	A1	Initial Pre-Test with Tree	1	4	0.5	112	570
			2	6	0.5	169	570
			3	10	0.5	282	570
	A2	Initial Pre-Test with Tree	1	6	0.3	169	205
			2	10	0.5	282	570
	A3	Initial Pre-Test with Tree	-	-	-	-	-
	A1	Initial Pre-Test without Tree	-	-	-	-	-
	A2	Initial Pre-Test without Tree	-	-	-	-	-
	A3	Initial Pre-Test without Tree	-	-	-	-	-
	A1	Steady State - Waterside Flood	1	4	0.5	112	570
			2	6	0.5	169	570
			3	10	0.5	282	570
	A2	Steady State - Waterside Flood	1	6	0.3	169	205
			2	10	0.5	282	570
	A3	Steady State - Waterside Flood	-	-	-	-	-
Landside C	C1 (2D)	Steady State Test	-	-	-	-	-
	C3	Steady State Test	-	-	-	-	-

* Roots are numbered beginning with 1 at the shallowest ~~embedment~~ depth and increasing sequentially with increasing depth

Model	Section	Pore Pressure Condition	Root Number*	Root Embedment (ft)	Diameter (in)	Bond Stress (psf)	Tensile Strength (lbs)
Waterside A	A1	Steady State - Test	-	-	-	-	-
	A3	Steady State - Test	-	-	-	-	-
	A1	Steady State - Landside Flood	-	-	-	-	-
	A3	Steady State - Landside Flood	-	-	-	-	-
Waterside B-1	B1	39 Hr Transient - Test	1	6	1	127	2280
			2	8	1.5	155	5130
	B3	39 Hr Transient - Test	1	6	1	127	2280
Waterside B-2	B1	39 Hr Transient - Test	1	6	1	127	2280
			2	8	1.5	155	5130
	B2	39 Hr Transient - Test	1	6	0.75	127	1282
	B3a	39 Hr Transient - Test	1	6	0.75	127	1282
	B3b	39 Hr Transient - Test	1	6	0.75	127	1282
	B1 - No Tree (2D)	39 Hr Transient - Test	-	-	-	-	-
	B2 - No Tree	39 Hr Transient - Test	-	-	-	-	-
	B3a - No Tree	39 Hr Transient - Test	-	-	-	-	-
	B3b - No Tree	39 Hr Transient - Test	-	-	-	-	-
Waterside BC-3	B1	2 Hr Transient - Test	1	6	1	169	2280
			2	8	1.5	226	5130
	B2	2 Hr Transient - Test	1	6	0.8	169	1459
	B3	2 Hr Transient - Test	1	6	0.7	169	1117
	C2	2 Hr Transient - Test	1	8	1	226	2280
	C3	2 Hr Transient - Test	-	-	-	-	-
	B1	39 hrs - Test	1	6	1	127	2280
			2	8	1.5	155	5130
	B2	39 hrs - Test	1	6	0.8	127	1459
	B3	39 hrs - Test	1	6	0.7	127	1117
	C2	39 hrs - Test	1	8	1	179	2280
	C3 (2D)	39 hrs - Test	-	-	-	-	-
	B1 No tree	39 Hr Transient - Test	-	-	-	-	-
	B2 - No Tree	39 Hr Transient - Test	-	-	-	-	-
	B3 - No Tree	39 Hr Transient - Test	-	-	-	-	-
	C2 - No Tree	39 Hr Transient - Test	-	-	-	-	-
	C3 - No Tree	39 Hr Transient - Test	-	-	-	-	-

* Roots are numbered beginning with 1 at the shallowest ~~embedment~~ depth and increasing sequentially with increasing depth

Max Load ~~Esimate~~ Based on Root Size and Embedment

Friction angle 32 degrees
Unit weight 120 pcf
Friction coefficient 0.8 unitless
Max. Tensile Stress: 418000 psf

Root Length 5 ft

Depth (ft)	Effective Overburden Stress (psf)	Bond Stress (psf)	Root Diameter (in) 0.25	0.5	0.75	1	1.25	1.5	1.75	2	2.5	3	3.5	4
1	120	28.2	9	18	28	37	46	55	65	74	92	111	129	148
2	240	56.4	18	37	55	74	92	111	129	148	185	221	258	295
3	360	84.6	28	55	83	111	138	166	194	221	277	332	388	443
4	480	112.8	37	74	111	148	185	221	258	295	369	443	517	591
5	600	141.0	46	92	138	185	231	277	323	369	461	554	646	738
6	720	169.2	55	111	166	221	277	332	388	443	554	664	775	886
7	840	197.4	65	129	194	258	323	388	452	517	646	775	904	1034
8	960	225.6	74	148	221	295	369	443	517	591	738	886	1034	1181
9	1080	253.8	83	166	249	332	415	498	581	664	831	997	1163	1329
10	1200	282.0	92	185	277	369	461	554	646	738	923	1107	1292	1476
11	1320	310.2	102	203	305	406	508	609	711	812	1015	1218	1421	1624
12	1440	338.4	111	221	332	443	554	664	775	886	1107	1329	1550	1772
13	1560	366.6	120	240	360	480	600	720	840	960	1200	1440	1680	1919
14	1680	394.8	129	258	388	517	646	775	904	1034	1292	1550	1809	2067
15	1800	423.0	138	277	415	554	692	831	969	1107	1384	1661	1938	2215

Note: Root capacities reported in red are roots expected to fail in tension.

Max Load Esimate Based on Root Size and Embedment

Friction angle 32 degrees
Unit weight 120 pcf
Friction coefficient 0.8 unitless
Max. Tensile Stress: 418000 psf

Root Length 10 ft

Depth (ft)	Effective Overburden Stress (psf)	Bond Stress (psf)	Root Diameter (in) 0.25	0.5	0.75	1	1.25	1.5	1.75	2	2.5	3	3.5	4
1	120	28.2	18	37	55	74	92	111	129	148	185	221	258	295
2	240	56.4	37	74	111	148	185	221	258	295	369	443	517	591
3	360	84.6	55	111	166	221	277	332	388	443	554	664	775	886
4	480	112.8	74	148	221	295	369	443	517	591	738	886	1034	1181
5	600	141.0	92	185	277	369	461	554	646	738	923	1107	1292	1476
6	720	169.2	111	221	332	443	554	664	775	886	1107	1329	1550	1772
7	840	197.4	129	258	388	517	646	775	904	1034	1292	1550	1809	2067
8	960	225.6	142	295	443	591	738	886	1034	1181	1476	1772	2067	2362
9	1080	253.8	142	332	498	664	831	997	1163	1329	1661	1993	2325	2658
10	1200	282.0	142	369	554	738	923	1107	1292	1476	1846	2215	2584	2953
11	1320	310.2	142	406	609	812	1015	1218	1421	1624	2030	2436	2842	3248
12	1440	338.4	142	443	664	886	1107	1329	1550	1772	2215	2658	3101	3544
13	1560	366.6	142	480	720	960	1200	1440	1680	1919	2399	2879	3359	3839
14	1680	394.8	142	517	775	1034	1292	1550	1809	2067	2584	3101	3617	4134
15	1800	423.0	142	554	831	1107	1384	1661	1938	2215	2768	3322	3876	4429

Note: Root capacities reported in red are roots expected to fail in tension.

Max Load Esimate Based on Root Size and Embedment

Friction angle 32 degrees
Unit weight 120 pcf
Friction coefficient 0.8 unitless
Max. Tensile Stress: 418000 psf

Root Length 15 ft

Depth (ft)	Effective Overburden Stress (psf)	Bond Stress (psf)	Root Diameter (in) 0.25	0.5	0.75	1	1.25	1.5	1.75	2	2.5	3	3.5	4
1	120	28.2	28	55	83	111	138	166	194	221	277	332	388	443
2	240	56.4	55	111	166	221	277	332	388	443	554	664	775	886
3	360	84.6	83	166	249	332	415	498	581	664	831	997	1163	1329
4	480	112.8	111	221	332	443	554	664	775	886	1107	1329	1550	1772
5	600	141.0	138	277	415	554	692	831	969	1107	1384	1661	1938	2215
6	720	169.2	142	332	498	664	831	997	1163	1329	1661	1993	2325	2658
7	840	197.4	142	388	581	775	969	1163	1357	1550	1938	2325	2713	3101
8	960	225.6	142	443	664	886	1107	1329	1550	1772	2215	2658	3101	3544
9	1080	253.8	142	498	747	997	1246	1495	1744	1993	2492	2990	3488	3987
10	1200	282.0	142	554	831	1107	1384	1661	1938	2215	2768	3322	3876	4429
11	1320	310.2	142	570	914	1218	1523	1827	2132	2436	3045	3654	4263	4872
12	1440	338.4	142	570	997	1329	1661	1993	2325	2658	3322	3987	4651	5315
13	1560	366.6	142	570	1080	1440	1799	2159	2519	2879	3599	4319	5039	5758
14	1680	394.8	142	570	1163	1550	1938	2325	2713	3101	3876	4651	5426	6201
15	1800	423.0	142	570	1246	1661	2076	2492	2907	3322	4153	4983	5814	6644

Note: Root capacities reported in red are roots expected to fail in tension.

Max Load Esimate Based on Root Size and Embedment

Friction angle 32 degrees
Unit weight 120 pcf
Friction coefficient 0.8 unitless
Max. Tensile Stress: 418000 psf

Root Length 20 ft

Depth (ft)	Effective Overburden Stress (psf)	Bond Stress (psf)	Root Diameter (in) 0.25	0.5	0.75	1	1.25	1.5	1.75	2	2.5	3	3.5	4
1	120	28.2	37	74	111	148	185	221	258	295	369	443	517	591
2	240	56.4	74	148	221	295	369	443	517	591	738	886	1034	1181
3	360	84.6	111	221	332	443	554	664	775	886	1107	1329	1550	1772
4	480	112.8	142	295	443	591	738	886	1034	1181	1476	1772	2067	2362
5	600	141.0	142	369	554	738	923	1107	1292	1476	1846	2215	2584	2953
6	720	169.2	142	443	664	886	1107	1329	1550	1772	2215	2658	3101	3544
7	840	197.4	142	517	775	1034	1292	1550	1809	2067	2584	3101	3617	4134
8	960	225.6	142	570	886	1181	1476	1772	2067	2362	2953	3544	4134	4725
9	1080	253.8	142	570	997	1329	1661	1993	2325	2658	3322	3987	4651	5315
10	1200	282.0	142	570	1107	1476	1846	2215	2584	2953	3691	4429	5168	5906
11	1320	310.2	142	570	1218	1624	2030	2436	2842	3248	4060	4872	5684	6497
12	1440	338.4	142	570	1282	1772	2215	2658	3101	3544	4429	5315	6201	7087
13	1560	366.6	142	570	1282	1919	2399	2879	3359	3839	4799	5758	6718	7678
14	1680	394.8	142	570	1282	2067	2584	3101	3617	4134	5168	6201	7235	8268
15	1800	423.0	142	570	1282	2215	2768	3322	3876	4429	5537	6644	7752	8859

Note: Root capacities reported in red are roots expected to fail in tension.

Max Load Esimate Based on Root Size and Embedment

Friction angle 32 degrees
Unit weight 120 pcf
Friction coefficient 0.8 unitless
Max. Tensile Stress: 418000 psf

Root Length 25 ft

Depth (ft)	Effective Overburden Stress (psf)	Bond Stress (psf)	Root Diameter (in) 0.25	0.5	0.75	1	1.25	1.5	1.75	2	2.5	3	3.5	4
1	120	28.2	46	92	138	185	231	277	323	369	461	554	646	738
2	240	56.4	92	185	277	369	461	554	646	738	923	1107	1292	1476
3	360	84.6	138	277	415	554	692	831	969	1107	1384	1661	1938	2215
4	480	112.8	142	369	554	738	923	1107	1292	1476	1846	2215	2584	2953
5	600	141.0	142	461	692	923	1154	1384	1615	1846	2307	2768	3230	3691
6	720	169.2	142	554	831	1107	1384	1661	1938	2215	2768	3322	3876	4429
7	840	197.4	142	570	969	1292	1615	1938	2261	2584	3230	3876	4522	5168
8	960	225.6	142	570	1107	1476	1846	2215	2584	2953	3691	4429	5168	5906
9	1080	253.8	142	570	1246	1661	2076	2492	2907	3322	4153	4983	5814	6644
10	1200	282.0	142	570	1282	1846	2307	2768	3230	3691	4614	5537	6460	7382
11	1320	310.2	142	570	1282	2030	2538	3045	3553	4060	5075	6091	7106	8121
12	1440	338.4	142	570	1282	2215	2768	3322	3876	4429	5537	6644	7752	8859
13	1560	366.6	142	570	1282	2280	2999	3599	4199	4799	5998	7198	8398	9597
14	1680	394.8	142	570	1282	2280	3230	3876	4522	5168	6460	7752	9044	10335
15	1800	423.0	142	570	1282	2280	3461	4153	4845	5537	6921	8305	9689	11074

Note: Root capacities reported in red are roots expected to fail in tension.

Max Load Esimate Based on Root Size and Embedment

Friction angle 32 degrees
Unit weight 120 pcf
Friction coefficient 0.8 unitless
Max. Tensile Stress: 418000 psf

Root Length 35 ft

Depth (ft)	Effective Overburden Stress (psf)	Bond Stress (psf)	Root Diameter (in) 0.25	0.5	0.75	1	1.25	1.5	1.75	2	2.5	3	3.5	4
1	120	28.2	65	129	194	258	323	388	452	517	646	775	904	1034
2	240	56.4	129	258	388	517	646	775	904	1034	1292	1550	1809	2067
3	360	84.6	142	388	581	775	969	1163	1357	1550	1938	2325	2713	3101
4	480	112.8	142	517	775	1034	1292	1550	1809	2067	2584	3101	3617	4134
5	600	141.0	142	570	969	1292	1615	1938	2261	2584	3230	3876	4522	5168
6	720	169.2	142	570	1163	1550	1938	2325	2713	3101	3876	4651	5426	6201
7	840	197.4	142	570	1282	1809	2261	2713	3165	3617	4522	5426	6330	7235
8	960	225.6	142	570	1282	2067	2584	3101	3617	4134	5168	6201	7235	8268
9	1080	253.8	142	570	1282	2280	2907	3488	4070	4651	5814	6976	8139	9302
10	1200	282.0	142	570	1282	2280	3230	3876	4522	5168	6460	7752	9044	10335
11	1320	310.2	142	570	1282	2280	3553	4263	4974	5684	7106	8527	9948	11369
12	1440	338.4	142	570	1282	2280	3562	4651	5426	6201	7752	9302	10852	12403
13	1560	366.6	142	570	1282	2280	3562	5039	5878	6718	8398	10077	11757	13436
14	1680	394.8	142	570	1282	2280	3562	5130	6330	7235	9044	10852	12661	14470
15	1800	423.0	142	570	1282	2280	3562	5130	6783	7752	9689	11627	13565	15503

Note: Root capacities reported in red are roots expected to fail in tension.

APPENDIX B

SLOPE STABILITY MODELING RESULTS – TWITCHELL ISLAND TEST SITE, RIO VISTA, CALIFORNIA

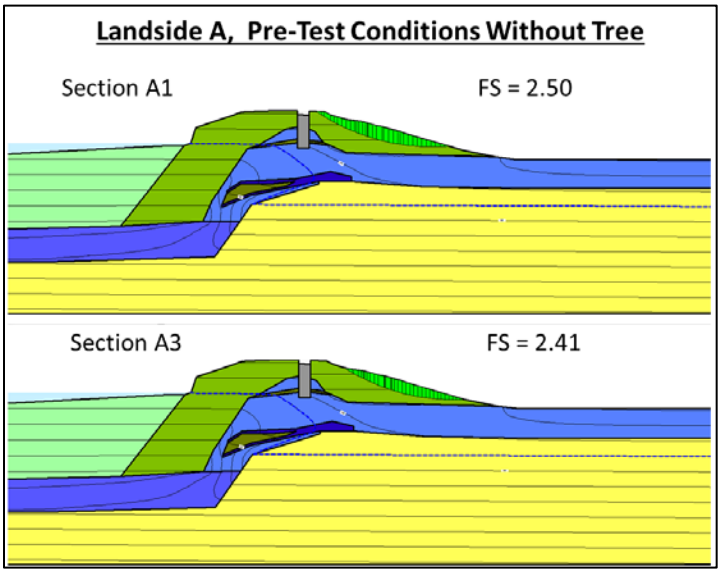

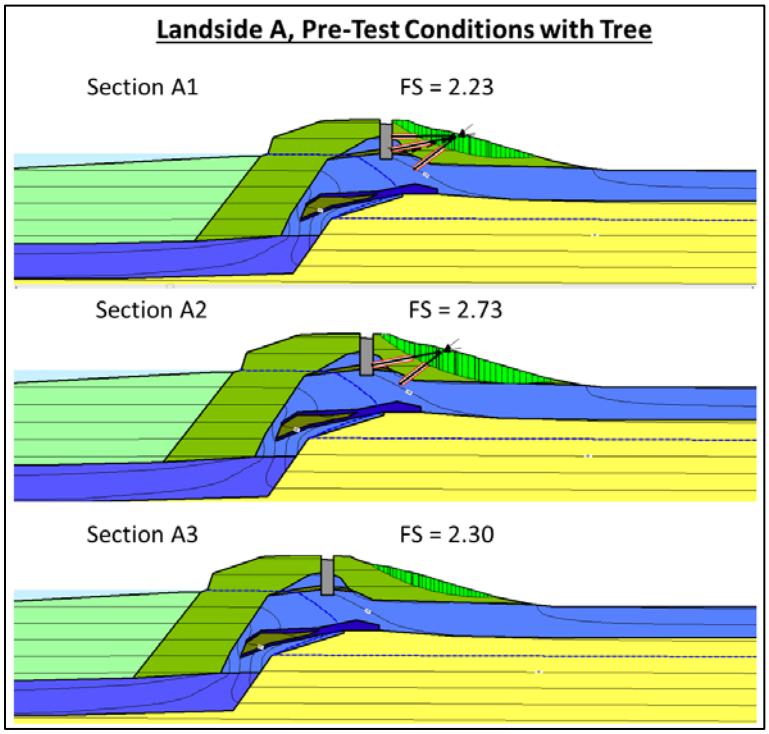

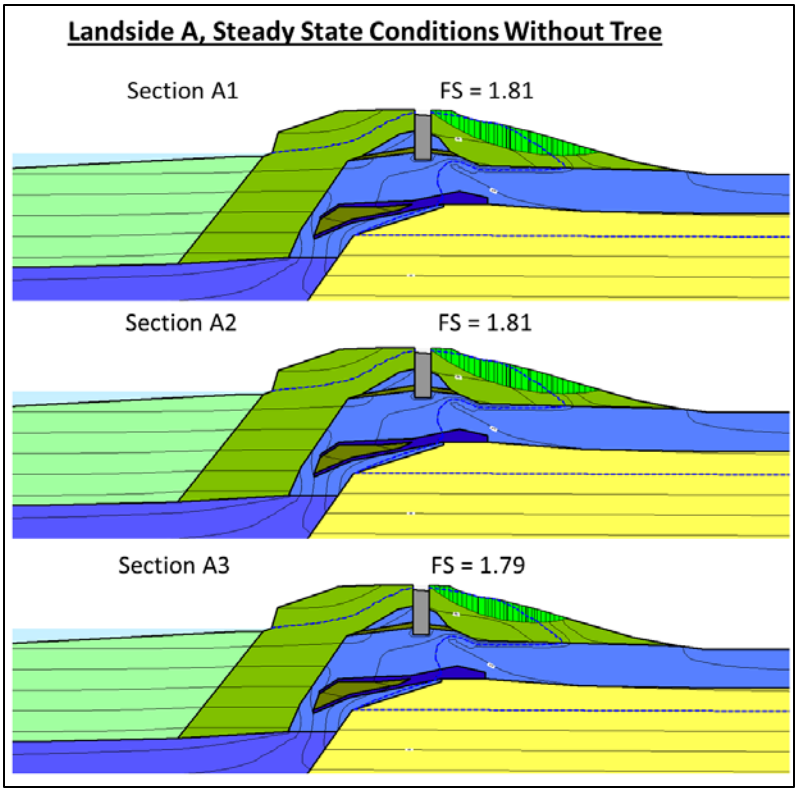
Landside A, Steady State Conditions Without Tree
Section A1
FS = 1.81
Section A2
FS = 1.81
Section A3
FS = 1.79

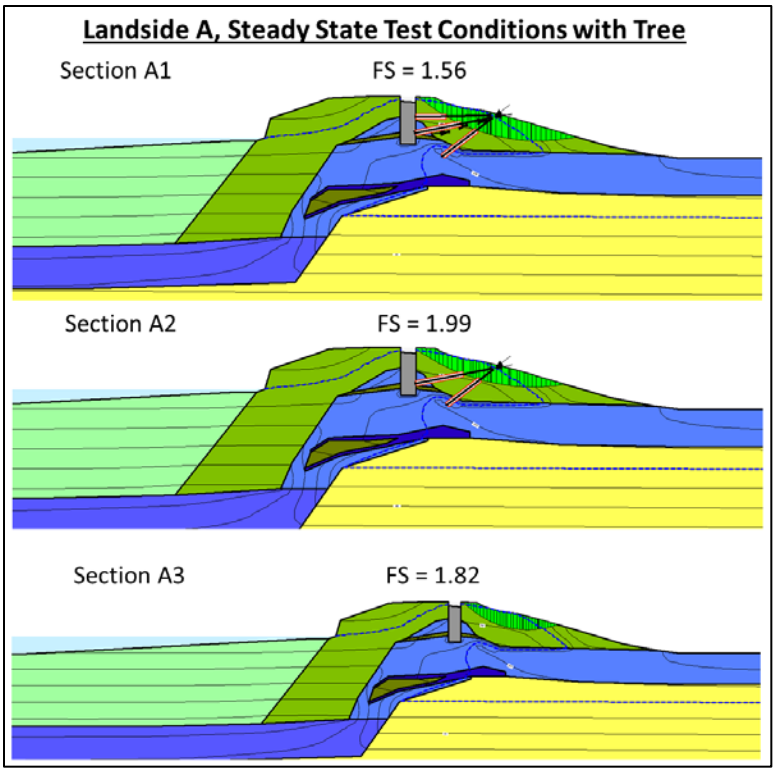
Landside A, Steady State Test Conditions with Tree
Section A1
FS = 1.56
Section A2
FS = 1.99
Section A3
FS = 1.82

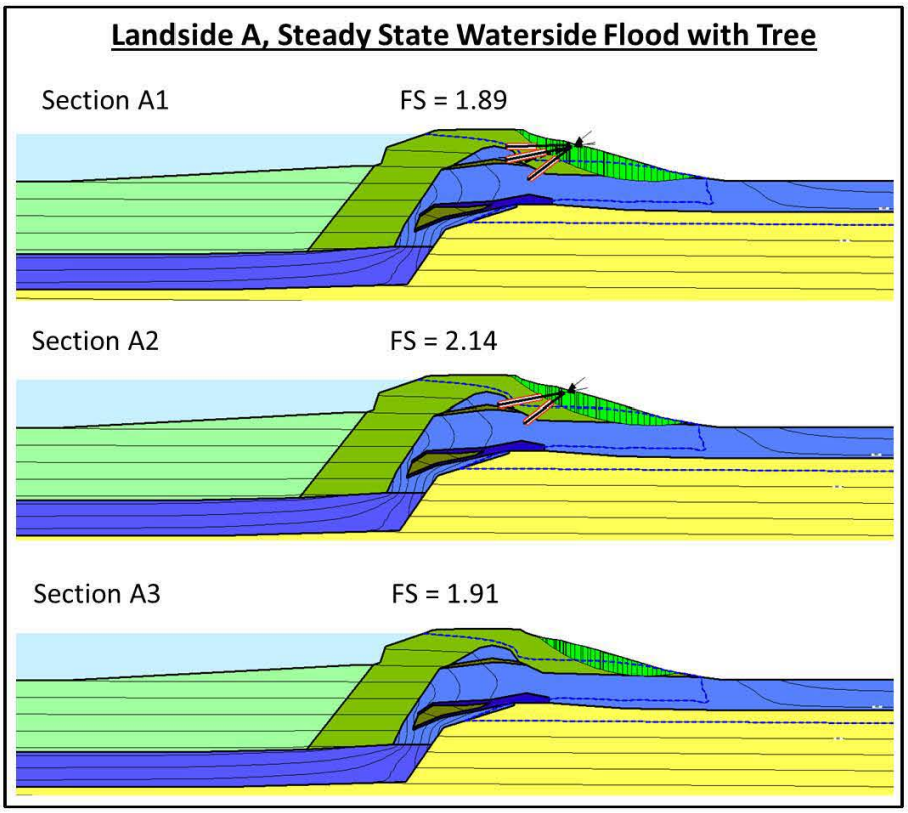
Landside A, Steady State Waterside Flood with Tree
Section A1
FS = 1.89
Section A2
FS = 2.14
Section A3
FS = 1.91

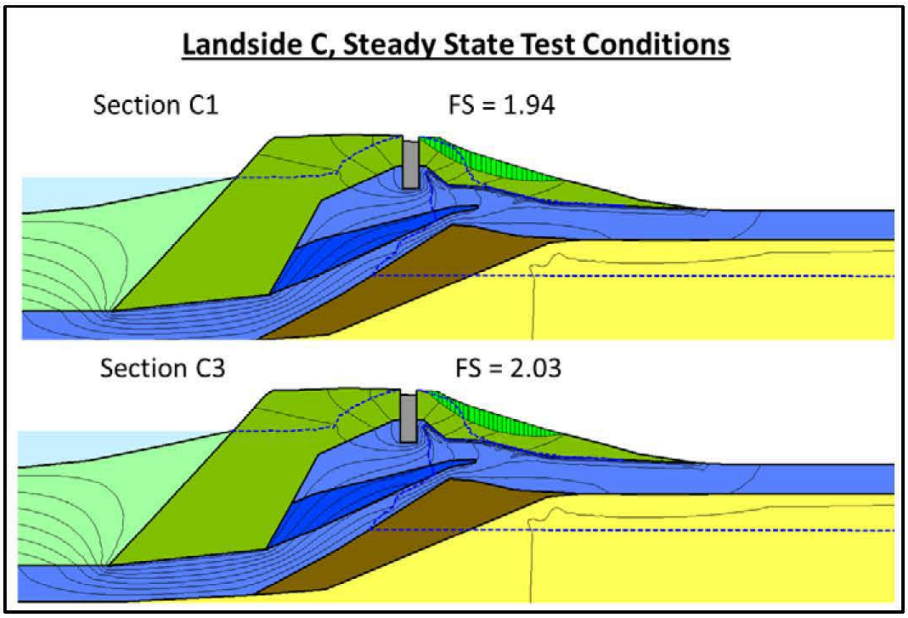
Landside C, Steady State Test Conditions
Section C1
FS = 1.94
Section C3
FS = 2.03

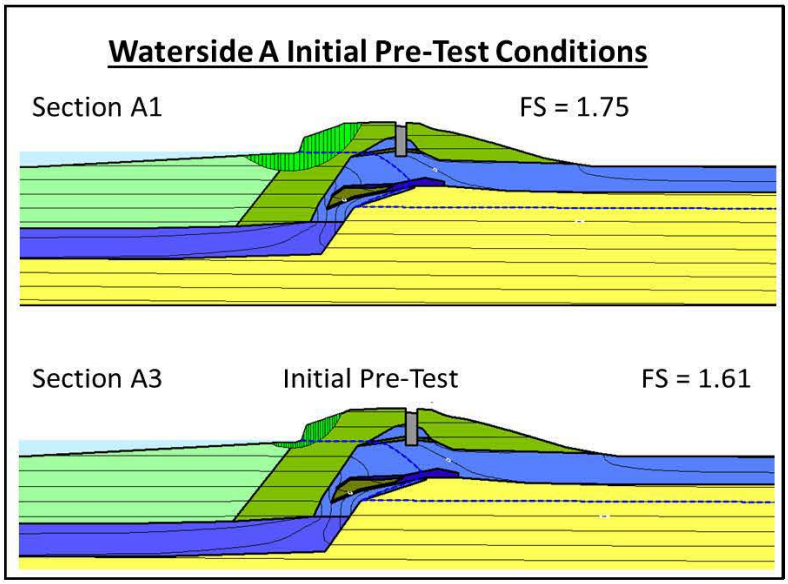
Waterside A Initial Pre-Test Conditions
Section A1
FS = 1.75
Section A3
Initial Pre-Test
FS = 1.61

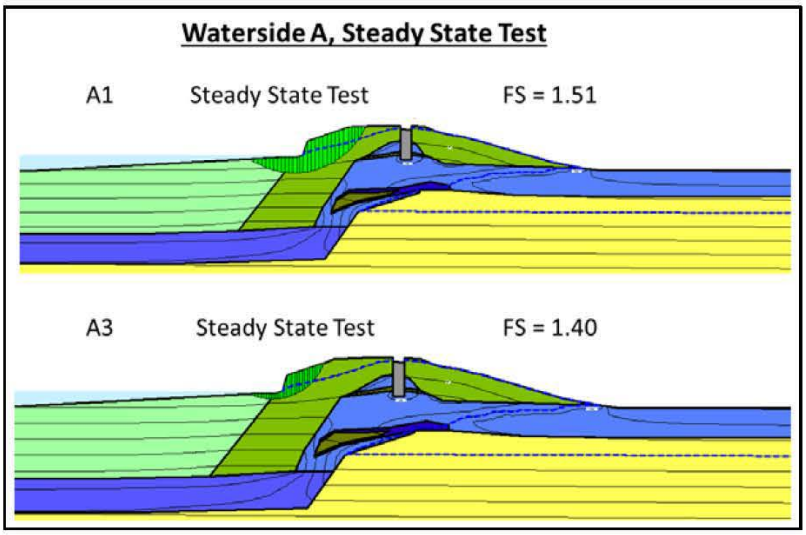
Waterside A, Steady State Test
A1
Steady State Test
FS = 1.51
A3
Steady State Test
FS = 1.40

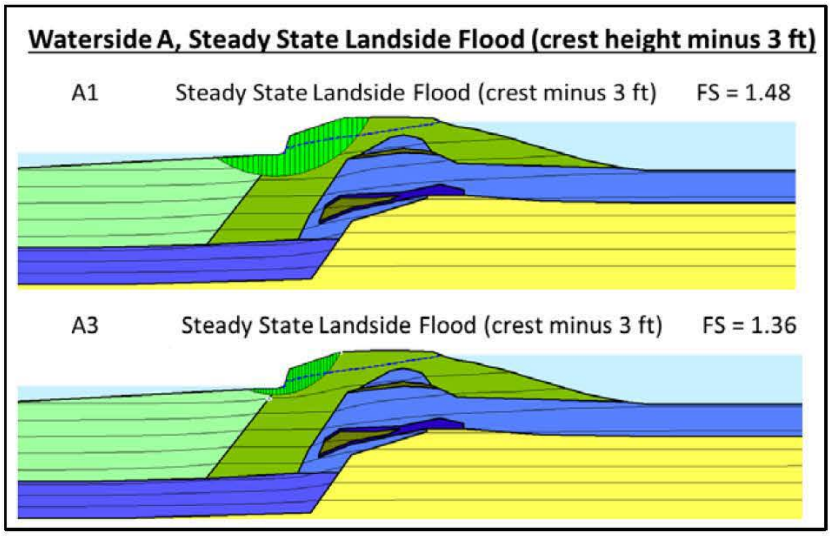
Waterside A, Steady State Landside Flood (crest height minus 3 ft)
A1
Steady State Landside Flood (crest minus 3 ft)
FS = 1.48
A3
Steady State Landside Flood (crest minus 3 ft)
FS = 1.36

Waterside B1 - – 39 hr Transient Test Conditions, with Tree

Section B1 FS = 0.96

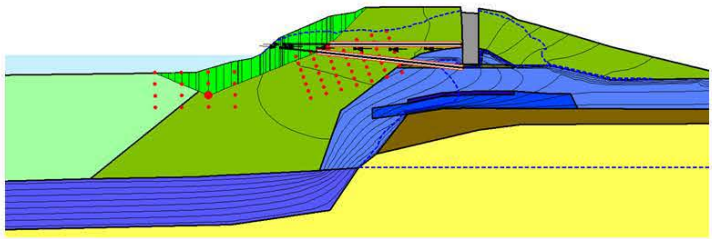

Section B3 FS = 1.50

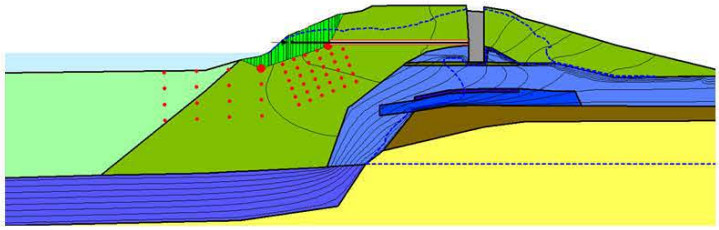

Waterside B2 – 39 hr Transient Test Conditions, with Tree

Section B1 FS = 1.05

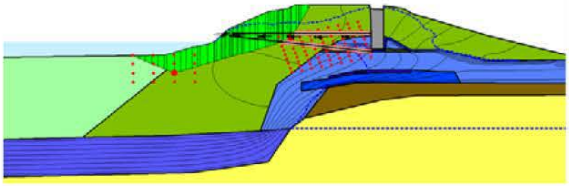

Section B2 FS = 1.28

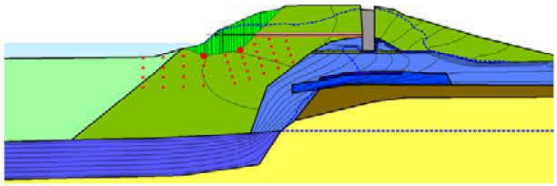

Section B3a FS = 1.35

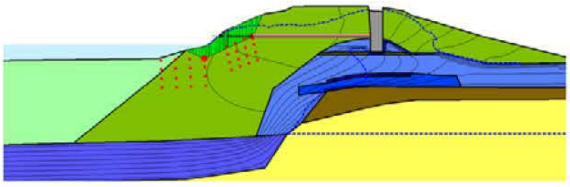

Section B3b FS = 1.44

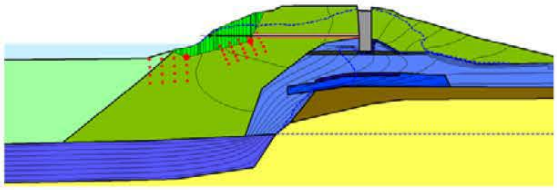

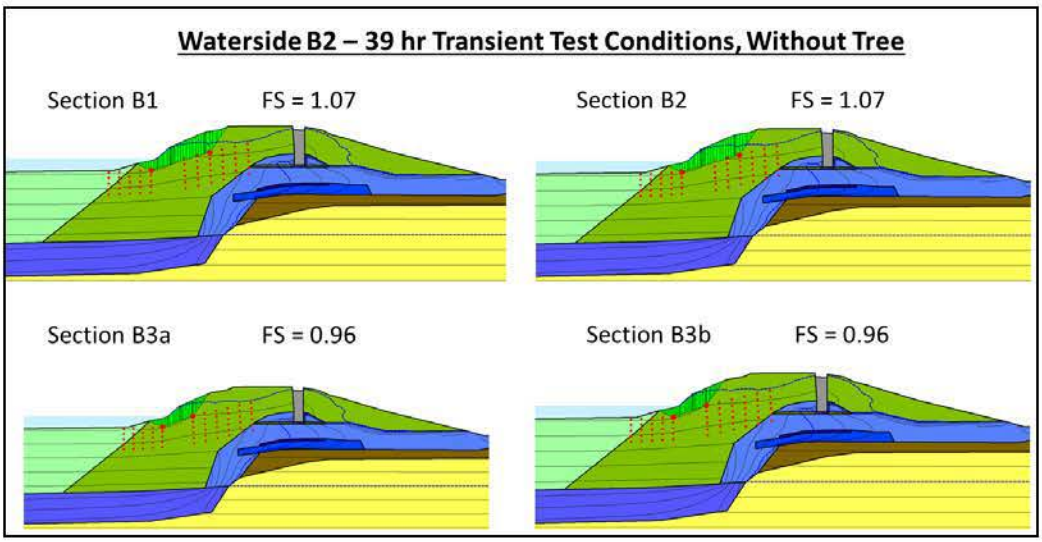
Waterside B2 – 39 hr Transient Test Conditions, Without Tree
Section B1
FS = 1.07
Section B2
FS = 1.07
Section B3a
FS = 0.96
Section B3b
FS = 0.96

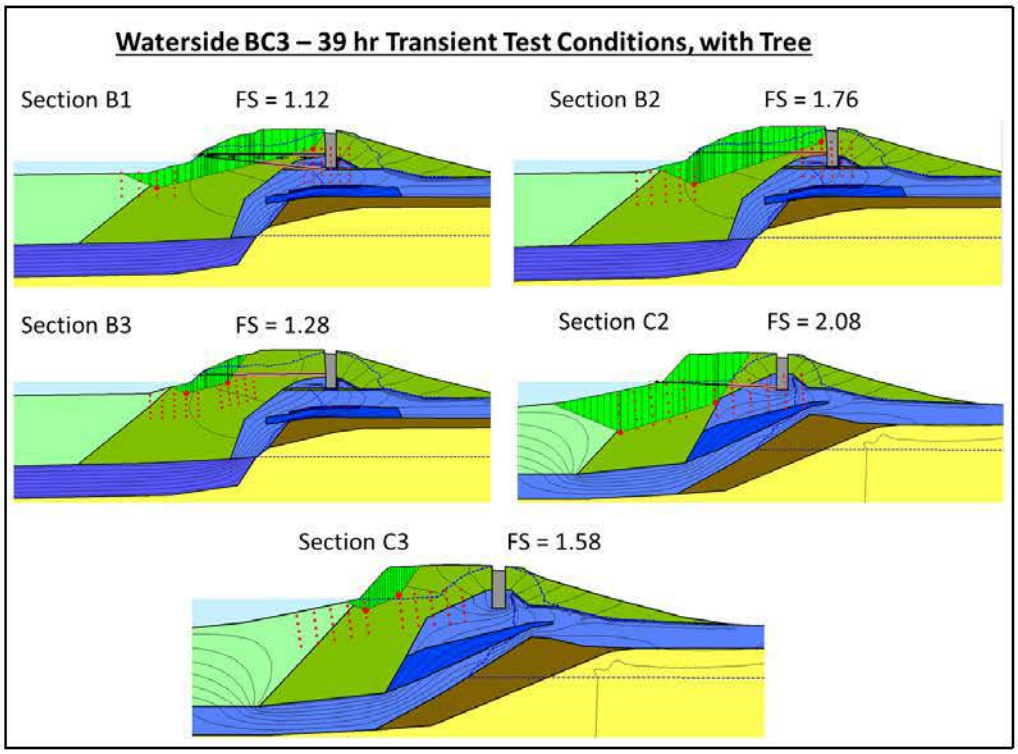
Waterside BC3 – 39 hr Transient Test Conditions, with Tree
Section B1
FS = 1.12
Section B2
FS = 1.76
Section B3
FS = 1.28
Section C2
FS = 2.08
Section C3
FS = 1.58

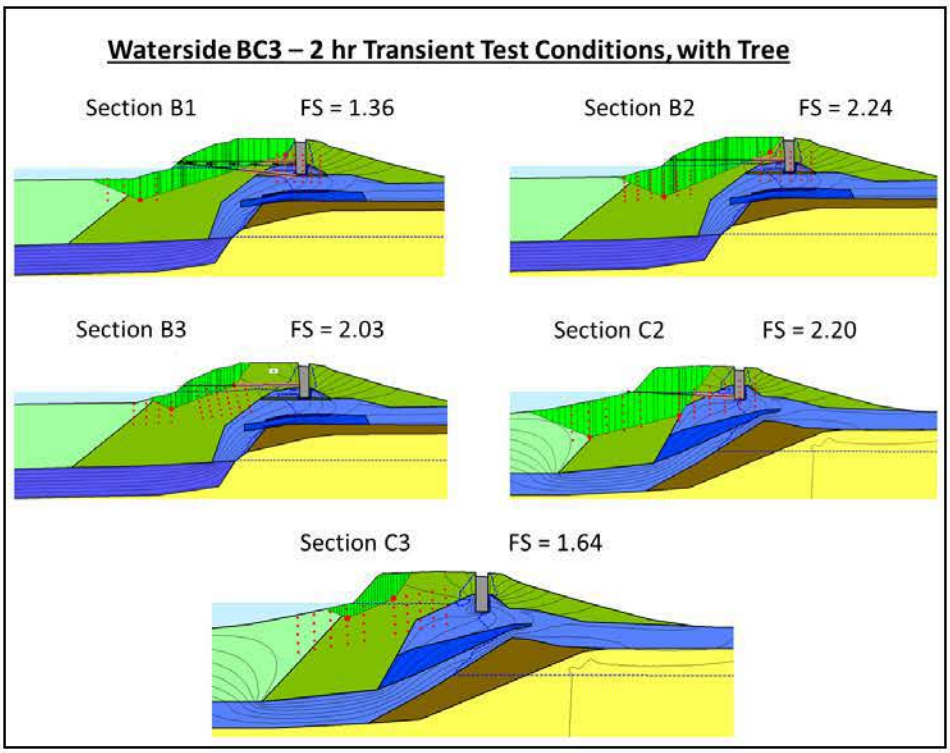
Waterside BC3 – 2 hr Transient Test Conditions, with Tree
Section B1
FS = 1.36
Section B2
FS = 2.24
Section B3
FS = 2.03
Section C2
FS = 2.20
Section C3
FS = 1.64

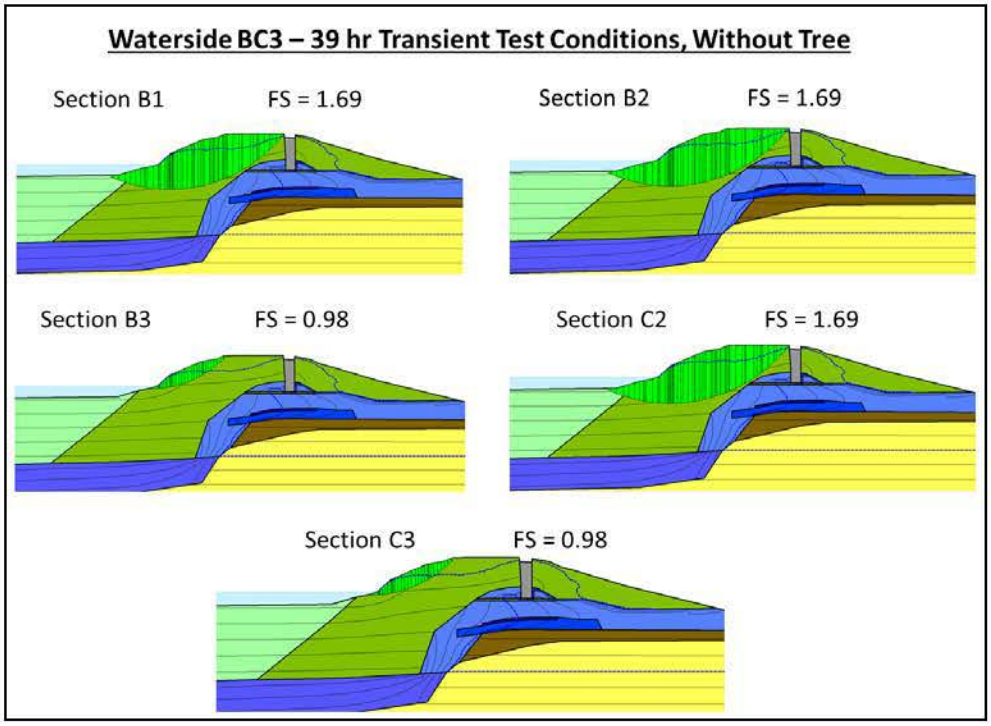
Waterside BC3 – 39 hr Transient Test Conditions, Without Tree
Section B1
FS = 1.69
Section B2
FS = 1.69
Section B3
FS = 0.98
Section C2
FS = 1.69
Section C3
FS = 0.98